PROCEEDINGS OF THE 1985 ANTENNA APPLICATIONS SYMPOSIUM VOLUME 1(U) ROME AIR DEVELOPMENT CENTER GRIFFISS AFB NY DEC 85 RADC-TR-85-242-VOL-1 NO-8166 754 174 F/G 9/5 NL UNCLASSIFIED Ų.



MICROCOPY RESCLUTION TEST CHART NATIONAL BUREAU OF STANDARDS - 1963 - A

RADC-TR-85-242, Vol I (of two) In-House Report December 1985



# PROCEEDINGS OF THE 1985 ANTENNA APPLICATIONS SYMPOSIUM

Sponsored by
ELECTROMAGNETIC SCIENCES DIVISION
ROME AIR DEVELOPMENT CENTER
HANSCOM AFB, BEDFORD MASS. 01731
AIR FORCE SYSTEMS COMMAND



APPROVED FOR PUBLIC RELEASE: DISTRIBUTION UNLIMITED

DITIC FILE COPY

754

AD-A166

ROME AIR DEVELOPMENT CENTER
Air Force Systems Command
Griffiss Air Force Base, NY 13441-5700

120

This report has been reviewed by the RADC Public Affairs Office (PA) and is releasable to the National Technical Information Service (NTIS). At NTIS it will be releasable to the general public, including foreign nations.

RADC-TR-85-242, Vol I (of two) has been reviewed and is approved for publication.

APPROVED:

PAUL H. CARR, Acting Chief Antennas & RF Components Branch Electromagnetic Sciences Division

1 ) W. Cam

APPROVED:

ALLAN C. SCHELL

sklan Thiel

Chief, Electromagnetic Sciences Division

FOR THE COMMANDER:

JOHN A. RITZ Plans Office

rlm a. 15

DESTRUCTION NOTICE - For classified documents, follow the procedures in DOD 5200.22-M, Industrial Security Manual, Section II-19 or DOD 5200.1-R, Information Security Program Regulation, Chapter IX. For unclassified, limited documents, destroy by any method that will prevent disclosure of contents or reconstruction of the document.

If your address has changed or if you wish to be removed from the RADC mailing list, or if the addressee is no longer employed by your organization, please notify RADC (EEAA) Griffiss AFB NY 13441-5700. This will assist us in maintaining a current mailing list.

Do not return copies of this report unless contractual obligations or notices on a specific document requires that it be returned.

 CLASSIEICATION OF THIS	PAGE

Unclassified ECURITY CLASSIFICATION OF THIS PAGE		AD-A	11667	54			
REPORT DOCUMEN							
	Uncla	LASSIFICATION SSIFIED		16. RESTRICTIVE N	ARKINGS		
2. SECURI	TY CLASSIFIC	ATION AUTHORITY		3 DISTRIBUTION/A			
26. DECLAS	SIFICATION/	DOWNGRADING SCH	HEDULE		for public ion unlimit	•	:
4. PERFOR	MING ORGAN	IZATION REPORT N	UMBER(S)	S. MONITORING OF	GANIZATION RE	PORT NUMBER	S)
RADC-	rr-85-242	(Volume I)					
6a NAME C		NG ORGANIZATION  opment Center	(If applicable)	7a. NAME OF MONI	TORING ORGANI	ZATION	
Sc. ADDRES	SS (City, State	and ZIP Code)	<del></del>	7b. ADDRESS (City,	State and ZIP Cod	le)	
<sup>o</sup> Hansco Massao	om AFB chusetts	01731					
ORGAN	IZATION	sponsoming opment Center	8b. OFFICE SYMBOL (If applicable) EEAA	9. PROCUREMENT	INSTRUMENT ID	ENTIFICATION N	UMBER
Bc. ADDRES	SS (City, State	and ZIP Code)	<del></del>	10. SOURCE OF FU	NDING NOS.	<del></del>	
Hansco	om AFB			PROGRAM ELEMENT NO.	PROJECT NO.	TASK NO.	WORK UNIT
	chusetts			62702F	4600	14	01
11. TITLE (	Include Securit	y Classification) Pr	oceedings of the	1			[
	Antenna A NALAUTHOR	pplications S (\$)	vmDosium	<u> </u>	<u> </u>	<u>l</u>	J
		1.5. 5	E COVERED	14. DATE OF REPO		1.5 0.05	
In-hou	OF REPORT	FROM_	то	1985 Decemb	oer	338	8
331 th	irough 69	4	I consists of page Monitor (RADC/EE		330; Volume	e II consis	ts of pages
17.	COSATI		18. SUBJECT TERMS (C	ontinue on reverse if n		fy by block numbe	r)
FIELD	GROUP 03	SUB. GR.	Antennas Satellite Ante	Microst ennas Reflect		Multibeam	
<u> </u>	- 03		Broadband Ante			Array Anto	ennas
The Proceedings of the 1985 Antenna Applications Symposium is a collection of state-of-the-art papers relating to phased array antennas, multibeam antennas, satellite antennas, microstrip antennas, reflector antennas, HF, VHF, UHF and various other antennas.							
O. DISTRIE	BUTION/AVAI	LABILITY OF ABSTE	ACT	21. ABSTRACT SEC	URITY CLASSIFIC	CATION	

20. DISTRIBUTION/AVAILABILITY OF ABSTRACT	21. ABSTRACT SECURITY CLASSIFI	CATION
UNCLASSIFIED/UNLIMITED - SAME AS APT. W DTIC USERS -	Unclassified	
22. NAME OF RESPONSIBLE INDIVIDUAL	22b. TELEPHONE NUMBER (Include Area Code)	22c. OFFICE SYMBOL
Daniel T. McGrath, Capt, USAF	(617) 861-4036	RADC/EEAA

DD FORM 1473, 83 APR

THE RESERVED FOR STATEMENT SANSTAGE SECTIONS FROM REPRESENT SANSTAGE SANSTAGE.

EDITION OF 1 JAN 73 IS OBSOLETE.

Unclassified

#### **PREFACE**

The Antenna Applications Symposium, held at the University of Illinois' Robert Allerton Park, was cosponsored by Rome Air Development Center's Electromagnetic Sciences Division (RADC/EEAA), Hanscom AFB, MA and the University of Illinois' Electromagnetic Laboratory under Contract F19628-85-M-0008. Professor Paul Mayes of UI was the symposium chairman. Capt. Daniel McGrath of RADC/EEA was the symposium manager for the Air Force.

Accession For				
NTIS	GRA&I			
DTIC	TAB			
Unann	ounced			
Justi	fication_			
By	D.			
,	Distribution/			
Avai	Availability Codos			
	Avail and/or			
Dist	Dist Special			
A·1				



# **Contents**

#### Votume 1

Keynote: "Antenna Technology," R. C. Johnson

and become statement because a session assessed to the session assessed to the session assessed to the session of the session and the session assessed to the session as th

Wednesday, September 18, 1985

#### Session 1

#### Arrays

Chairman: P. R. Franchi, Rome Air Development Center

1.	"Antenna Elements for Integrated Phased Arrays," D. H. Schaubert, R. W. Jackson and D. M. Pozar	1
2.	"Cross Polarization Considerations for Microstrip Antenna Array Modules," M. L. Oberhart and Y. T. Lo	27
3.	"Ku-Band High-Gain Microstrip Planar Array for TDRSS," F. Lalezari and C. Gilbert	45
4.	"Diode Grids for Electronic Beam Steering and Frequency Multiplication," W. W. Lam, C. F. Jou, N. C. Luhmann, Jr., and D. B. Rutledge	67
5.	"Design of a Tilted Beam Waveguide Planar Array," J. M. Wachsman	73
6.	"Resonant Microstrip Dipole Arrays," J. Lane, N. Sa, and	91

#### Session II

#### Broadband and Multiband Antennas

Chairman: P. E. Mayes, University of Illinois

7.	"Some Broadband, Low-Profile Antennas," P. Mayes, D. Tanner, R. Waller, J. Drewniak, T. Szmurlo, A. Boris and D. Kunkee	105
8.	"A Dual Feed Dual Polarized Log-Periodic HF Antenna System," D. V. Campbell, P. Dubowicz, B. Feigenbaum and K. Loffer	141
* 9.	"Coaxial Antennas for Duplex Operation," J. N. Hines and R. E. Myer	
10.	"A Dual Frequency Microstrip Antenna for Ka Band," R. Q. Lee and M. F. Baddour	165
11.	"Traveling Wave Dipole Array for HF-VHF-UHF Tactical DF Systems," S. C. Kuo, H. Cook, and H. Hochman	189
*12.	"Broadband Size-Reduced Antennas for Spacecraft Applications," J. L. Wong and H.E. King	
13.	"Reduction of Coupling Between Cosited Antennas by Separation of Near Fields," D. V. Campbell, P. Dubowicz and R. Hoverter	205
	Thursday, September 19, 1985	
	Session III	
	Reflectors, Lenses and Feeds	
	Chairman: Y. Rahmat-Samii, Jet Propulsion Laboratory, California Institute of Technology	
*14.	"Overview of Reflector Antenna Technology," Y. Rahmat-Samii	
15.	"K & S Band Feed System for an 18-Meter High-Efficiency Cassegrain Antenna," B. X. Nguyen, R. Rudolph, G. H. Schennum and C. H. Tsao	n <sup>221</sup>
16.	"Low-Loss Symmetric Off-Axis Feeds for Symmetric Dual Reflector Antennas," T. Veruttipong, V. Galindo-Israel and W. Imbriale	255
17.	"Improving the Performance of a Small Reflector Antenna," M. Lewis, J. Toth, R. Kliger and W. Miccioli	, 313
		Volume II

18. "Reflector Pattern Control Using Variable Phase Plates," D. Jacavanco, Sr.

331

scal lectored ministral terrespon societies existed existing contract terrespon terrespon terrespond

### Contents

19.	"A Numerical Method for Approximating Antenna Surfaces Defined by Discrete Surface Points," R. Q. Lee and R. J. Acosta	351
20.	"Experimental Transform Feed Antenna," D. T. McGrath	359
21.	"High Efficiency Multibeam Antenna Design," P. G. Ingerson and C. A. Chen	377
	Session IV	
	Analysis and Measurement I	
	Chairman: R. Mittra, University of Illinois	
22.	"On the Use of the Numerical Electromagnetics Code (NEC) to Solve for the Input Impedance and Radiative Efficiency of Loaded, Thin-Wire Antennas," B. M. Halpern and R. Mittra	405
23.	"Electromagnetic Analysis of Dielectric Honeycomb Supports for Frequency Selective Surfaces," R. E. Jorgenson, R. Mittra, H. Ohta, K. C. Lang and T. K. Wu	435
24.	"Application of Planar Near Field Measurement Techniques for Space Antennas," R. D. Ward and M. A. Shulz	459
25.	"Evaluation of a VHF Satellite Antenna System," C. W. Thousand	475
26.	"Automated Three-Antenna Polarization Measurements Using Digital Signal Processing," J. R. Jones and D. W. Hess	497
27.	"Preliminary Evaluation of MMIC Array Antenna Performance," J. Smetana and R. J. Acosta	
28.	"Simple Expressions for the Phase Centers of Small Horn Antennas," P. R. Franchi	513
29.	"Shaped Beam Earth Coverage Horn Antennas," J. C. Lee and W. Rotman	529
	Friday, September 20, 1985	
	Session V	
	Analysis and Measurement II	
	Chairman: R. Lampe, RCA Missile & Surface Radar Division	
30.	"Circular Array of Coaxially-Fed Monopole Elements in a Parallel Plate Waveguide," B. Tomasic	543

# Contents

31.	"VHF Satellite Antenna System," M. R. Matthew	581
32.	"A Simple Technique to Correct for Curvature Effects on Conformal Phased Arrays," J. Antonucci and P. Franchi	607
33.	"Optimization for Antenna Arrays in an Arbitrary Interference Environment," A. Y. Piatnicia and Y. T. Lo	631
34.	"Wideband Monopulse Antenna Design," D. L. Thomas	661

#### ANTENNA ELEMENTS FOR INTEGRATED PHASED ARRAYS

Daniel H. Schaubert, R.W. Jackson, and D.M. Pozar Department of Electrical and Computer Engineering University of Massachusetts Amherst, MA 01003

#### **ABSTRACT**

Monolithic integrated antennas on GaAs have been studied for use in millimeter wave phased arrays. A number of potential problems, including surface wave effects and available area for circuit and antenna layout, have led to the consideration of antenna and circuit structures that utilize different surfaces and substrates for these two functions. There is no need for via connections between the feed circuit and the radiating elements because effective means of electromagnetic coupling are utilized. Two particular antennas will be described: 1) aperture-coupled patch and 2) slot-fed dipoles. Both of these antenna/circuit structures can use a GaAs substrate for active devices and circuits while using a lower permittivity substrate for the radiating elements. The aperture-coupled patch utilizes microstripline for the feed network, and a ground plane isolates the feed network from the radiating aperture. The slot-fed dipoles can utilize coplanar waveguide for the feed network. The paper will include experimental results and some calculated results, with emphasis on how the antennas perform.

#### 1.0 INTRODUCTION

Integrated phased array systems consisting of a large number of elements and operating at millimeter wavelengths have motivated many antenna developments in recent years. Reduced cost, increased reliability, and performance are some of the reasons for investigating monolithic and integrated structures, and the high level of integration of active and passive components in these structures makes them different from most systems that have been developed to date. The coexistance of these components requires the use of substrates, transmission lines, and circuit designs that have not been necessary at lower frequencies in modular units. Another feature of these integrated structures is the large number of control and power supply circuits that must be included. All of these features contribute to a very dense packing of components that is difficult to achieve at best and is usually detrimental to system performance.

In this paper, two types of antenna elements are described. These elements are integrable with monolithic circuits, but do not reside on the same substrate surface as the circuits, which reduces component crowding. Coupling to the radiating element is via the electromagnetic fields so that no via connections (plated through holes) are needed. An added advantage of these antennas is that different substrates can be used for the active circuits and the radiators. This can help to alleviate surface wave and scan blindness effects that have been predicted for printed antenna arrays on GaAs<sup>1-4</sup>.

The antenna elements that are described below are a microstrip patch radiator coupled to a microstripline via an aperture in their common ground plane<sup>5,6</sup> and a printed dipole coupled to a slotline in its ground plane. Another version of the latter antenna is a dipole pair coupled to a coplanar waveguide. Measured impedance and radiation properties of these antennas are presented and, for the aperture coupled patch, computed parameter studies provide useful design data.

#### 2.0 APERTURE-COUPLED PATCH

No. Constitution of the Co

The structure of the aperture coupled patch antenna is shown in Figure 1. The patch is resonant and radiates effectively into the upper half space, whereas the aperture is smaller than resonant dimensions and does not radiate much power into the lower half space. The operating frequency of the antenna is determined by the patch dimensions and the input impedance can be controlled by the aperture size and stub length.

An analysis of the structure in Figure 1 has been performed by solving the coupled integral equations for the fields in the upper and lower regions. The method of moments is used along with Green's functions for the grounded dielectric slab [7]. The computations are quite time consuming, requiring 30 minutes per data point on a VAX 11/750, but many useful design studies have been completed.

Typical impedance data are shown in Figure 2 for 3 different stub lengths. The reference plane is located at the center of the aperture. For all impedance plots, measured results are plotted as solid lines and calculated results are plotted as dashed lines.

Increasing the stub length further causes the locus to rotate into the inductive part of the chart and become smaller in size, similar to the loci for shorter stub lengths. If the impedance at a single frequency is tracked for various stub lengths, it is found to follow approximately a constant resistance circle, implying that the slot and antenna appear to the feedline as an impedance in series with an open circuited stub.

The effects of aperture length are shown in Figure 3 and 4. Increasing the aperture length increases the diameter of the impedance locus and lowers the resonant frequency slightly. The combination of stub length and aperture length provide extensive control of the input impedance and allow tuning for perfect match at a single frequency or maximum bandwidth for a given VSWR. (In general, the bandwidth of aperture coupled patches is similar to that of ordinary probe fed or microstripline fed patches of similar size on the same substrate, but some results have been obtained that indicate an increased bandwidth due perhaps to double tuning.)

Increasing the relative permittivity of the feedline substrate has the effects illustrated in Figure 5. For these calculations, the impedance of the microstripline feed was maintained at 50 ohms and the stub length was maintained at 0.22 wavelengths of the microstripline. The specific values of the antenna parameters are listed in the figure.

Measured radiation patterns of aperture coupled patches are shown in Figures 6-8. All of these patterns were taken with a small ground plane and the coaxial transmission line that attaches to the

microstripline has some effect on the E-plane patterns. The level of radiation into the back (feed) region of Figure 6 is not particularly high and does not resemble slot radiation. Therefore, it appears that the resonant patch is providing the primary means of radiation and the feed region would be relatively free of radiated power if the ground plane was large enough. The antennas that were used to obtain the patterns in Figures 7 and 8 were both fabricated by using 0.025-inch Duroid 6010.2 ( $\varepsilon_r$ =10.2) for the feedline and 0.020-inch Duroid 5880 ( $\varepsilon_{r}$ =2.22) for the antenna. The other antenna parameters are given in the figures. The feed substrate in Figure 8 is twice as thick electrically as that in Figure 7, and this may contribute to the increased radiation in the backward region. Nonetheless, relatively little power is radiated to the feed side of the ground plane and absorber in this region should help to control stray coupling effects without significant loss of gain or adverse effects on the upper half space radiation pattern.

#### 3.0 COPLANAR WAVEGUIDE FEEDLINES FOR PRINTED DIPOLES

Manage State of the State of th

Three configurations have been studeed which involve slots feeding printed dipoles; (a) a single slot feeding a single dipole (Figure 9), (b) coplanar waveguide feeding two dipoles (Figure 10(a)) and (c) coplanar waveguide feeding crossed dipoles for circular polarization (Figure 10(b)). All three structures are based upon the slot fed dipole shown in Figure 9. As in the aperture coupled patch two substrates are used, one substrate with a low dielectric constant to enhance antenna operation and one with dielectric that simulates the semiconducting material used for

active devices. Interest in coplanar waveguide feeds is due to the superior R.F. grounding it offers to active devices at millimeter wave frequencies. This grounding advantage can be critical for the design of high gain millimeter wave amplifiers. A possible disadvantage in comparison with the aperture coupled patch is the disruption of the antenna's ground plane caused by the presence of the slots or coplanar waveguide. This effect can be minimized by making the feed cross-section as small as possible.

The slot fed dipole structure is motivated by the well known slotline-to-microstripline transition<sup>8</sup>. In that application, the slot and microstrip lines cross and then extend beyond each other by about one quarter wavelength. For the slot fed dipole case, it was found that placing the slot end almost directly under the dipole gave the best results. Coupling is tightest when the slot is located at nearly the center of the dipole's long dimension, lessening as it is moved closer to an end. The interaction can be considered as inductive coupling between the current flowing around the slot end and the current on the dipole.

The structure shown in Figure 9 was constructed with the antenna supported on a substrate ( $\varepsilon_r$ =2.5) with a thickness of .060" and the slot supported on a substrate ( $\varepsilon_r$ =10.0) with a thickness of .050". A slot of width .010" was excited by a semirigid coaxial line and then tapered to a width of .030" under a dipole which is .820" long and .100" wide. (The dimensions of the dipole, the substrate and the slot under the dipole are the same for the configurations shown in Figure 10(a) and 10(b).) The measured

antenna patterns are shown in Figure 11. Impedance plots show a well behaved resonance with roughly a 1% bandwidth (VSWR < 2) and greater than 20 dB return loss at 4.72 GHz. The patterns show some significant back radiation which is attributed to radiation from the slot feed and from the coax-to-slot transition.

Figure 10(a) illustrates the second configuration, a coplanar waveguide feeding two dipoles. At the board edge, the coplanar waveguide dimensions are chosen for a 50  $\Omega$  impedance. The coupled slots are then gradually thinned to a width of .030", separated by several slot widths (to decouple one from the other) and then routed to each dipole. By adjusting the placement of the dipoles relative to the slots, a return loss greater than 20 dB is achieved at the resonant frequency (see Figure 12(a)). Bandwidth and slot location were, as expected, nearly the same as for the single slot/dipole structure. Patterns for the coplanar waveguide fed dipoles are shown in Figure 12. Dipole separation was such that H-plane nulls should exist at +39° from broadside. Since no nulls are evident, it appears that the feed slots are participating in the radiation such that the effective radiating centers of the dipole/slot combination are closer to each other than the physical distance between the dipoles. As a check of this hypothesis, the feed locations were shifted so that the slots pass under the dipoles one quarter dipole length from the dipoles' ends. This reduces the coupling from slot to dipole and pattern nulls appear at the proper angles. For dipoles offset fed in this manner the return loss is 10 dB.

Finally, in Figure 10(b), we show crossed dipoles fed by coplanar waveguide for circular polarization. As in the second structure the slots are gradually decoupled from each other, the slot path to one dipole is then made one quarter wavelength longer than the path to the other. Each slot feeds its dipole roughly one quarter dipole length from the dipole end. A return loss of greater than 15 dB is observed at an operating frequency of 4.81 GHz (See Figure 13(a)). In Figure 13(b), pattern plots of  $E_{\theta}(\phi=0^{\circ},\theta)$ ,  $E_{\theta}(\phi=90^{\circ},\theta)$ ,  $E_{\phi}(\phi=0^{\circ},\theta)$  and  $E_{\phi}(\phi=90^{\circ},\theta)$  are presented. The coordinates  $\phi$  and  $\theta$  are defined in the usual way with respect to the  $\hat{x}$  and  $\hat{y}$  axes in Figure 10(b). From relative gain measurements at  $\phi=0.45^{\circ}$  and  $90^{\circ}$  an axial ratio of 2.8 dB is estimated.

Spurious slot radiation seems to play a role in each of the three structures tested. It is likely that this effect could be further minimized by adjusting slot width and location. Theoretical studies are currently addressing this question.

#### 4.0 SUMMARY

Two types of antenna elements for use in integrated phased arrays have been investigated. Both allow the use of two substrates, a low permittivity substrate to optimize antenna performance and a high permittivity substrate (such as GaAs) on which active devices can be fabricated. The aperture coupled patch radiates well, can be impedance matched by simple adjustment of antenna parameters, and is compatible with microstripline circuit techniques. The slot fed dipoles can be used singly with slotline feeds or in pairs with coplanar waveguide feeds, which offer good

grounding for millimeter wave devices. A circularly polarized version of the antenna has been obtained by using crossed dipoles and a coplanar waveguide feed.

#### 5.0 ACKNOWLEDGEMENT

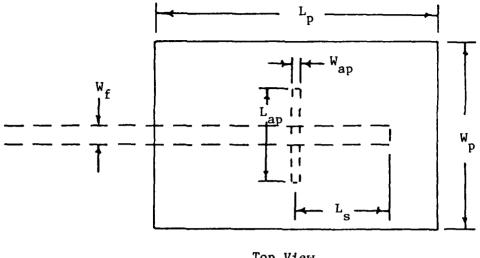
Secretary Personal Advisory ( Personal Secretary )

This work was supported by RADC/EE, Hanscom AFB, under contract No. F19628-84-K-0022.

#### REFERENCES

- Pozar, D.M. (1983) Considerations for millimeter wave printed antennas, IEEE Trans. Antennas Propagat., AP-31:740-747.
- Pozar, D.M. and Schaubert, D.H. (1984) Scan blindness in infinite phased arrays of printed dipoles, IEEE Trans.
   Antennas Propagat., AP-32:602-610.
- Pozar, D.M. and Schaubert D.H. (1984) Analysis of an infinite array of rectangular patches with idealized probe feeds, IEEE Trans. Antennas Propagat., AP-32:1101-1107.
- 4. Schaubert, D.H., Pozar, D.M., Yngvesson, K.S., and Jackson, R.W. (1984) Considerations for millimeter wave, monolithic phased arrays, Proc. 1984 Antenna Applications Sym., University of Illinois.
- 5. Pozar, D.M. (1985) Microstrip antenna aperture coupled to a microstripline, Elect. Letters, 21:49-50.
- 6. Sullivan, P.L., Schaubert, D.H., and Pozar, D.M. (1985) Analysis of aperture coupled patch antenna, Proc. 1985 North American Radio Science Meeting, University of British Columbia.

- 7. Sullivan, P.L. (1985) Analysis of an aperture coupled microstrip antenna, MS Thesis, Dept. of Electrical and Computer Engineering, University of Massachusetts.
- 8. Knorr, J.B. (1974) Slot-line transitions, IEEE Trans. on Microwave Theory and Techniques, MTT-22:548-554.



Top View

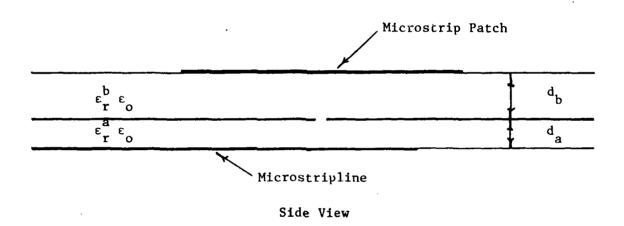


Figure 1. Aperture coupled patch antenna with microstripline feed.

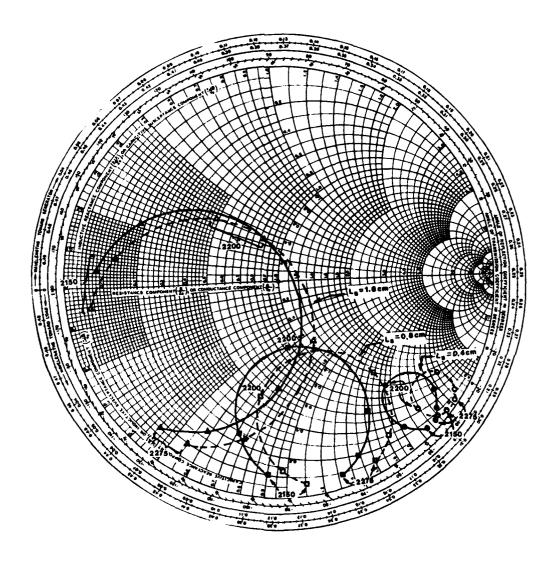


Figure 2. Measured versus calculated input impedance loci as a function of stub length.  $\epsilon_r$ =2.54,  $d_b$ =.16cm,  $L_p$ =4.0cm,  $W_p$ =3.0cm,  $L_{ap}$ =1.12cm,  $L_{ap}$ =1.15cm,  $L_{ap}$ =2.54,  $L_{ap}$ =1.16cm,  $L_{ap}$ =4.42cm.

Investment provided benefits accepted reserved

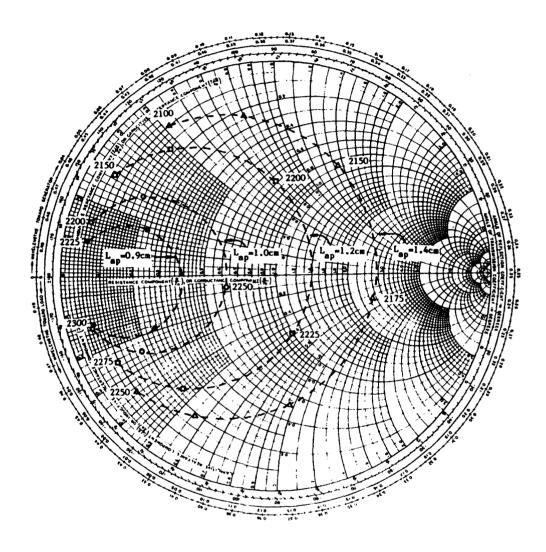
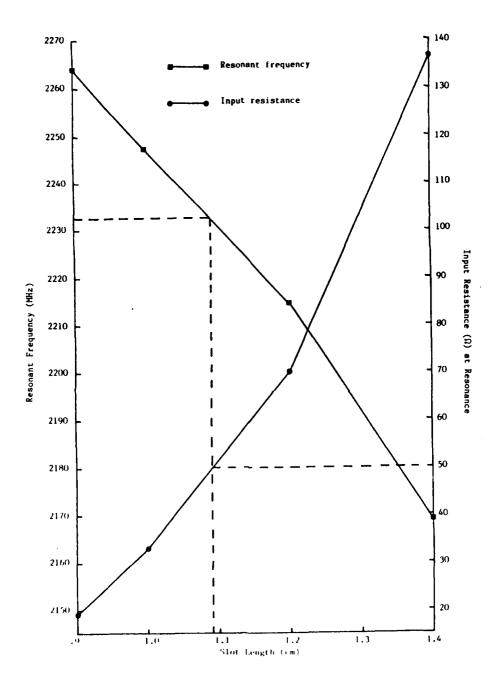
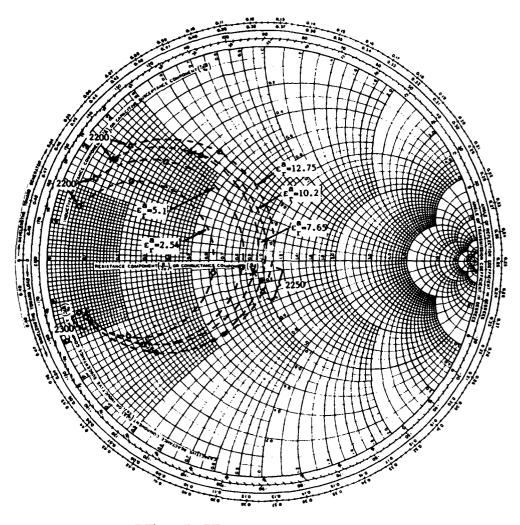


Figure 3. Calculated input impedance loci as a function of aperture length (long dimension). The other antenna parameters are:  $\epsilon_r^{=2.54}$ ,  $d_b^{=.16\text{cm}}$ ,  $L_p^{=4.0\text{cm}}$ ,  $W_{ap}^{=.11\text{cm}}$ ,  $\epsilon_r^{a=2.54}$ ,  $d_a^{=.16\text{cm}}$ ,  $W_f^{=.495\text{cm}}$ ,  $L_s^{2.0\text{cm}}$ .



THE PARTY OF THE P

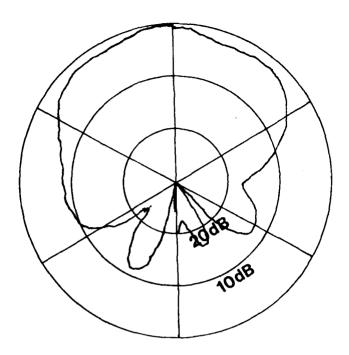
Figure 4. Resonant frequency and input resistance at resonance versus slot length (data from figure 3).



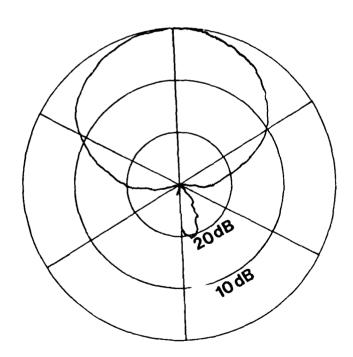
ε <mark>a</mark> r	W <sub>f</sub>	Ls
2.54	.495 cm	2.000 cm
5.10	.310 cm	1.493 cm
7.65	.225 cm	1.255 cm
10.20	.173 cm	1.108 cm
12.75	.139 cm	1.004 cm

Figure 5. Calculated input impedance loci as a function of feed substrate dielectric constant. The tabular data above give the feed line width and stub length used in the analysis to maintain a 50  $\Omega$  characteristic impedance and stub length of .22 $\lambda_f$  for each value of  $\epsilon_r^a$ . The other antenna parameters are:

 $\varepsilon_{r}^{b}=2.54$ ,  $d_{b}.16em$ ,  $L_{p}=4.0em$ ,  $W_{p}3.0em$ ,  $L_{ap}=1.0em$ ,  $W_{ap}=.11em$ ,  $d_{a}=.16em$ .

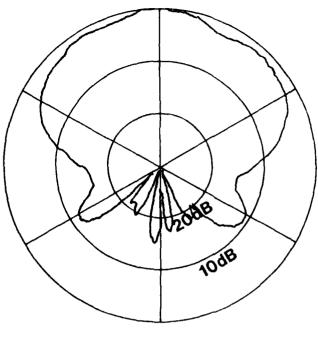


E Plane

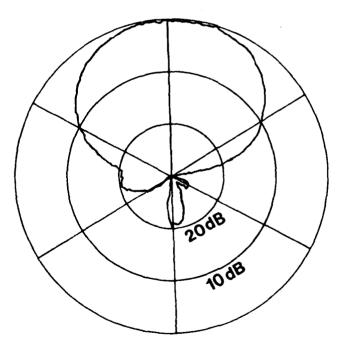


H Plane

Figure 6. Radiation patterns of 4.17 GHz antenna.  $\epsilon_r^b$ =2.2,  $d_b$ =.16 cm,  $L_p$ =2.17 cm,  $W_p$ =3.0cm,  $L_{ap}$ =1.0 cm,  $W_{ap}$ =.16cm.

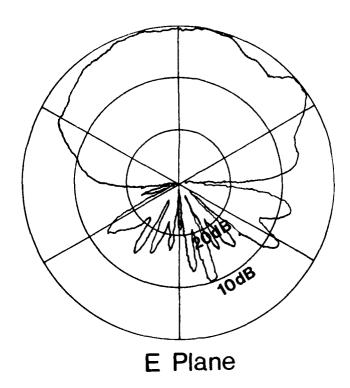


E Plane



H Plane

Figure 7. X-band (9.65 GHz) aperture coupled patch with high permittivity feed substrate.  $\epsilon_r^{D}=2.2$ ,  $d_{D}=.05$ cm,  $L_{D}=.94$  cm,  $W_{D}=1.28$ cm,  $L_{ap}=.35$ cm,  $W_{ap}=.09$ cm,  $\epsilon_r^{D}=10.2$ ,  $d_{D}=.06$ cm,  $W_{C}=.06$ cm,  $W_{C}=1.83$ cm.



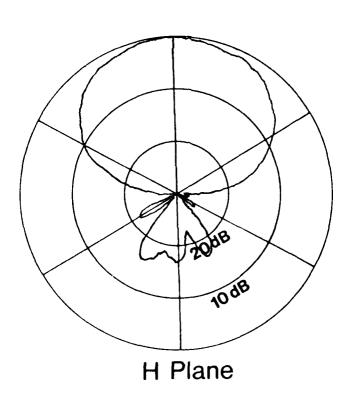
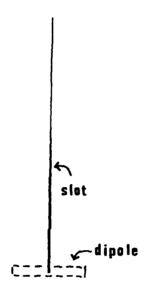


Figure 8. 16.68 GHz radiation patterns.

adali essesse. Valadaa essesse essesselulunidad valadas issesse valadaa issoosoo issessen posses

$$\epsilon_r^b = 2.2$$
, d = .05cm, L = .52cm, W = .7cm, L ap = .115cm, W ap = .08cm,  $\epsilon_r^a = 10.2$ , d = .64cm, W = .06cm, L = .44cm.



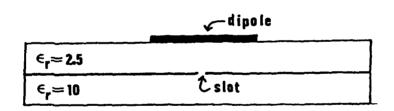


Figure 9 Single slot-fed dipole.

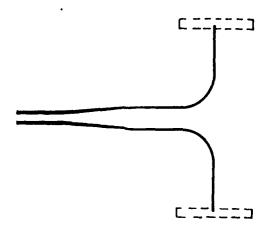


Figure 10(a) Coplanar waveguide feeding two dipoles.

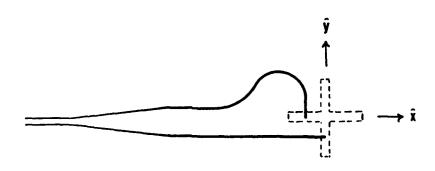
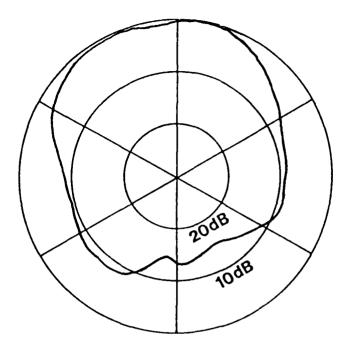
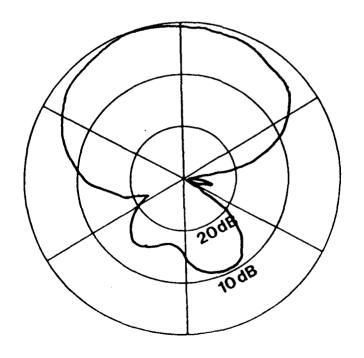


Figure 10(b) Coplanar Waveguide feeding crossed dipoles for circular polarization  $% \left( \frac{1}{2}\right) =\frac{1}{2}\left( \frac{1}{2}\right) +\frac{1}{2}\left( \frac{1}$ 



E Plane



H Plane

Figure 11 Pattern of single slot fed dipole.

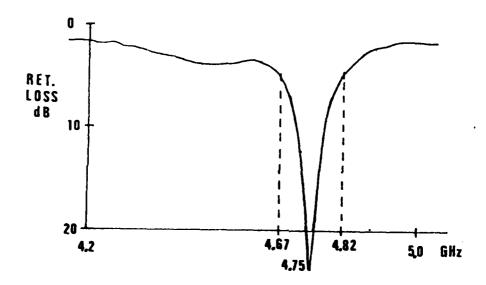
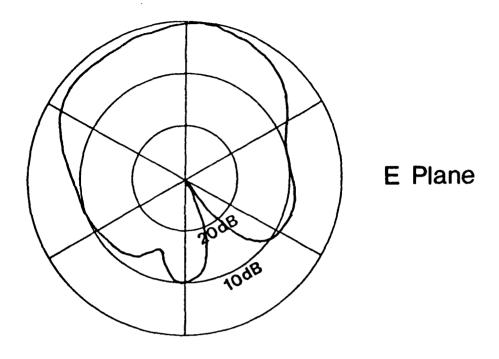


Figure 12(a) Return loss of dipoles center-fed by coplanar waveguide.

CONTRACTOR OF STATES AND STATES OF S



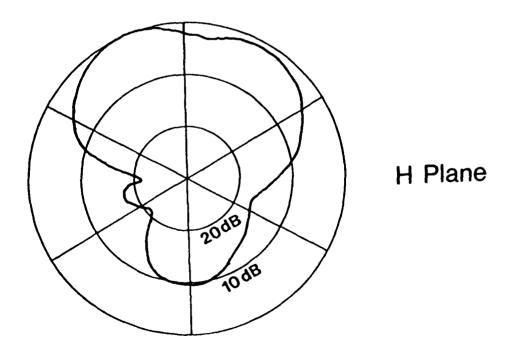
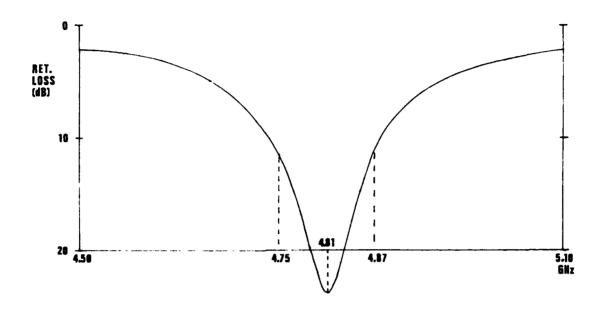


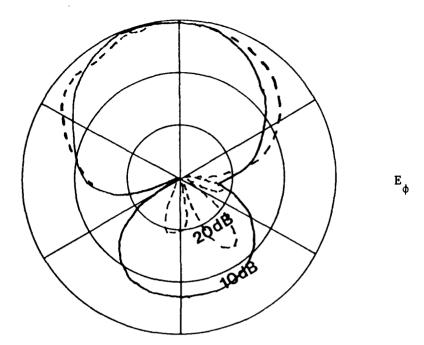
Figure 12(b). Pattern of two dipoles fed by coplanar waveguide



Consideration and the state of the state of

SSOIL LASSESSEE MOSSOSO JUNGSER

Figure 13(a). Return loss for crossed dipoles.



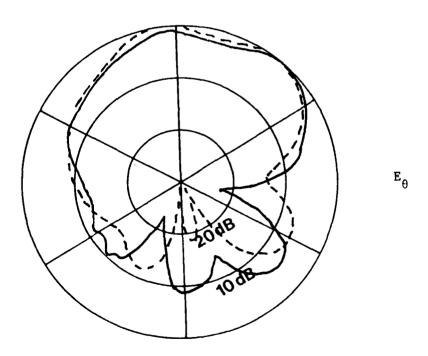


Figure 13(b)  $E_{\phi}$  and  $E_{\theta}$  patterns for crossed dipoles  $(---\phi = 90^{\circ}, -----\phi = 0^{\circ})$ 

# CROSS POLARIZATION CONSIDERATIONS FOR MICROSTRIP ANTENNA ARRAY MODULES

M. L. Oterhart Y. T. Lo

Electromagnetics Laboratory University of Illinois Urbana, IL

R. Q. H. Lee

Lewis Research Center NASA Cleveland, OH

### **ABSTRACT**

It is well known that the radiation characteristics of a microstrip antenna can be accurately predicted by using the cavity model theory in which the fields beneath the patch are represented as an infinite sum of the cavity modes. Using the equivalence theorem the antenna radiation pattern can then be written as a function of those cavity modes which are actually excited and their individual magnitudes. Usually a low order cavity mode is strongly excited for producing the intended radiation pattern. However, many other modes may contribute to the undesirable cross+polarized far field. In general, the excitation of any particular mode will depend upon the location of the feed point, the thickness of the dielectric substrate, the frequency of excitation, and the aspect ratio of the conducting patch (assuming a rectangular patch). For some particular feed locations though, the dependence upon substrate thickness and aspect ratio can significantly be reduced. In general, using the cavity model theory of isolated patches, an analysis is performed to determine these dependences. Although this technique may not be very accurate for some array structures, it is very simple and does provide significant physical insight into the nature of the cross polarization problem thereby lending itself development of simple methods by which cross polarization can be effectively reduced.

### 1. Introduction

Because of their compactness, conformability, and ease of fabrication there is currently substantial interest in the use of microstrip patches as the elements of antenna arrays. implementation makes use of an array of modules in which each module is comprised of four rectangular patches and a microstrip feed network. Analytical and empirical evaluation of the module radiation characteristics has shown that significant levels of undesired cross polarized far field can exist, depending upon the thickness of the dielectric substrate, the patch aspect ratio, the frequency of operation, and the patch feed point. In fact, it is well known, for example, that when nearly square patches are excited at particular feed points the two cross polarized components of the electric field radiated broadside to the antenna are equal in magnitude and 90° out of phase, thereby resulting in circular polarization, instead oflinear Hence, the purpose of this paper is to show polarization [1]. that, as in the case of patches producing circular polarization for instance, the cavity model theory can be utilized to understand the cross polarization problem of patches intended for radiation of linear polarization and to suggest remedies for it.

# 2. Theory

STATES SALVES TO SALVES TO

First we briefly review the cavity model theory of microstrip antenna radiation [2-3]. Consider a rectangular patch of dimensions axb on a grounded dielectric substrate with

dielectric constant  $\epsilon_r$  and dielectric loss tangent 6 as shown in Figure 1. In modelling the structure, the electric field beneath the patch is assumed to have only a component which lies perpendicular to the ground plane and patch and which is invariant in that direction. The tangential magnetic field at the edges of the patch are assumed to be zero and, therefore, that the perimeter is enclosed by a magnetic wall. By applying Huygen's theorem, an equivalent magnetic current ribbon is defined at the patch edge, combined with its image, and then considered as radiating in the absence of the dieletric slab. In general, the computed electric far field consists of an infinite summation, the mn<sup>th</sup> term of which is proportional to:

$$A_{mn}(\theta,\phi) = \frac{\Psi_{mn}(x',y') \cdot j_{0}(m\pi d/2a)}{k^{2} - k_{mn}^{2}}$$
(1)

where  $\Psi_{mn}$  (x',y')=  $\cos(m\pi x'/a)\cos(n\pi y'/b)$ ,  $j_{o}(x)=\sin(x)/x$ ,  $k^{2}=\omega^{2}\mu_{o}\varepsilon_{o}(1-j\delta_{eff})\varepsilon_{r}$ ,  $k^{2}_{mn}=(m\pi/a)^{2}+(n\pi/b)^{2}$ , x',y' = patch feed point coordinates, a= patch length, b= patch width,  $\delta_{eff}=effective$  dielectric loss tangent,  $\Lambda_{mn}(\theta,\phi)=angular$  coefficient.

AND TANKS OF THE PROPERTY OF T

However, as the operating frequency  $\omega$  approaches the resonant frequency of a particular mode mn, the real part of the intrinsic wavenumber k and the resonant wavenumber  $k_{mn}$  will be equal thereby causing the mn<sup>th</sup> term of the series to become dominant over all others provided of course that  $\Psi_{mn}(x^*,y^*)_{\neq 0}$ . For

typical values of patch aspect ratio  $(1.0 \le a/b \le 2.0)$  the two lowest order cavity modes (disregarding the DC mode mn=00) are the mn=10 and mn=01 modes. It has been shown that under the condition that a≥b , the latter of these two is the more efficient as it results in higher radiation [4]. Given that the operating mode corresponds to mn=01, the cavity model theory also predicts that only modes of the form mn=m0 can significantly contribute to the cross polarized far field. The denominator of (1) also contains an imaginary term which is determined by lumping the radiation, surface wave, copper, and dielectric losses into a single "effective dielectric loss tangent",  $\delta_{\text{eff}}$ . To do so, the copper and dielectric losses are found from the magnetic and electric energies stored beneath the patch, and the radiation loss is determined from the integration of the Poynting vector over a closed surface located in the far field. surface wave loss is similarly determined by far field integration except that use is made of the Green's function for an infinitesimal magnetic dipole located on the surface of the dielectric substrate. To see how frequency, aspect ratio, feed point location, and beff contribute to the cross polarized far field, consider the ratio of the radiated fields corresponding to the 01 and m0 modes as given by (1):

CONTRACTOR OF THE PROPERTY OF

$$\frac{E_{01}}{E_{m0}} = \frac{\Psi_{01}(x',y')}{\Psi_{m0}(x',y')} = \frac{\kappa^2 - \kappa_{m0}^2}{\kappa^2 - \kappa_{01}^2} = \frac{1}{J_0(m\pi d/2a)} = \frac{A_{01}(\theta,\phi)}{A_{m0}(\theta,\phi)}.$$
 (2)

In order to maximize this expression and thereby minimize cross polarized radiation, consider first the frequency dependent term in the denominator,  $k^2 - k_{01}^2$ . Recalling that k can be written as  $k'(1-j\delta_{eff})$ , where  $k'=\omega\sqrt{\mu_0\epsilon_0\epsilon_r}$ , one can obtain the frequency which minimizes the magnitude of  $k^2-k_{01}^2$  by setting the first derivative with respect to k' of the magnitude equal to zero and solving for k'. Doing so yields  $k' \notin k_{01}$ , for  $\delta^2 \leqslant 2/3$ . Using this value of k', (2) becomes:

$$\frac{E_{m1}}{E_{m0}} = \frac{\Psi_{01}(y')}{\Psi_{m0}(x')} \left( \frac{j}{2\delta_{eff}} \left( 1 - (mb/a)^2 \right) + 1 \right) \frac{1}{j_{o}(m\pi d/2a)} \frac{A_{01}(\theta, \phi)}{A_{m0}(\theta, \phi)}.$$
 (3)

Notice that for  $\Psi_{01}(y^*) \neq 0$  and  $a/b \neq m$ , the ratio tends to infinity as the effective loss tangent tends to zero. Similarly, under the condition that  $\Psi_{01}(y^*) \neq 0$ , the ratio tends to infinity as  $\Psi_{m0}(x^*) = \cos(m\pi x^*/a)$  tends to zero (i.e., as  $m\pi x^*/a$  tends to an odd multiple of  $\pi/2$ ).

# 3. Theoretical and Experimental Results

pred estimate properties assessed influences assessed assessed assessed

Numerous experimental single patch and four element modules were implemented and tested in the frequency range of 3.7 to 4.0 GHz using Rexolite 2200 circuit board ( $\epsilon_r$ = 2.62, dielectric loss tangent  $\delta$ = 0.001). Both microstrip and coaxial line feed types were used with no noticeable difference appearing in the pattern measurements. In computing the theoretical data, the actual, physical dimensions a and b were increased by a factor

approximately equal to t, as determined from previous results. In Figure 2, theoretically and experimentally determined cross polarized far field levels are compared as a function of aspect ratio. As one would expect from the previous discussion, cross polarized radiation is minimized when the aspect ratio takes on the value 1.5 and is greatest for values near 1.0 and 2.0. Nevertheless, given that an aspect ratio such as a/b= 2.0, for example, results in a degeneracy of the 01 mode and the undesired 20 mode, one can easily reduce the cross polarized radiation to a level comparable to that for which a/b= 1.5 by using mode supression pins. In Figure 3a, it can be seen that placement of shorting pins along the nodal line of the O1 mode electric field distribution effectively suppresses the cross polarization producing modes immediately above and below the 01 mode but leaves the 01 modal field unaffected. Even when the operating frequency is increased or decreased by as much as 3.0%, the effects of the pins remains significant as can be seen in Figure 3b.

For the case of the four element module, two basic microstrip feed networks are depicted in Figure 4a. In one network the antenna is fed on the "a" side of each element whereas in the other it is fed on the "b" side. Both types of modules have been implemented and tested, although attention will focus on the latter since it is simpler in construction and it provides a simple mechanism by which the array may be matched to 50 ohms. Because the 01 mode results in a sinusoidal variation

of the electric field along the "b" side of each patch, the feed points of the elements on the second module may be simultaneously shifted left or right in order to achieve a desired impedance value. Figure 4b illustrates the results of having made use of this fact in one implemented module. In Figure 5, measured effects of varying patch aspect ratio for a particular array module are shown, and in Figure 6 it is seen how short open circuited stubs can be used to simulate a change in aspect ratio thereby resulting in a reduction of cross polarized radiation as well.

# 4. Conclusions

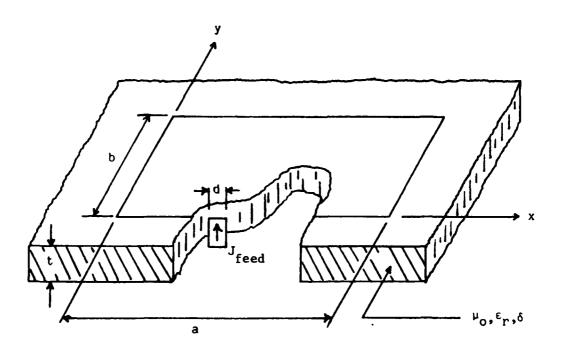
- (1) Despite the fact that this theory concerning cross polarization is based upon the cavity model theory, which is valid only for thin substrates, the results indicate that it is still applicable for dielectric thicknesses as much as 0.032 dielectric wavelengths ( $\lambda_{\rm f}$ ).
- (2) The application of the theory is not restricted solely to the case of isolated patches but can be applied to the case of array modules in which the elements are spaced by a fraction of a free space wavelength.

# 5. References

- [1] Y. T. Lo, B. Engst, R. Q. Lee, "Circularly polarized microstrip antennas," Proc. of the 1984 Antenna Applications Synposium at Allerton Park, University of Illinois, Urbana, IL.
- [2] Y. T. Lo, W. F. Richards, "Theory and experiment on microstrip antennas," IEEE Trans., AP-27, pp. 1377145, Mar. 1979.
- [3] W. F. Richards, Y. T. Lo and D. D. Harrison, "An improved theory for microstrip antennas and applications," IEEE Trans., AP-29, pp. 38-46, Jan. 1981.
- [4] Y. T. Lo, et al., "Study of microstrip antenna elements, arrays, feeds, losses, and applications," Final Technical Report, RADC-TR-81-98, June 1981.

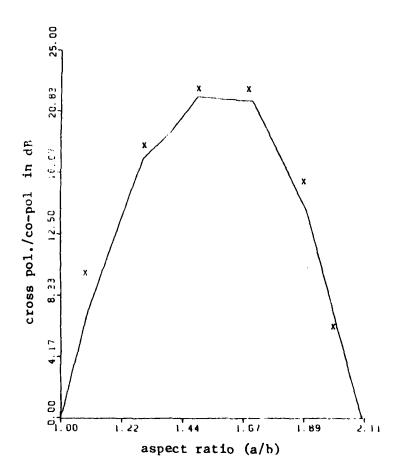
# Acknowledgement

This work is supported by Lewis Research Center, NASA, Cleveland OH.



feed point location = (x',y')

Figure 1. Rectangular microstrip antenna geometry and idealized feed.



X theory
-- experiment

f = 3.8 GHz feed point at  $x^*$ = 0.0 cm.,  $y^*$ = 0.7 cm. b= 2.27 cm. t= 0.032  $\lambda_E$ 

AND REPORTED COCKECCAL EXCESSES COCCERCA

Figure 2. Comparison of the measured and theoretically predicted attenuation of the cross polarized radiation level.

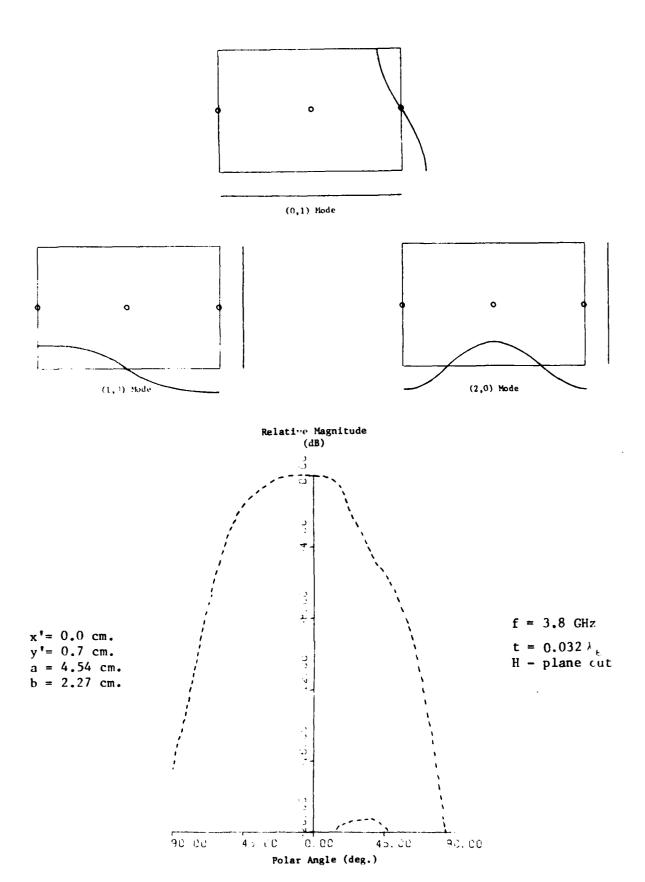
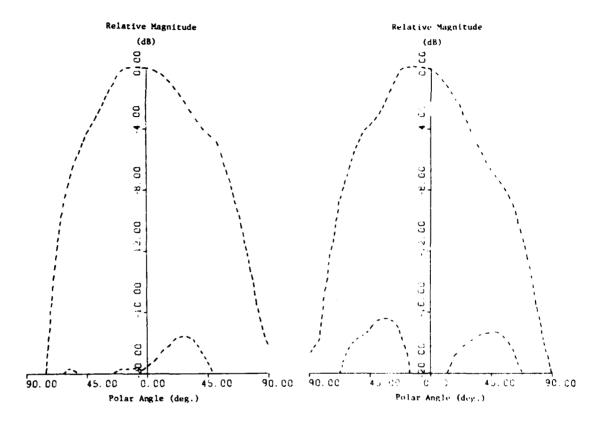


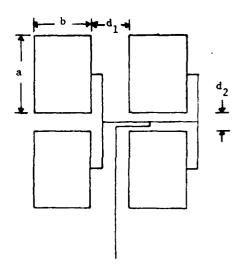
Figure 3a. Use of mode suppression pins for the case of a patch with aspect ratio a/b= 2.0.



$$f = 3.69 \text{ GHz}$$

$$f = 3.91 \text{ GHz}$$

Figure 3b. Measured patterns obtained while using mode suppression pins and exciting the patch both above and below the 0,1 mode resonant frequency (3.8 GHz).



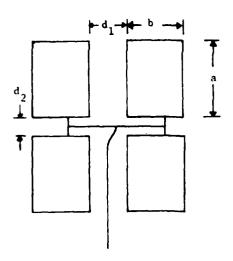
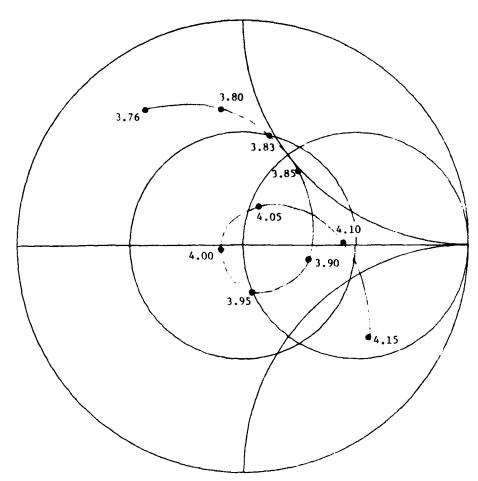


Figure 4a. Two microstrip feed networks for the four element array module.



Frequencies in GHz.

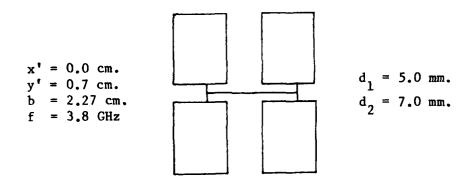
a= 3.0 cm. b= 2.24 cm. substrate thickness=  $0.017 \lambda_{\epsilon}$ 

50  $\Omega$  feed lines x' = 0.0 cm. y' = 0.7 cm.

Bandwidth (VSWR  $\leq$  3.0) = 7.1%

 $d_1 = 7.0 \text{ mm.}$   $d_2 = 7.0 \text{ mm.}$ 

Figure 4b. Measured input impedance locus of an array module consisting of patches fed on the "b" side.



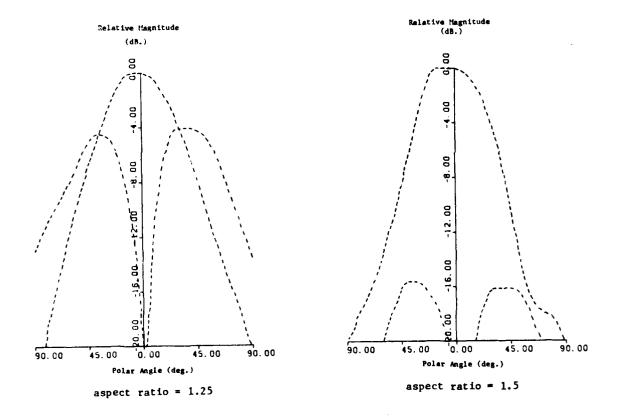
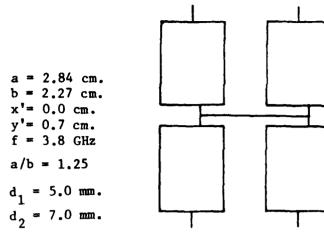


Figure 5. Reduction of cross polarized radiation obtained by varying the aspect ratio a/b, in the case of the four element array module. Substrate thickness=  $0.032\lambda_{\odot}$ , H- plane cut.



stub location = b/2.0stub length = 5.0 mm.

Zo stub =100  $\Omega$ 

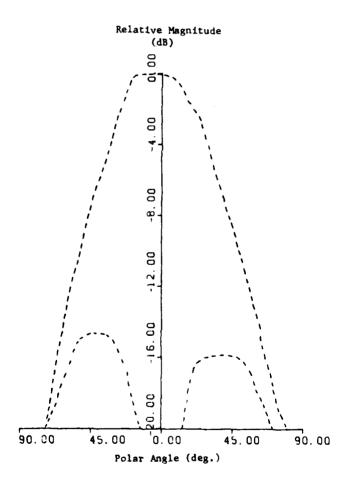


Figure 6. Reduction of the cross polarized radiation through the use of short open circuited stubs. Substrate thickness is  $0.032\,\lambda_{E}$ , H- plane cut.

# Ku-Band High Gain Microstrip Planar Array for TDRSS

Farzin Lalezari and Charles Gilbert Ball Aerospace Systems Division Boulder, CO

#### **ABSTRACT**

A high gain microstrip planar array to be used in the TDRS (Track-ing/Data Relay Satellite) system has been developed at Ku-Band for NASA-GSFC Contract #NAS5-28032. The antenna is circularly polarized and employs a patch rotation scheme to more than double the 3 dB axial ratio bandwidth and the 2:1 VSWR bandwidth. A bandwidth of 4.5% was achieved on 0.015 inch Teflon-fiberglass material centered about 14.8 GHz. The increase in bandwidth can best be explained in terms of circular polarization ellipses. The increase in impedance bandwidth is due to the impedances of each patch not adding in phase. Thus, an array of 64 x 64 elements was built and tested based on these principles and we achieved 4.5% bandwidth and 39 dBic gain.

Also, a Ku-band tracking system was included in the same aperture. A coarse and fine ( for both elevation and azimuth), sum and difference monopulse tracking was employed and were mounted around the perimeter of the main aperture.

#### 1.0 Introduction

A Ku-band high gain planar microstrip array has been developed at Ball Aerospace Systems Division using a unique patch rotation scheme. This work was sponsored by NASA/Goddard Space Flight Center under Contract #NASS-28032. First of all, the patch rotation scheme will be explained in terms of axial ratio ellipses and impedance. Secondly, the performance of one of the sixteen panels will be reviewed. Next the overall structure of the antenna will be described. Then the waveguide feeding structure will be detailed. Finally, the monopulse tracking system will be discussed. Also, in Phase II of this contract an S-band data link for the TDRSS system is being developed and this antenna will be briefly mentioned.

#### 2.0 Patch Rotation Scheme

The basis for this antenna and its relatively wide bandwidth is the patch rotation scheme. In general, a microstrip patch etched on 0.015 inch teflon-fiberglass will have 1.5 to 2.0% bandwidth. However, by rotating the patches a greater than two-fold increase in both VSWR (inside 2.0:1) and axial ratio (less than 3 dB) will be realized. The improvement in axial ratio can best be explained in terms of axial ratio ellipses as will be done below. The increased VSWR bandwidth will be shown in terms of a Smith Chart. The axial ratio ellipse explanation will be given first followed by the VSWR improvement explanation.

Consider two circularly polarized microstrip patches spatially rotated  $90^{\circ}$  with respect to each other. Figure 1 shows this arrangement. Near the center frequency the axial ratio is small so consider these patches at their band edge, where the individual patches have an axial ratio of 3 dB. The axial ratio ellipses may be drawn as shown in Figure 2.

Thus, the major axis of the first ellipse adds to the minor axis of the second ellipse and vice versa. So the net axial ratio theoretically is back to 0 dB even though the individual microstrip patches have a 3 dB axial ratio. In practice things are not perfect and so one does not achieve 0 dB axial ratio everywhere; however, there is substantial improvement in the axial ratio bandwidth. Factors such as nonidentical patches, finite array size and phase offset error all contribute to limiting the bandwidth. As can be seen in Figure 1, since the patches are spacially rotated  $90^{\circ}$ , the phase must be offset  $90^{\circ}$ to compensate for this. This offset is produced by making the path length 90° longer to one patch than the other. Of course this electrical offset is 90° only at the center frequency and so at the band edge of a single element (as in the above example) there is already a phase error, thus the ellipses do not add to completely neutralize the axial ratio. Then as one goes further and further beyond the center frequency this phase error becomes larger and larger, thereby limiting the axial ratio bandwidth. Hence this is the manner in which the axial ratio bandwidth is increased, the impedance bandwidth will be detailed next.

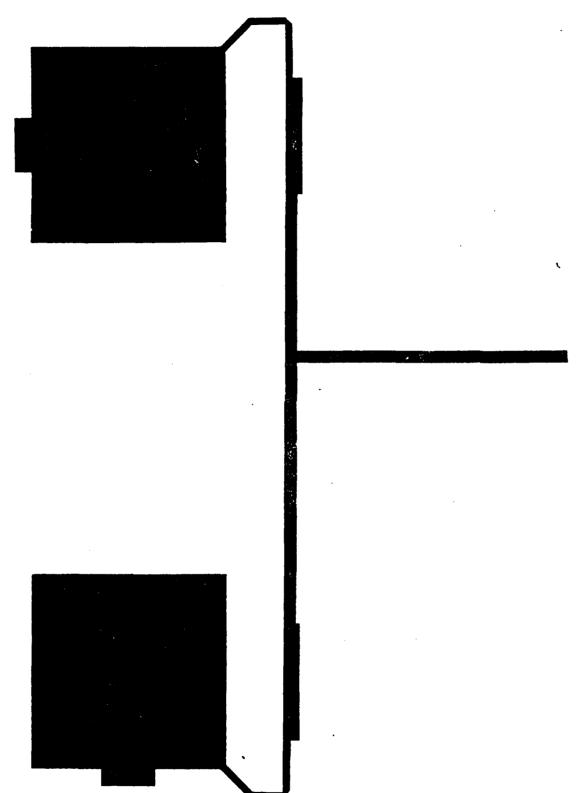


Figure 1. Pair of Rotated Circularly Polarized Microstrip Patches

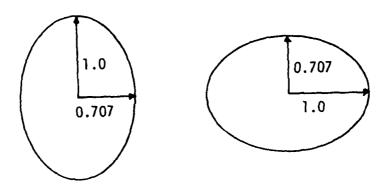


Figure 2. Axial Ratio Ellipses

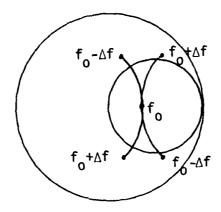


Figure 3. Microstrip Patch Impedances  $90^{\circ}$  Out of Phase

The improvement in impedance bandwidth can best be shown by an example. Suppose that one had two microstrip patches each matched to  $100~\Omega$  but out of phase by  $90^{\circ}$ . On a Smith Chart these impedances would look like the following in Figure 3, where the center frequency  $(f_0)$  crosses the real axis on the 2:1 circle. Then choosing some arbitrary bandwidth  $\Delta F$ , since the curves are rotated by  $90^{\circ}$  the low end of the bandwidth is higher in impedance than  $100~\Omega$  and capacitance in one case and lower than  $100~\Omega$  and inductive in the other. Thus choosing a point on these curves and adding them in parallel will show that the reactive portions of the impedance tend to cancel out, thereby increasing the bandwidth (i.e., smaller VSWR) over the case when the patches are not  $90^{\circ}$  out of phase. If the  $F_0$ - $\Delta F$  impedance point on the first curve is  $Z_1$  = 2.2-j0.8 and the second curve is  $Z_2$  = 1.8 + j0.8 then the parallel combination is the following:

$$Z_{\text{total}} = \frac{Z_1 Z_2}{Z_1 + Z_2} = \frac{(2.2 - \text{j}0.8)(1.8 + \text{j}0.8)}{2.2 - \text{j}.08 + 1.8 + \text{j}0.8} = \frac{4.6 + \text{j}0.32}{4}$$
 (1)

$$Z_{\text{total}} = 1.15 + j0.09$$

and seconds presently principles operated property of the property of the present of the property of the prope

This is very close to the center of the chart where we want to be. Now to compare this to the case where the impedances are the same (i.e., no  $90^{\circ}$  phase difference) we have

$$Z'_{total} = \frac{Z_1 Z_2}{Z_1 + Z_1} = \frac{(2.2 - j0.8)(2.2 - j0.8)}{22.2 - j0.8 + 2.2 - j0.8} = \frac{4.2 - j3.52}{4.4 - j1.6}$$
(2)

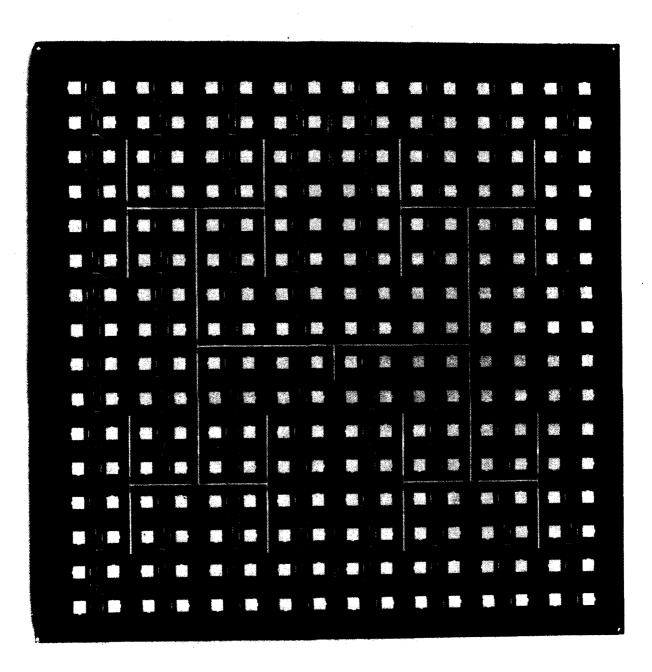
 $Z'_{total} = 1.1-j0.4$ 

CONTRACTOR CANDACTOR

Thus, one can easily see that since the reactive part of  $Z'_{total}$  is much larger than  $Z_{total}$  that  $Z'_{total}$  will have a larger VSWR. In other words the bandwidth is increased by rotating the patches and then compensating for this spatial rotation by an electrical  $90^{\circ}$  phase difference. The axial ratio bandwidth is increased as explained above as is the VSWR bandwidth by more than a factor of two. So the improved bandwidth and axial ratio have been detailed; now the actual performance of a  $16 \times 16$  subarray panel will be discussed.

# 3.0 Subarray Development and Performance

Once one develops a pair of patches as described above, one can quickly build up to a  $16 \times 16$  element subarray level. First of all, a  $2 \times 2$  must be developed where each patch is  $90^{\circ}$  out of phase with the adjacent patches. This produces a  $0^{\circ}$ ,  $90^{\circ}$ ,  $180^{\circ}$ ,  $270^{\circ}$  phase rotation around the  $2 \times 2$  cluster. One needs to be careful to get the sense of this rotation the same as the polarization sense of the patches (either right hand or left hand) or else a null will occur at broadside. Once this  $2 \times 2$  cluster is developed however, another slightly different but equivalent  $2 \times 2$  cluster must be made in order to facilitate the feed lines in the corporate power divider. Finally, once this small obstacle is overcome it is simply a matter of arraying these  $2 \times 2$  clusters in a straight forward corporate feed manner. A photograph of a completed subarray is shown in Figure 4. The performance of this subarray is as follows:



84-626

Figure 4. 16 X 16 Subarray Panel

Bandwidth Center Frequency Sidelobe Level

Gain

650 MHz or 4.5%
14.8 GHz
>12 dB down from peak of
main beam
29.0 dBic

A typical VSWR and typical principle plane antenna patterns are shown in Figures 5, 6, and 7. After the subarray panel design was complete we then had to make a  $4 \times 4$  array of these subarray panels.

# 4.0 Full Array Configuration

The complete array is shown in Figure 8. It is made up of a  $4 \times 4$  array of subarray panels mounted on 0.25 inch honeycomb with 0.005 inch fiberglass backing. The monopulse tracking antennas are also shown and these will be discussed in a later section. Other mechanical specifications of this array are as follows:

Size Weight Thickness

SOCIAL POPULARIO PROPERTY PROPERTY SERVICES CONTINUE BOUNDED SERVICES

<10 lbs
 51 inches x 51 inches
<2 inches</pre>

As this antenna is for a space application, weight and volume were minimized. The feeding structure for each of the subarray panels was attained using waveguide.

# 5.0 Waveguide Power Divider/Combiner

Each of the subarray penels in the array were fed through a WR-51 waveguide power divider. A section of the waveguide power divider to feed 4 subarrays is shown in Figure 9. This four-way waveguide power



PROJECT NO	PROGRAM	
PART NO.	MODEL NO.	SERIAL NO.
	JALIFICATION ACC	
EDECLIENCY RANG	E 14.625 to 15.25	SHEET OF

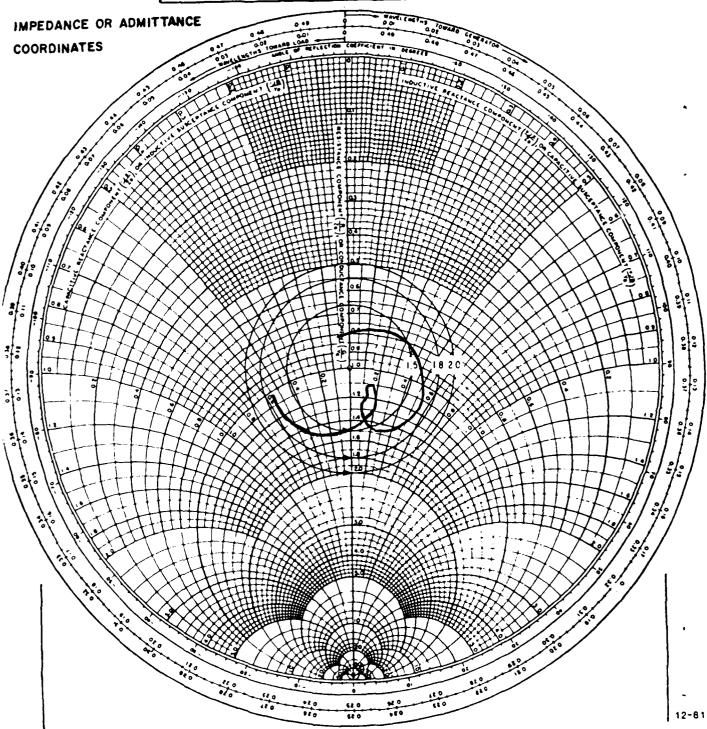


Figure 5. VSWR of Typical 16 X 16 Element Panel

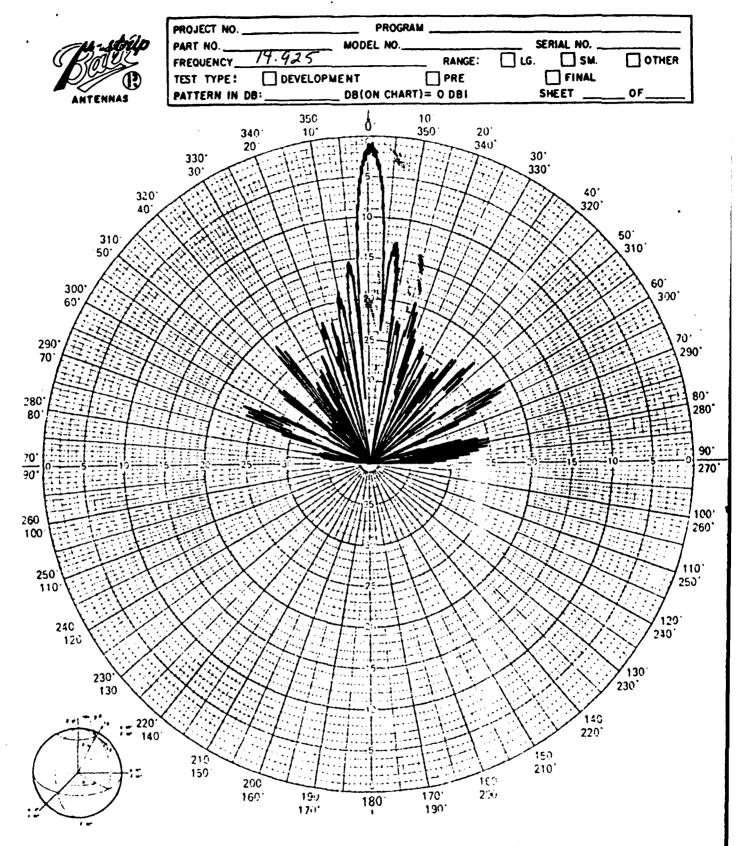


Figure 6. Principle Plane Cut of 16 X 16 Element Panel

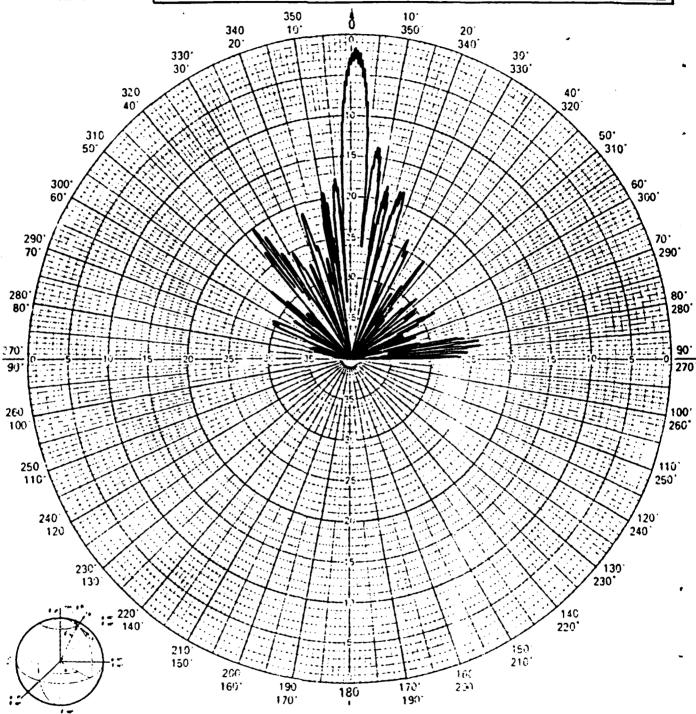


Figure 7. Orthogonal Plane Cut of 16 X 16 Element Panel

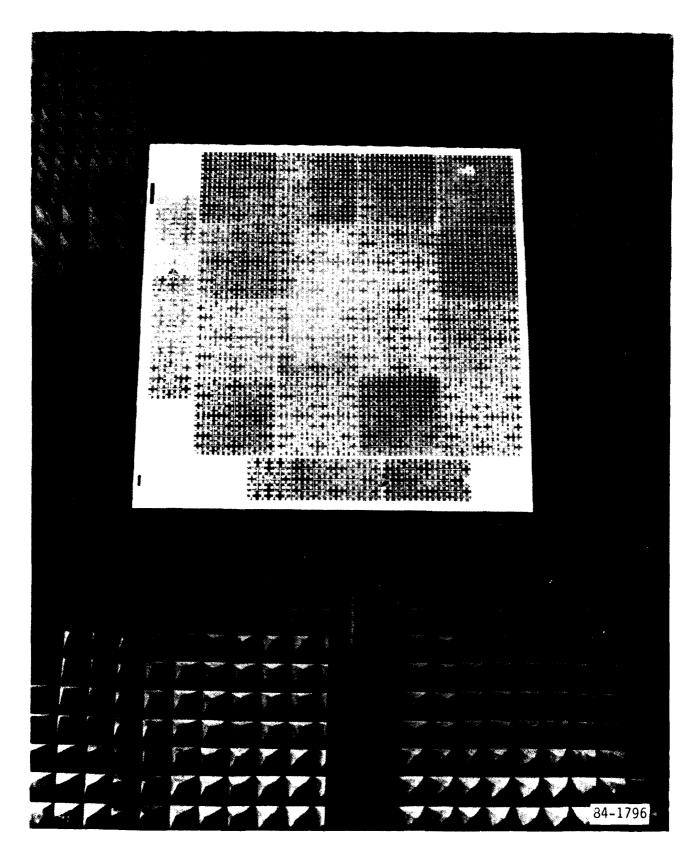


Figure 8. Complete Ku-Band Antenna

gones transcent objected becamed societies correctly sessions.

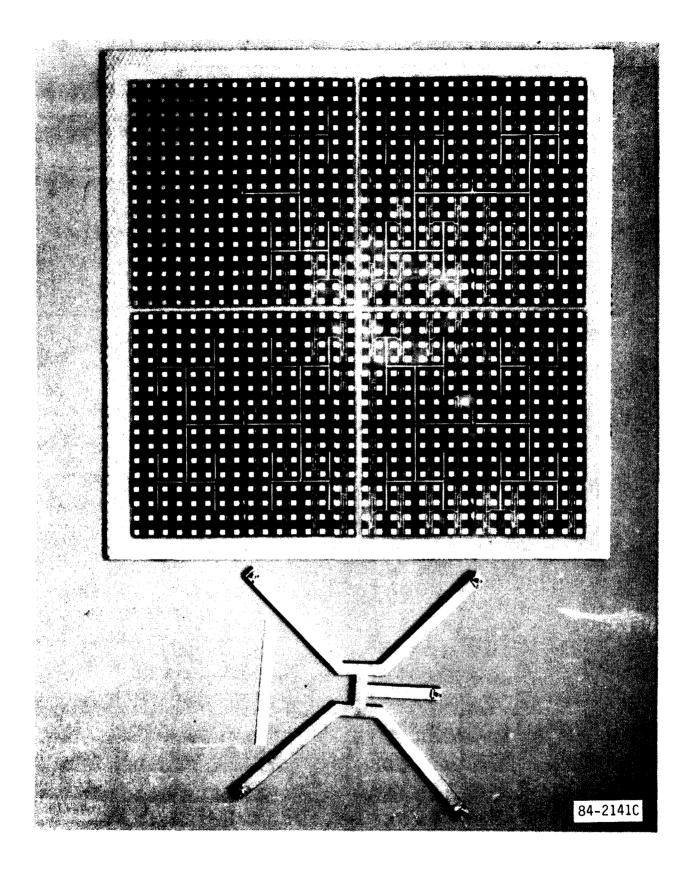


Figure 9. 4 Panels With Waveguide Power Divider

divider consists of the following design. Looking at this as a power combiner helps in explaining how it works. First of all, (assuming that the output ports are matched and their impedance is  $Z_0$ ) following two of these outputs back toward the center we see that we have  $Z_0$  in parallel with  $Z_0$  to give an impedance of  $Z_0/2$  for the right section of the structure for example. Of course the left section of the structure will have the same impedance. Then, because the point where the impedance of the two arms is  $Z_0/2$  is 3/4 waveguide wavelength from the center of the structure (where the two halves meet) this impedance is transformed to  $Z_0$ . Thus, one has  $Z_0$  in parallel with  $Z_0$  which nets  $Z_0$  and so the waveguide structure is matched. This is the principle of operation of the waveguide structure and in practise it works very well over limited bandwidths ( ~10% which was more than ample for this application).

The entire 16 way waveguide feeding structure is shown in Figure 10. Each subarray panel if fed from the waveguide via a waveguide to coaxial transition then a coax to microstrip transition to the panels. As the construction of this waveguide structure was not perfect there were significant path length differences from the center input to the 16 outputs. The maximum variation was  $40^{\circ}$  of electrical phase length. Due to the fact that we had to use coaxial jumpers anyway, this phase error was compensated for in the length of these cables. Thus, even though there are many transitions to go through, feeding with waveguide is definitely less lossy than using microstrip transmission lines for the entire array. The loss in microstrip would be over 5 dB while the loss

81 15 CONTROL (CONTROL) 15 CONTROL

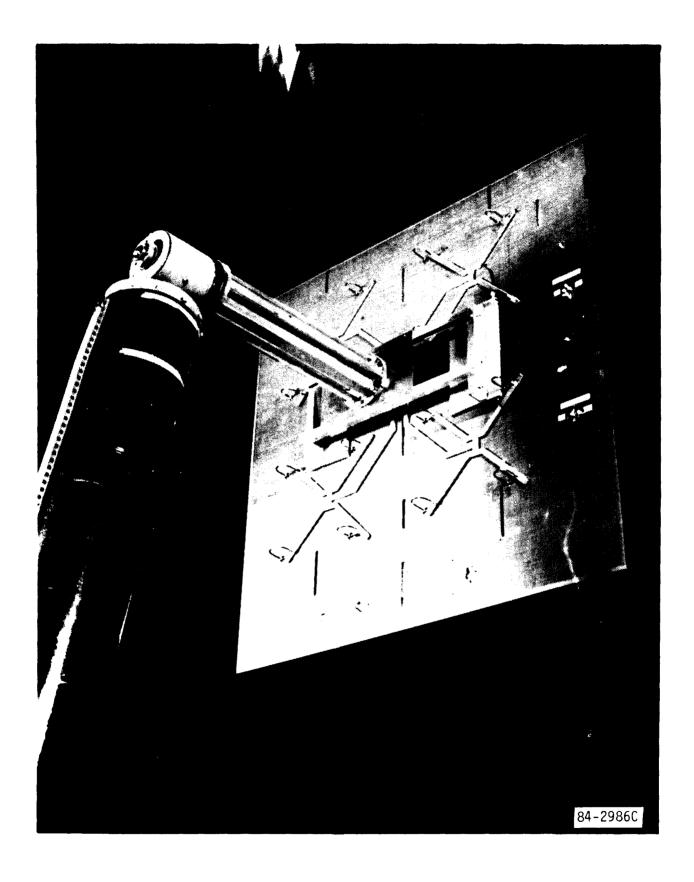


Figure 10. 16-Way Waveguide Power Divider

in the waveguide including the transitions was 1.3 dB. Therefore, the waveguide feeding structure greatly helped the efficiency of the antenna.

#### 6.0 Final Results

The main goal we had in assembling this antenna was to achieve 40 dBic gain. We missed this goal slightly as we measured only 34 dBic. We believe that there is a great deal of room for improvement, however, especially in the waveguide and the subarray panel efficiencies. All other goals were met and they were:

Bandwidth	650 MHz on 4.5%
Beamwidth (both plans)	1.0 <sup>0</sup>
Sidelobe level	>12 dB down from peak of main beam
Weight	<10 1bs
Thickness	√ inches

Thus we believe that this program was a success as we know how to improve the gain and will achieve over 40 dBic on the next iteration.

Also, it should be mentioned that the time frame for this entire project was 6 months and so we simply did not have time to refine many parameters that would have increased the gain. The final item to discuss is the tracking antennas, and this will be done in the next section.

## 7.0 Ku-Band Tracking Antennas

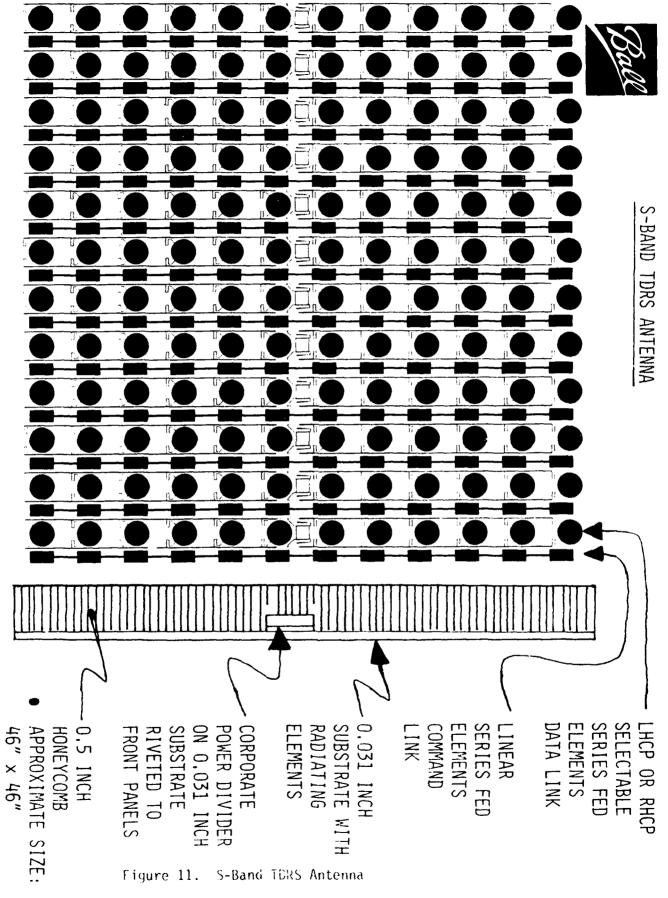
The state of the s

The tracking scheme for this antenna employed a coarse and fine monopulse sum and difference patterns. There were coarse and fine monopulse antennas in both the azimuth and elevation planes. The coarse monopulse antenna consists of an  $8 \times 8$  array of circular polarization microstrip

patches at a center frequency of 13.725 GHz. There is a circular 180<sup>0</sup> hybrid in the center feeding each half of the antenna where the other ports are the sum and difference outputs. The 180° hybrid was etched on the same material as the antenna. The coarse tracking was capable of pointing the beam to within  $+5^{\circ}$ . Since the beamwidth of the main antenna is only 10 a finer tracking system is also necessary. The fine tracking antenna consists of an 8 x 32 array of circular polarized patches with a circular  $180^{\circ}$  hybrid in the center. Due to the fact that we did not have a piece of material long enough to etch this entire array on, it had to be done in two pieces. Thus even though the 180° hybrid is printed on one of the boards, the connections are made by coaxial cable from "behind". The fine tracking antenna is capable of pointing the beam to within  $+0.1^{\circ}$ . Therefore when the coarse tracking antennas point the aperture to within +50 then the fine tracking antennas take over and point the beam to within +0.10 which is entirely adequate for a 10 beamwidth.

### 8.0 S-Band TDRSS Antenna

This antenna will perform the same function as the Ku-band antenna; however at a much lower frequency and data rate. The antenna consists of dual polarized circular microstrip patches etched on .031 inch teflon-fiberglass interlaced with linear polarized series fed microstrip patches as shown in Figure 11. The circular dual polarized patches are series fed also and the input to each column is from a  $90^{\circ}$  hybrid in the center of the column. Thus dual circular polarization is achieved with



these columns. RHCP from one port of the  $90^{\circ}$  hybrid and LHCP from the other port. These columns consistute the data link aperture and are fed from "behind" with a corporate feed network as shown in Figure 12. The command link columns are interlaced with the data link columns and due to the fact that the frequencies are fairly close together ( $f_0 = 2.2875$  GHz for the data link and  $f_0 = 2.1064$  GHz for the command link) there are no grating lobes or other spacing related problems. These columns are also fed from the "back" with a corporate power divider. The specifications that this antenna will meet are the following:

gain	28 dBic
axial ratio	1 dB
bandwidth (data link)	<u>+</u> 20 MHz
VSWR	<2:1
size	4 ft x 4 ft
thickness	≤2.0 inches
weight	≤12.0 lbs

### 9.0 Conclusion

SECOND PROCESSES (SECONDARY (SECONDARY (SECONDARY (SECONDARY)))

A high gain Ku-band antenna has been developed for use in the TDRS system that has increased bandwidth due to patch rotation. This increased both the VSWR and axial ratio bandwidth more than twofold. The overall structure is lightweight and occupies minimum volume as the antenna is for a space application. Also, a new S-band antenna has been developed for the same system. This antenna, too, is lightweight and occupies minimum volume due to its space application nature. Therefore, the two high gain planar array microstrip antennas developed at Ball Aerospace are ready to be included into the TDRS system.

CONTROL OF THE PROPERTY OF THE

# S-BAND SUBARRAY CONFIGURATION

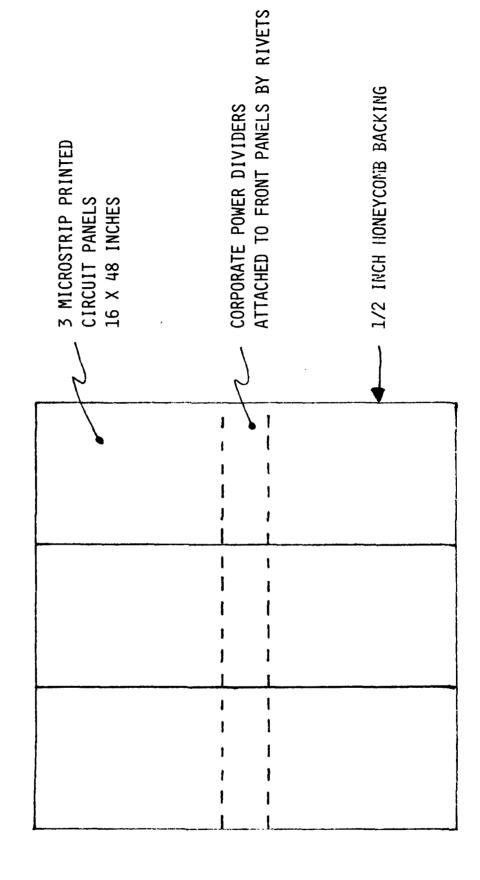


Figure 12. "Back" of S-Band TDRS Antenna

# References

 Johnson, Richard C. and Jasik, Henry Eds (1984) <u>Antenna Engineering</u> <u>Handbook</u>, McGraw-Hill, New York, Chapter 7 by Robert E. Munson. Submitted to the Symposium on Antenna Applications, September, 1985.

# DIODE GRIDS FOR ELECTRONIC BEAM-STEERING AND FREQUENCY MULTIPLICATION

Wayne W. Lam, Christina F. Jou, N. C. Luhmann, Jr., and David B. Rutledge

\*Division of Engineering and Applied Science California Institute of Technology Pasadena, CA 91125

\*\*Department of Electrical Sciences University of California, Los Angeles Los Angeles, CA 90024

### Abstract

Grids loaded with diodes are attractive because they are suitable for monolithic integration with gallium-arsenide and for high-power operation. Here we present grid designs for electronic beam-steering and harmonic generation. The beam-steering grid is a programmable reflector, where the diode bias controls the phase shift of the reflection. The variation of the phase across the aperture sets the direction of the reflected beam. The reflection loss in computer simulations is 3dB at 90GHz. The harmonic-generating grid acts as a nonlinear reactive surface, where the nonlinear capacitance of the diodes produces the harmonic frequencies. Quasi-optical filters select the desired harmonic. Computer simulations predict that a 65GHz-to-130GHz doubler would have an output power of 0.56W/cm<sup>2</sup> and a conversion efficiency of 35%.

### 1. Introduction

Periodic grids have many applications in infrared and millimeter waves [1],[2],[3]. Additional interesting applications become possible when solid-state devices are added to the grids. Tong et al. demonstrated a two-dimensional tracking array with microbolometers [4]. In this paper, we propose a varactor-diode grid that can be used in an electronically programmable beam-steering array at 90GHz or in a 65GHz-to-130GHz doubler.

In the beam-steering array (Fig. 1), the incident beam reflects off a pair of varactor-diode grids. The idea to steer the beam is to progressively shift the phase across the aperture. Changing the bias changes the grid reactance, and this controls the reflection phase. No transmission lines or waveguides are required, and this makes the design and fabrication simpler. Since the power is distributed among all the diodes, the power handling capability can be quite high.

In the doubler (Fig. 2), power at the fundamental frequency enters from the left, through a filter that passes the fundamental, but blocks the second harmonic. The power then arrives at the varactor-diode grid, and the non-linear capacitance of the diodes generates harmonics. The second harmonic leaves on the right, through another

resident, seedhee fannaar entered annaar opposit leekkost gebestel granden granden gebestel gebestel gebestel

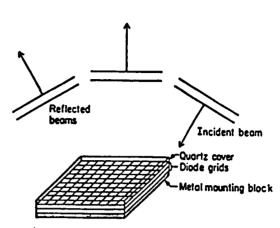


Fig. 1 Electronically programmable beam-steering array.

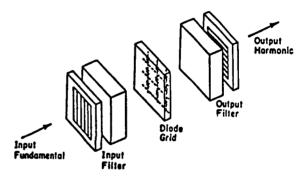


Fig. 2 Varactor-diode doubler grid.

filter that blocks the fundamental. This approach overcomes the power limitations of a single-diode multiplier because power is distributed among many diodes.

# 2. Periodic grids

The grid for these designs, shown in Fig. 3, is a square mesh of metal strips on a gallium-arsenide substrate. The diodes are located on the vertical strips. The horizontal strips provide the bias, but should not otherwise affect the circuit. We model the grids by transmission-line equivalent circuits. The grid reactance, jX, is represented by an inductive reactance in series with the diode. The substrate appears as a section of transmission line with a characteristic impedance equal to the wave impedance in the material.

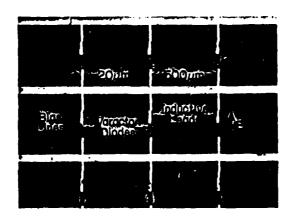


Fig. 3 Grid dimensions for a 90-GHz programmable reflector.

The inductance can be calculated by a conformal mapping [5], and is given by

$$L = \mu_0 a/(2\pi) \ln \{ \csc[\pi w/(2a)] \},$$
 (1)

where a is the grid period and w is the strip width. This formula is derived from statics. Higher order corrections have been considered for our design. They are less than 10%, and have been neglected.

The period a should be chosen somewhat smaller than a substrate wavelength to avoid exciting substrate modes. This means the period should satisfy

$$a < \lambda_0/(n+1), \qquad (2)$$

where n is the refractive index of the substrate. For gallium-arsenide substrate, which has a refractive index of 3.52, the period a should be less than  $0.22\lambda_0$ .

# 3. Electronic beam steering

The reflector design (Fig. 1), consists of a fused-quartz cover, two diode grids, and a metal mirror. The quartz cover acts as a quarter-wave matching layer. The metal mirror prevent radiation from escaping and serves as a heat sink and mechanical support.

In the transmission-line equivalent circuit model, the mirror is effectively an open-circuit, because it is a quarter-wavelength behind the back grid. At the front grid, the back grid appears as a parallel load, but with the

impedance inverted. The total normalized reactance  $X_{t}$  is the parallel combination of jX and 1/(jX), or

$$X_{t} = X/(1-X^{2}).$$
 (3)

 $X_t$  ranges from  $-\infty$  as X approaches -1, to  $+\infty$  as X approaches +1. This allows a full  $360^\circ$  phase shift.

To analyze the grid structures, together with the substrate, dielectric slabs, and mirrors, we have written an interactive graphics program called TRAP (transmission, reflection, absorption, and phase) to calculate the effect of different layers.

Fig. 4 shows a simulation of the programmable reflector. The phase variation is almost linear from -180° to +180° as the grid reactance sweeps from a normalized reactance of -1 to +1 (-1070 to +1070 for GaAs substrate). The reflection efficiency varies from a low of 0.49 to a high of 0.57, with an average loss of 2.7dB. For TE polarized waves, the best performance is at an angle of incidence 30° to 45°.

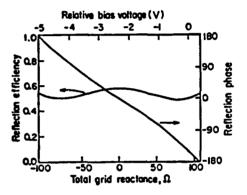


Fig. 4 Simulated results of programmable reflector.

Preliminary test of one diode grid shows a 20 phase shift per volt. This result is obtained from modulating 3 rows of Schottky diodes in the Michaelson interferometer.

### 4. Doubler

In the multiplier design (Fig.2), the proposed filters consist of a wire polarizing grid with a half-wave plate designed for the fundamental. The half-wave plate separates the fundamental from the second harmonic because it rotates the fundamental polarization by 90°, but does not alter the second harmonic polarization. This allows the polarizing grid to select the desired frequency.

Recently Siegel et al [6] have written a program to calculate the conversion efficiency of a multiplier, and we have used this program in the design. Fig. 5 shows the equivalent circuits of the multiplier. It is assumed that

the input and output polarizers can be place so that they do not affect the circuit at either frequencies. In the fundamental circuit (Fig. 5a), the grid impedance is the sum of the lead reactance, 1050 and diode impedance 40-j2250. The breakdown voltage is taken to be -5V, and this limits the input power to 4mW. In the second-harmonic circuit (Fig. 5b), the lead reactance doubles and the capacitive reactance of the diode halfes. The output power of a single diode is 1.4mW. For a grid with 400 diodes per square centimeter, the output power is  $0.56\text{W/cm}^2$ . We plan to tune the fundamental source impedance Zs and the harmonic load impedance Zt with fused-quartz plate tuners developed by Archer [7]. With these tuners, we can match a VSWR of  $\text{E}_r^2$ , where  $\text{E}_r$  is the dielectric constant of the plate. For fused-quartz the VSWR is about 15.

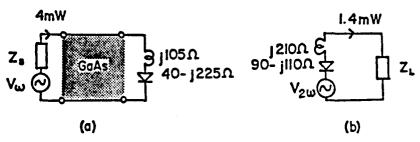


Fig. 5 (a) Input equivalent circuit at 65 GHz, (b) Output equivalent circuit at 130 GHz.

### Acknowledgments

We thank Dr. Peter Siegel and Dr. Anthony Kerr at the National Radio Astronomy Observatory for sending us their multiplier program. We appreciate the advice Dr. Chung-en Zah at Bell Communications Research on diode design, fabrication, and quasi-optical filters. This work was supported by the Army Research Office and by TRW under the University of California MICRO program. Wayne Lam is supported by an Army Research Office Fellowship.

### 6. References

- [1] G. Latmiral and A. Sposito, "Radar Corner Reflector For Linear or Circular Polarization," J. of Res. of NBS, 66D, pp. 23-29, 1962.
- [2] J. A. Arnaud and A. Pelow, "Resonant-Grid Quasi-Optical Diplexers," Bell Sys. Tech. J., 54, pp. 263-283, 1975.
- [3] R. Ulrich, T. J. Bridges, and M. A. Pollack, "Variable Metal Mesh Coupler for Far Infrared Lasers," Appl. Opt., 11, pp. 2511-2516, 1970.
- [4] P. P. Tong, D. P. Neikirk, D. Psaltis, K. Wagner, and P. E. Young, "Tracking Antenna Arrays for Near-Millimeter Waves," IEEE Trans. on Antennas and Propagat., AP-31, pp. 512-515, 1983.
- [5] G. G. MacFarlane, "Quasi-Stationary Field Theory and Its Application to Diaphragms and Junctions in Transmission Lines and Wave Guides," Proc. Inst. Blect. Eng., 93, Part 3A, pp. 1523-1527, 1946.
- [6] H. Siegel, A. R. Kerr, and W. Hwang, "Topics in the Optimization of Millimeter-Wave Mixers," NASA Technical Paper 2287, Mar. 1984.
- [7] J. W. Archer, "A Novel Quasi-Optical Frequency Multiplier Design for Millimetere and Submillimeter Wavelengths," IBBE Trans. Microwave Theory and Tech., MTT-32 pp.421-427, 1984.

# DESIGN OF A TILTED BEAM WAVEGUIDE PLANAR ARRAY

John M. Wachsman
Adams-Russell Company, Inc.
Microwave Products Division
Chatsworth, CA 91311

### ABSTRACT

The purpose of this paper is to discuss the general design of a standing wave planar array with the main beam tilted in the E-plane at  $\Theta_0$  off broadside. A brief discussion of beamtilt theory will precede the derivation of the design equations. This will be followed by the procedure used to achieve the proper slot dimensions from the desired excitations and design equations. Finally, a comparison between theoretical and measured patterns on a Ku band array will be shown.

### 2. INTRODUCTION

Waveguide arrays have been used to create radiation patterns of narrow beams, shaped beams, and tilted or scanned beams. The desired radiation pattern is dependent on amplitude and phase distribution across the aperture. Achieving the desired amplitude and phase distribution with radiating slots (longitudinal slots in

the broad wall) is common practice, however, the problem becomes more complex when a non-resonant distribution is to be determined by the feed slots (series-series slots), the second layer in a two dimensional array. This is because the loading on these slots is the radiating guides rather than free space. This paper will address a tilted beam but the theory is applicable to achieve any desired voltage amplitude and phase variation.

### BASIC BEAMTILT THEORY

Processor

the beststate beststate beststate attracted station

In order to tilt the mainbeam of an array, it is necessary to create a linear phase slope across the front of the array. The amount of phase slope is related to the amount of beam tilt. In general, the array will consist of elements with a desired amplitude distribution and a progressive phase shift between elements as depicted below.

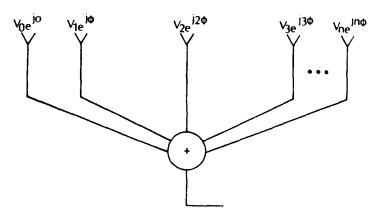


Figure 1. Linear Array

It can be shown that the direction of the mainbeam,  $\Theta_0$ , is related to the differential phase,  $\phi$ , between adjacent elements by

$$\Theta_0 = \sin^{-1}\left(-\frac{\phi}{\beta d}\right) \tag{1}$$

where  $\beta = 2\pi/\lambda_0$ 

 $\lambda_{O}$  = freespace wavelength

d = interelement spacing

### 4. DESIGN OF WAVEGUIDE ARRAY

To tilt the main beam in the E-plane of a waveguide array, drawn in Figure 2, it is necessary to create a differential phase, φ, between adjacent feed slots. Possible ways of doing this

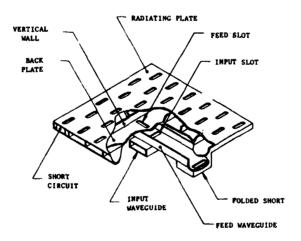
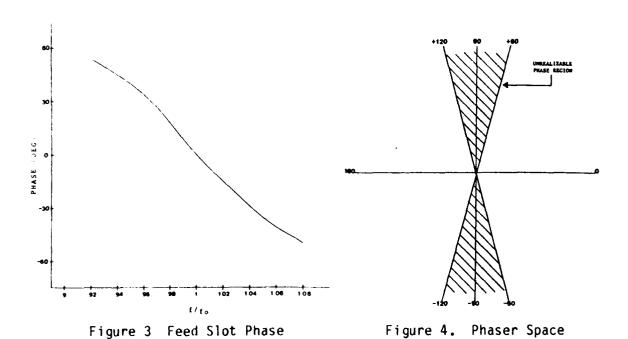


Figure 2. Two Dimensional Waveguide Array

are: (a) line lengths between feed slots other than  $\lambda g/2$ , (b) dielectric blocks between feed slots and (c) non-resonant feed slots. Solution (a) will create a non-uniform interelement spacing, and the overall design method is no longer valid. Solution (b) is generally not feasible because there is not enough room between the feed slots. Therefore, solution (c) is the most practical. The general limitations of using nonresonant slots is that empirical data reveals the maximum realizable phase shift is  $\approx \pm 60^{\circ}$  (see Figure 3). Therefore, there is an unrealizable zone in the phaser space as depicted in Figure 4.



vs Frequency

76

It is essential that any design using this approach does not have any slot phases between  $60^{\circ}$  and  $120^{\circ}$  or  $-60^{\circ}$  and  $-120^{\circ}$  as there is significant pattern degradation when unrealizable phases are used. Note that angles from  $+120^{\circ}$  to  $-120^{\circ}$  are achieved by changing the slot orientation thus creating an extra  $180^{\circ}$ , i.e.,  $-140^{\circ}$  is realized by designing a  $+40^{\circ}$  slot and changing its orientation in the feedguide as depicted in Figure 5.

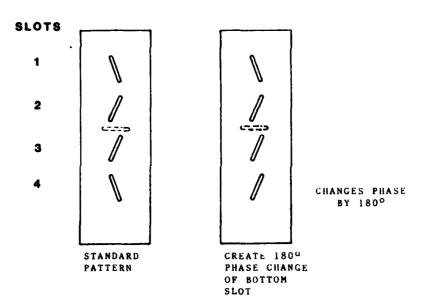


Figure 5. Creating a Phase Between +120° and -120°

POSSESSES PRODUCE CONTRACTOR OF TRANSPORT OF TRANSPORT OF THE PRODUCE OF TRANSPORT OF THE PRODUCE OF THE PRODUC

The design process requires determination of the angle and length of the feed slots. Therefore, an expression between desired voltage amplitude and phase and angle and length must be achieved. The voltage amplitude and phase of the feed slot is derived as a function of the slot coupling values m and  $\alpha$ .

The m and  $\alpha$  terms are related to resonant resistance and frequency which are empirically linked to angle and length. To accomplish this, the following circuit shown in Figure 6 is used.

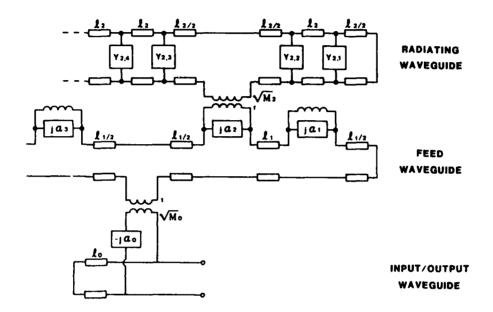


Figure 6. Waveguide Array Schematic

 $\lambda_q$  = guide wavelength

 $Y_{k,n}$  = admittance of the nth radiating slot in the kth row

 $m_k$  = coupling factor of the kth feed slot

 $\alpha_{k}$  = phase term associated with the kth feed slot

 $m_0$  = coupling factor of the input slot

 $\alpha_{0}$  = phase term associated with the input slot

For this derivation, the following assumptions are made.

- 1) The end radiating slots are  $\lambda_g/4$  from the short, the inner radiating slots are  $\lambda_g/4$  from the feed slot, and all adjacent radiating slots are  $\lambda_g/2$  apart.
- 2) All radiating slots are resonant.

- Industrial Afficient assessed between statements for the control of

3) The end feed slots are  $\lambda_g/2$  from the short the minor feed slots are  $\lambda_g/4$  from the input slot, and adjacent feed slots are  $\lambda_g/2$  apart.

With these assumptions, the circuit shown in Figure 7 can be used to determine the transformed input impedance of a radiating guide through the  $\mathbf{k}^{\text{th}}$  feed slot.

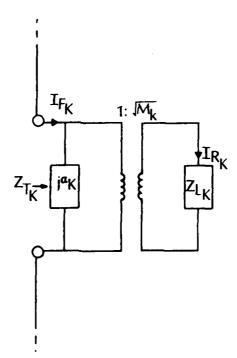


Figure 7. Single Feed Slot Loaded By Radiating Waveguide

where 
$$Z_{k} = \sum_{n=1}^{N} G_{k,n}$$
 (Y<sub>k,n</sub> = G<sub>k,n</sub> Assumption 2)

 $m_k$ ,  $\alpha_k$  = coupling terms of the  $k^{th}$  feed slot

 $I_{Fk}$  = feedguide current through  $k^{th}$  feed slot

 $I_{R_k}$  = radiating current through the  $k^{th}$  radiating guide

 $Z_{TK}$ = transformed impedance through the  $k_{(}^{th}$  feed slot

A desired  $V_k$  and  $\Theta_k$  is necessary to obtain the beamtilt. Therefore, a relationship between  $V_k$  and  $\Theta_k$  and  $m_k$  and  $\omega_k$  must be found. Hence the  $k^{th}$  feed slot will be investigated and the k subscript dropped.

Watson's series-series coupling  $law^1$  will be used.

$$\frac{1}{Z_{\mathsf{T}}} = \frac{\mathsf{m}}{\mathsf{Z}_{\mathsf{L}}} + \mathsf{j}\alpha \tag{2}$$

It can be shown that the ratio of the radiating current  $\mathbf{I}_{\mathsf{R}}$ , to feed guide current is

$$\frac{I_R}{I_F} = \frac{\sqrt{m}}{m + j\alpha Z_L}$$
 (3)

and

$$m = \frac{Z_L R_T}{|Z_T 2|}$$
 (4)

$$\alpha = \frac{-X_T}{|Z_T 2|} \tag{5}$$

where  $R_T$  = the real part of  $Z_T$   $X_T$  = the imaginary part of  $Z_T$ 

The desired voltage excitation, V, is given by

$$V = I_R Z_L \tag{6}$$

substituting (2) into (5) yields

$$V = \frac{\sqrt{m}(m - j\alpha Z_L)}{m^2 + \alpha^2 Z_L^2} I_F Z_L$$
 (7)

Therefore, the phase of V,  $\phi_V$  is

$$\phi_{V} = \tan^{-1}\left(\frac{-\alpha Z_{L}}{m}\right) \tag{8}$$

and the magnitude of V is

$$|V| = \frac{m}{\sqrt{m^2 + \alpha^2 \overline{Z}_L^2}} |I_F| |Z_L|$$
 (9)

substituting (4), (5) into (8) yields

$$|V| = \sqrt{Z_L R_T} |I_F| \tag{10}$$

In general,  $|I_F|$ , can be written

$$|I_{F}| = \frac{V_{o}}{|\sum_{i=1}^{K} (R_{T_{i}} + jX_{T_{i}})|}$$
(11)

where

$$|\sum_{i=1}^{K} (R_{T_i} + jX_{T_i})|$$
 = magnitude of the total transformed impedance on one side of the input slot.

 $V_0$  = voltage impressed on the feedguide from the input slot

Figure 8 illustrates the circuit used to determine the feedguide current.

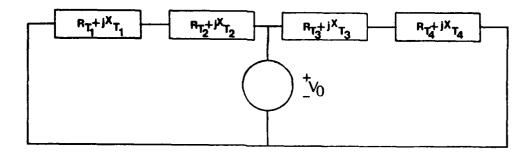


Figure 8. Impressed Input Voltage on Feedguide

Therefore, from (4)(5) and (8)

$$\phi_{V} = \tan^{-1}\left(\frac{-\alpha Z_{L}}{m}\right) = \tan^{-1}\left(\frac{-X_{T}}{R_{T}}\right)$$
 (12)

$$|V| = \frac{\sqrt{R_T Z_L} V_o}{|V|}$$

$$|V| = \frac{K}{K} (R_{T_i} + jX_{T_i})|$$

$$|V| = \frac{K}{K} (R_{T_i} + jX_{T_i})|$$

$$|V| = \frac{K}{K} (R_{T_i} + jX_{T_i})|$$

So, in general, for given  $Z_{L_K}$ , one has 2K equations and 2K unknowns with K being the number of feed slots on one side of the input. A computer program was written to solve these equations for  $X_T$  and  $R_T$ . These terms yield an m and  $\alpha$  according to (4)

and (5). This program computes the resonant resistances, Ro's, and the normalized frequencies  $f/_{f0}$ 's for the computed m's and  $\alpha$ 's. The Ro's and  $f/f_0$ 's can then be correlated to the physical dimensions of the slot as shown in Figure 9.

It is important to note that the feedguide current,  $I_{\rm F}$ , has a phase associated with it, (see Equation 10.) This current phase will not, in general, be the same above and below the input slot. Therefore, a phase correction using the input slot location will be necessary. Also, if the array is subdivided into subapertures (modules), the phase from module to module may have to be corrected so that there is a continuous phase slope across the face of the array.

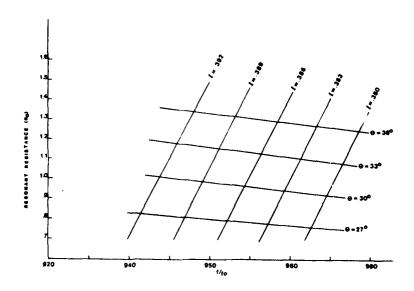


Figure 9. Resonant Resistance for +45° Phase

### 5. EXPERIMENTAL RESULTS

A 10 module linear 2.5% bandwidth Ku-band array, shown in Figure 10, was designed and fabricated. Each module has 4 feed slots with 6 radiating slots in each row. The phase shift between adjacent slots was chosen to be 90° which relates to a beam tilt of 22° off of boresight.

The desired voltage phases were chosen to be  $+45^{\circ}$ ,  $-45^{\circ}$ ,  $-135^{\circ}$ ,  $+135^{\circ}$  for each module. This made the modules similar and the phases remained continuous from module to module. A 31dB n=5 linear Taylor distribution was utilized in the design.

A comparison between the computed and the measured patterns is shown in Figure 11. The computed pattern contains the measured parameters of the corporate feed.

Roth the computed and measured patterns show an error lobe appearing at the image angle of the array. This is due to a two-slot periodic amplitude error that occurs off center frequency. At the high (low) frequency the +45°  $R_0$  increases (decreases) while the -45°  $R_0$  decreases (increases). The error lobe at center frequency appears because the shorts in the radiating guide were not  $\lambda/4$  from the end slot. The shorts were moved in .010 to simulate a .020 wall between modules. A grading lobe appeared at 0° due to higher order mode coupling and was compensated for in this experiment.

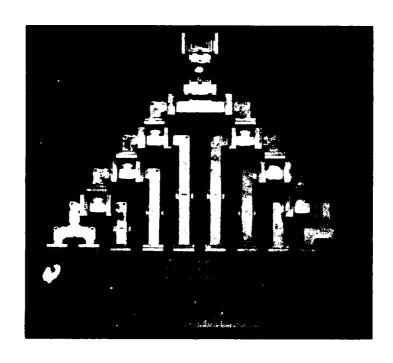


Figure 10. 10 Module Array

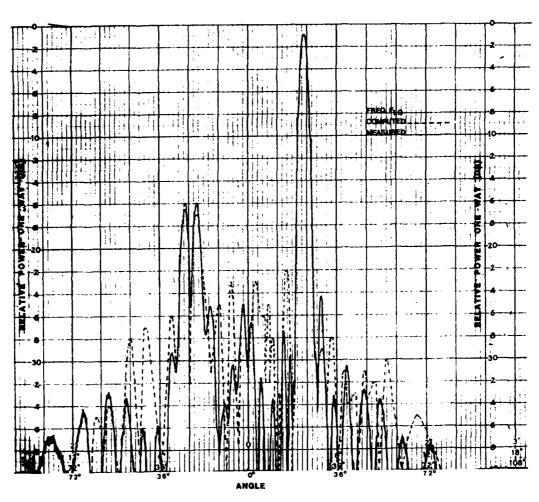


Figure 11(a). E-plane Low Frequency

STATES OF THE PROPERTY OF THE PARTY OF THE P

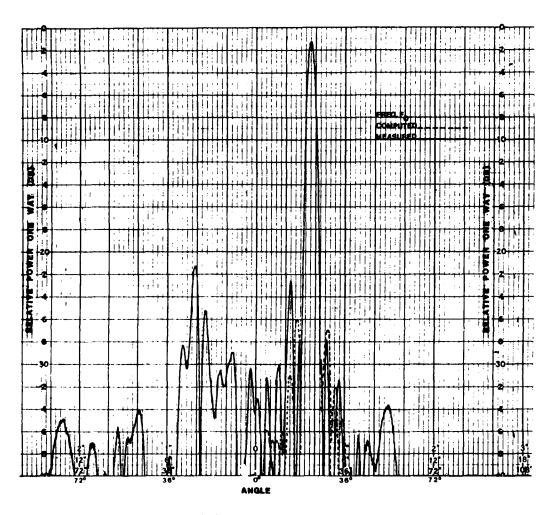
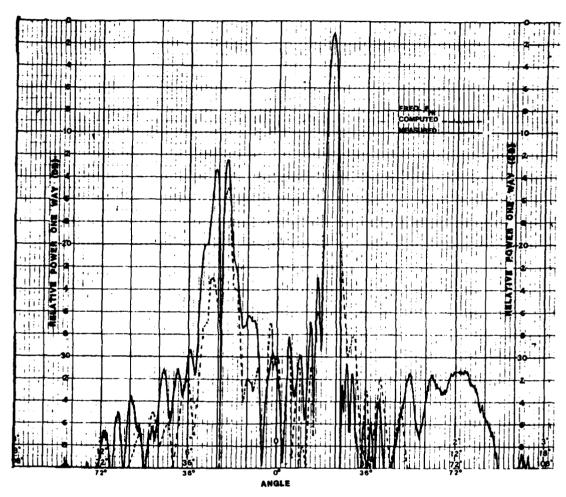


Figure 11(b). E-plane Center Frequency



cigure 11(c). E-plane High Frequency

AND PROCESS STREET, SCHOOL STREET

### 6. SUMMARY

It has been shown that it is possible to achieve a tilted beam in the E-plane using non-resonant feed slots. The critical parameters are the inclination and length of the feed slots. A designer must ensure that the desired phase of any element is within the realizable region of a non-resonant feed slot. Corrections must be made in both input slot location and corporate feed phase in order to obtain a linear phase slope across the front of the array.

### **ACKNOWLEDGEMENT**

The author would like to acknowledge the guidance and insights of Joseph Thomas and thank Bill Bullen and Hal Banbrook for their attention to detail in the hardware development.

### REFERENCES

SAL BESSER SECTION REPRESE BONNESS BREESE

1. Watson, W.H., (1946) Resonant Slots, J. Inst. Elect.
Engers (IIIA), 747-777

AD-A166 754 PROCEEDINGS OF THE 1985 ANTENNA APPLICATIONS SYMPOSIUM VOLUME 1(U) ROME AIR DEVELOPMENT CENTER GRIFFISS AFB NY DEC 85 RADC-TR-85-242-VOL-1 2/4 UNCLASSIFIED F/G 9/5 NL 3



MICROCOPY TELECLOTION TEST CHART
NATIONAL BUREAU OF STANDARDS - 1963 - A

### RESONANT MICROSTRIP DIPOLE ARRAYS

Jeffrey Lane, Norbert Sa, and John Toth Raytheon Company, Missile Systems Division Bedford, Massachusetts 01730

### ABSTRACT

In the 1984 Antenna Applications Symposium, a paper presented by W. Miccioli discussed the development of a microstrip radiating aperture utilizing Electromagnetically Coupled (EMC) microstrip dipole radiators fed by a resonant feed configuration. This paper describes the continuation of that effort, and several new features are discussed. A rigorous analytical model of the dipole radiating element above a grounded dielectric slab has been developed. Theoretical and measured radiation pattern characteristics are presented which indicate the excellent validity of the model. In addition, a technique for obtaining broadband array performance will be reviewed and measured data will be presented illustrating the 10% bandwidth achieved.

### 1.0 INTRODUCTION

The basic microstrip antenna configuration of interest first presented by W. Miccioli consists of several resonant linear arrays of half wavelength dipoles, as shown in Figure 1, used in conjunction with a power division network to develop each quadrant of a microstrip monopulse array. The first dipole in Figure 1 is located at the voltage maximum that occurs one half dielectric wavelength from the open circuit end of feed. Successive dipoles may be located at

wavelength intervals to obtain broadside radiation. Broadside radiation can also be obtained by positioning the dipoles at half wavelength intervals with alternate dipoles on opposite sides of the imbedded feed line.

W. Miccioli also discussed the idea of "stacking" dipoles to achieve added bandwidth. Figure 2 shows a cross-sectional view of this stacked configuration. Radiation efficiency and bandwidth of the microstrip antenna increase with dipole height above the ground plane. Because of this, the upper dipole is positioned at roughly five times the height of the feed line. The lower dipole is kept relatively close to the feed to maximize coupling.

Recently, a nonstacked microstrip dipole electromagnetically coupled to a parallel feed was analyzed  $^2$ . The method of potentials was used to calculate the Green's function pertaining to current flow in only one direction. Since in the configuration considered herein there is current flow in two directions (dipole and feed), the Green's function for sources in both directions is required. Therefore, the dyadic Green's function technique which gives the Green's function  $(\overline{\overline{G}})$  for an arbitrarily directed source has been used in this paper.

### 2.0 DIPOLE ANALYTIC MODEL

cool accessed from the second seconds assessed assessed assessed

An arbitrarily directed current source placed above an infinite grounded dielectric slab is shown in Figure 3. Equations 1 and 2 are the wave equations that govern the fields above and inside the dielectric. Solving for these fields is facilitated by letting the

source term become the delta function or unit source where the Green's function is, by definition, the electric field due to a unit source (Equations 3 and 4).

Applying the Dirichlet and Neumann conditions to tangential  $\overline{E}$  and  $\overline{H}$  at the interface and setting tangential  $\overline{E}$  to zero at the conductor, a solution for  $\overline{\overline{G}}$  is obtained (Figure 4). The total electric field in regions 1 or 2 is derived by integrating  $\overline{\overline{G}}$  over the dipole current distribution (Equation 5). For the purpose of obtaining far field equation, the asymptotic form of the Green's function is derived by applying the saddle point integration technique. Since the far field is stationary about the antenna current distribution, the Green's function is multiplied by the Fourier transform of an assumed current. The resulting normalized electric field is given by Equation 6.

In Equation 6, the first two terms are the Fourier transforms of the uniform current distribution along the width and half sinusoidal current distribution along the length of the dipole, respectively. In the third term  $a(\theta)$  and  $b(\theta)$  are determined by the boundary conditions of the particular geometry. Sin $\phi$  multiplying the  $\phi$  component and  $\cos\phi$  multiplying the  $\theta$  component are due to the current chosen to be x-directed.  $K_1$  and  $K_2$  are the propagation constants for regions 1 and 2, respectively.

ASSESSMENT OF THE PROPERTY OF

It is interesting to note that if you let the dielectric constant of region 2 equal that of air, then  $K_1 = K_2$ ,  $a(\theta) = -1$ ,  $b(\theta) = 1$ , and Equation 6 reduces to the well known expression for a horizontal current source above an infinite ground plane.

### 3.0 ANALYTIC MODEL VALIDATION

A single element microstrip dipole was fabricated to compare measured and numerical results. The lower board, which contains the feed line, is .015 inch Duroid and the upper board is .031 inch Duroid. Both layers have a dielectric constant of 2.2.

Measured return loss in dB vs normalized frequency for this dipole is shown in Figure 5. It has a -10 dB bandwidth of 3.2 percent, which is typical for single layer microstrip dipoles. A polar plot of the H-plane radiation pattern of the antenna is shown in Figure 6. Agreement between the measured and predicted results is excellent. The asymmetry in the measured pattern from 60 to 90 degrees is due to reflections in the anechoic chamber. Figure 7 is a polar plot of the measured and calculated E-plane radiation pattern. Again, there is excellent agreement between the two curves. Ripples in the E-plane pattern are due to scattering off the edges of the ground plane.

A five-element resonant dipole array was constructed to examine dipole performance in a linear array configuration. The dipoles are positioned over voltage maxima of the feed line approximately one wavelength apart, as shown in Figure 8, so that broadside radiation is obtained. Figure 8 shows a plot of the measured vs calculated H-plane pattern for a five-element resonant dipole array.

The calculated plot shows good agreement with the measured plot data from broadside to 60 degrees, and even at large scan angles the calculated plot provides an average of the asymmetrical sidelobes.

Mutual coupling between dipoles was not taken into account in the calculations, but the measured data suggests that their effects are small.

### 4.0 MICROSTRIP ARRAY BANDWIDTH

ALTERNATION RECESSED BY THE SECOND BY THE SECOND SE

The ultimate application of the EMC dipole radiator is the development of a complete moderate bandwidth (≥10%) planar microstrip array aperture. An overlay of the microstrip aperture artwork is shown in Figure 9. To obtain a monopulse configuration, the full array is divided into quadrants. Each quadrant, which is independently fed by its own power divider network, is made up of two and three element linear sub-arrays.

Initial array development concentrated on a single layer of EMC dipoles over the microstrip power divider feed, resulting in structures constrained to a few percent bandwidth. The addition of a second layer of dipoles separated in height and aligned with the first set could improve the array bandwidth characteristics. It was discovered that the bandwidth of the linear array structure increased as the height of the upper dipole in Figure 2 was increased. The lower dipole must remain relatively close to the feed line in order to obtain a satisfactory impedance match for a given dipolefeed overlap. Radiation by the feed itself is minimized by placing it near the ground plane.

During the present investigation, optimization of the double stacked dipole bandwidth was addressed experimentally. Various combinations of dipole to feed and dipole to dipole separation were tested. A plot of the best return loss data for a three-element linear arry is shown in Figure 10. As indicated, a 10% 2:1 VSWR bandwidth (-10dB return loss) was achieved. Similar results were obtained for the required two-element linear array. A plot of the measured and theoretical H-plane pattern for the three-element linear array is shown in Figure 11. The sidelobe level of the measured pattern is within .5dB of the theoretical pattern.

# 5.0 CONCLUSIONS

The analytical tools used in the past did not adequately model the element pattern of the EMC microstrip dipole. Previous models deviated from the actual measured data at large angles (between 60° and 90°) from broadside. The predicted results presented here show a very close correlation to measured results for the single element. This improvement in the single element model leads to corresponding improvements in multi-element array analytical results. The closed form far field element pattern expression developed should provide a convenient means for more accurate prediction of large arrays.

The bandwidth of low profile microstrip radiators has always presented problems, both from an individual radiator consideration and also when considering the phase dispersive effects in resonant arrays. These latter effects will always be present when resonant arrays become large and must be handled by the overall feed design of

the array in question. Maximizing the bandwidth of individual radiators will aid in reducing the magnitude of the overall problem. The results obtained for multielement linear arrays indicate that the bandwidth can be increased from about three to ten percent. This greatly increases the applicability of this type of radiator.

# 6.0 REFERENCES

THE PROFITS COURTS PROFISE CONTROL

- William Miccioli, John Toth, Norbert Sa, and Michael Lewis,
   "Microstrip Monopulse Dipole Array," 1984 Symposium on Antenna
   Applications, Urbana, Illinois, September 19-21, 1984.
- Pisti B. Katehi and Nicolaos G. Alexopoulos, "On the Modeling of Electromagnetically Coupled Microstrip Antennas--The Printed Strip Dipole," <u>IEEE Transactions on Antennas and Propagation</u>, Vol. AP-32, No. 11, November 1984.

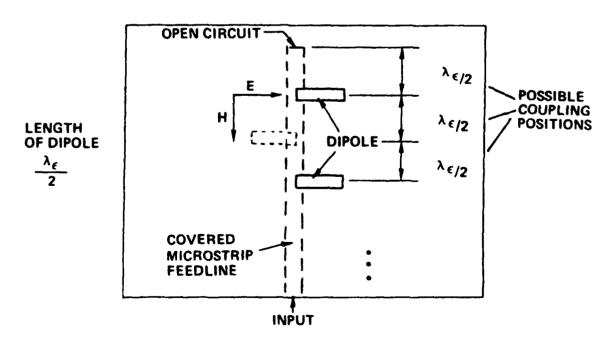


Figure 1. EMC Linear Array, Top View

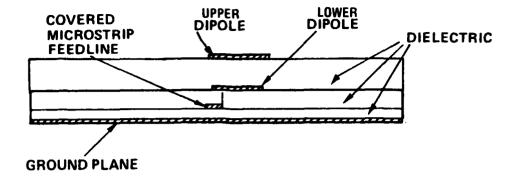


Figure 2. EMC Linear Array, Cross-Sectional View

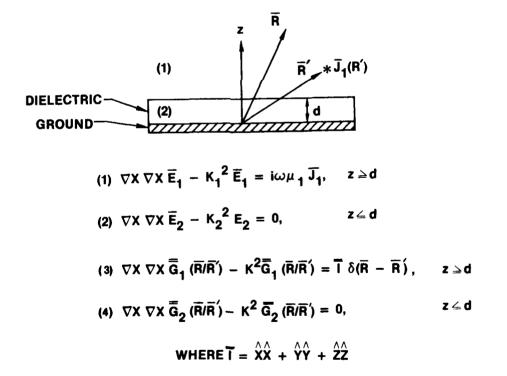
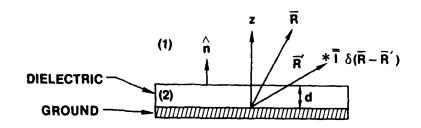


Figure 3. Vector Wave Equations



BOUNDARY CONDITIONS: 
$$\hat{n} \times \overline{G}_1 = \hat{n} \times \overline{G}_2$$
,  $z = d$  DIRICHLET 
$$\hat{n} \times \nabla \times \overline{G}_1 = \hat{n} \times \nabla \times \overline{G}_2, \qquad z = d$$
 NEUMANN 
$$\hat{n} \times \overline{G}_2 = 0, \qquad z = o$$

$$^{(5)} \ \widetilde{\mathbf{E}}_{1}(\mathbf{R}) = \mathbf{k}\omega\mu_{0} \iiint \ \widetilde{\mathbf{G}}_{1} \left(\overline{\mathbf{R}}/\overline{\mathbf{R}}'\right) \cdot \widetilde{\mathbf{J}}_{1} \left(\overline{\mathbf{R}}'\right) \mathrm{d}\mathbf{r}'$$

Figure 4. Boundary Value Problem

(6) 
$$F(\theta, \phi) = \frac{\sin\left[\left(\frac{KW}{2}\right) \sin\phi \sin\theta\right]}{\left(\frac{KW}{2}\right) \sin\phi \sin\theta} \cdot \frac{\cos\left[\frac{\pi}{2} \sin\theta \cos\phi\right]}{1 - \sin^2\theta \cos^2\phi}$$

$$\left\{\hat{\phi} \left[-\mathbf{a}(\theta)\mathbf{e}^{\mathsf{i}\mathsf{K}}_{\mathsf{1}}\mathbf{\cos}\theta\,\underline{\mathbf{d}}\,\underline{\mathbf{e}}^{\mathsf{-}}\,\mathsf{i}\mathsf{K}_{\mathsf{1}}\mathbf{\cos}\hat{\theta}\,\mathbf{d}\right]\,\,\sin\phi\,-\hat{\theta}\left[\mathbf{b}(\theta)\mathbf{e}^{\mathsf{i}\mathsf{K}}_{\mathsf{1}}\mathbf{\cos}\theta\,\mathbf{d}\,\underline{\mathbf{-}}_{\mathsf{e}}^{\mathsf{i}\mathsf{K}}_{\mathsf{1}}\mathbf{\cos}\theta\,\mathbf{d}\right]\,\cos\phi\,\cos\theta\right\}$$

WHERE 
$$a(\theta) = -e^{-2idB} \left\{ \frac{A \cos(Ad) + iB \sin(Ad)}{A \cos(Ad) - iB \sin(Ad)} \right\}$$

$$b(\theta) = e^{-2idB} \left\{ \frac{K_2^2 B \cos(Ad) + iA K_1^2 \sin(Ad)}{K_2^2 B \cos(Ad) - iA K_1^2 \sin(Ad)} \right\}$$

$$A = \sqrt{K_2^2 - K_1^2 \sin \theta} \quad B = K_1 \cos \theta$$

$$K_1 = \omega \sqrt{\mu_0 \epsilon_0} \quad K_2 = \omega \sqrt{\mu_0 \epsilon_r \epsilon_0}$$

Figure 4 (continued). Normalized Electric Field

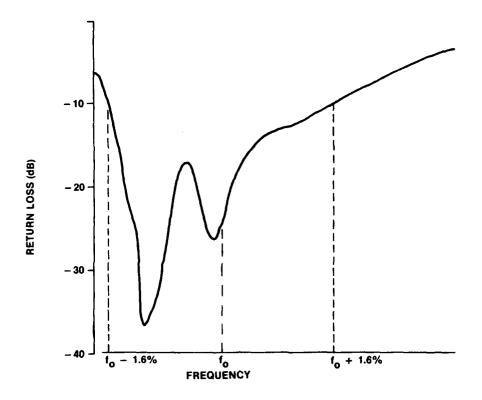


Figure 5. Input Impedance Match of Single Element Dipole

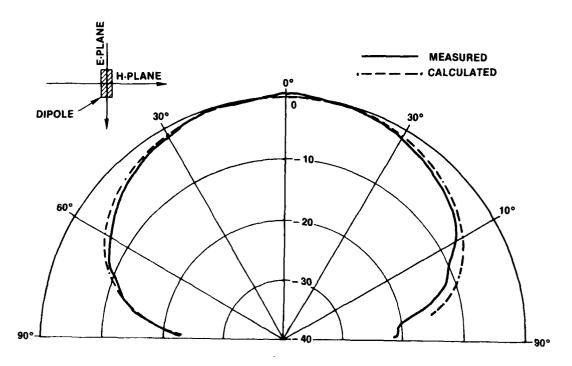


Figure 6. H-Plane Radiation Pattern of Printed Dipole 100

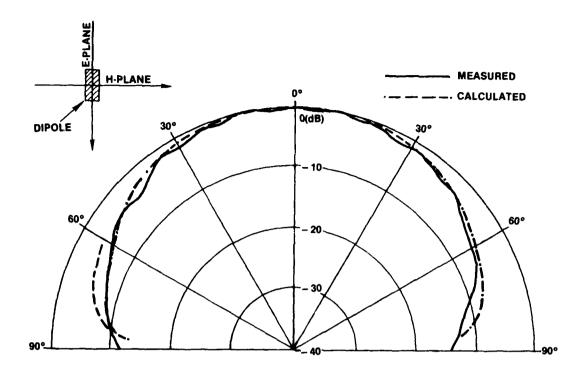


Figure 7. E-Plane Radiation Pattern of Printed Dipole

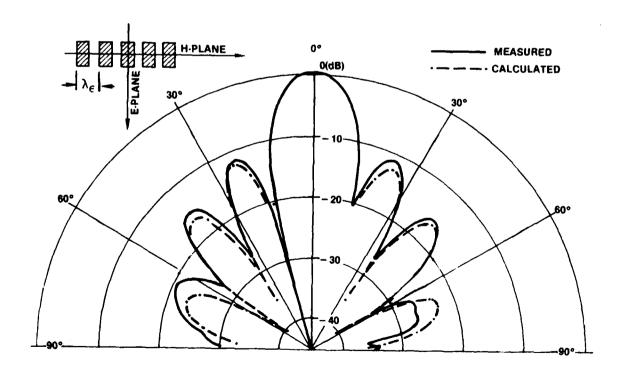


Figure 8. H-Plane Radiation Pattern of 5 Element Linear Array

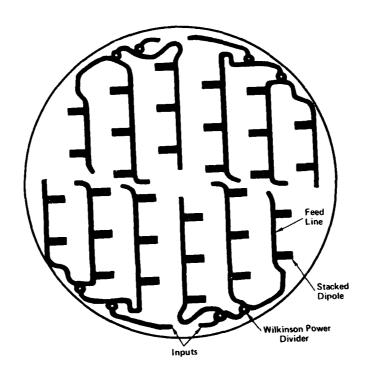


Figure 9. Microstrip Monopulse Dipole Array

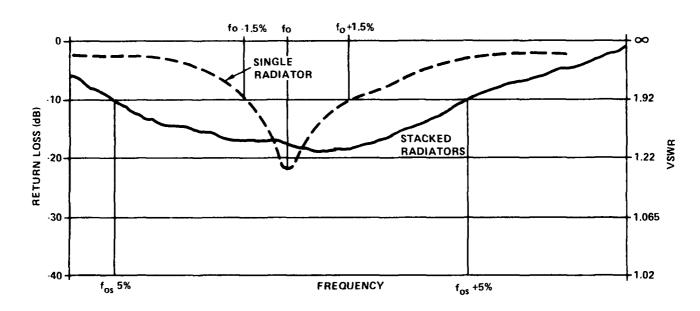


Figure 10. Input Impedance Match of Three Element Arrays

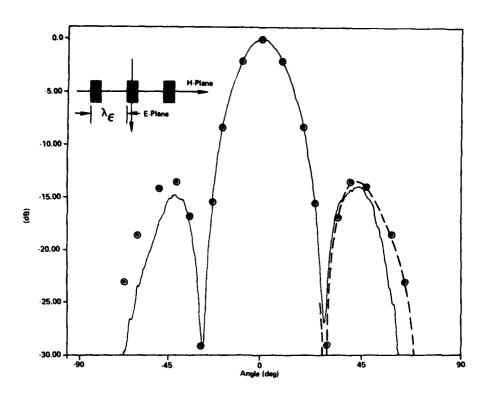


Figure 11. Three Element Stacked Dipole Array H-Plane Radiation Pattern

COCCU STREET KNOWNS SEEDING

## SOME BROADBAND, LOW-PROFILE ANTENNAS

P. Mayes, D. Tanner, R. Waller, J. Drewniak,
T. Szmurlo, A. Boris, and D. Kunkee
Electromagnetics Laboratory
Department of Electrical and Computer Engineering
University of Illinois
Urbana, Illinois

### **ABSTRACT**

Several methods are presented for obtaining broadband performance from low-profile structures. radiating Computer-aided design can produce reactive matching networks that the theoretical impedance bandwidth of center-fed increase cavity-backed slot (CBS) antennas from a few percent to 30% or Attempts to achieve these results in practice fall more. somewhat short due to differences between the physical network and the theoretical model. Putting several CBS elements, even though high-Q, into a log-periodic array with a sufficiently high value of scaling factor can produce wideband performance in both impedance and patterns. A logarithmic spiral arm over a closely spaced conducting surface (operating as a radiating line) also displays wideband impedance. Single beam, circularly polarized patterns are obtained with this log-spiral transmission line antenna. A log-periodic zigzag slot in a wedge-shaped conducting surface produces linearly polarized radiation that is unidirectional when absorber is placed inside the wedge.

#### 1. INTRODUCTION

Property and the second of the

Some systems require, others are simplified by, the use of radiating elements that do not protrude beyond a prescribed structural surface. Available space and/or economics may also constrain the radiators from extending much below the surface. Such low-profile radiating elements generally take the form of either microstrip patches on a thin substrate or cavity-backed slots with very thin cavities. In either case, it is found that a single element displays a very narrow bandwidth due to resonant Nevertheless, these low-profile elements, especially behavior. the patch radiators, have found widespread application due to their simplicity, ease of construction, and light weight. Because of the ever-increasing demand for greater system bandwidth, it is highly desirable to develop radiators that overcome the bandwidth limitations typical of these high-Q yet retain the advantages of low-profile resonators. and construction. Several promising approaches increased bandwidth from low-profile radiators are presented here.

The impedance bandwidth of any lossy resonant device can be increased by adding a reactive network at its terminals. A method of designing such a network for a cavity-backed slot (CBS) shows theoretical promise, but practical difficulties. However, using multiple CBS elements, even high-Q ones, in a log-periodic array can produce near-constant impedance over a much wider

bandwidth than for an individual CBS element. Of course, increased directivity and gain that change little with frequency are also obtained with the LPCBS array.

Equiangular spirals in free space are well known to have theoretically unlimited impedance and pattern bandwidths<sup>1</sup>. However, cavity-backed spirals do not retain the free-space characteristics. Achieving even wideband performance from cavity-backed spirals usually entails putting microwave absorber in the cavity and accepting the resulting loss in gain. It is shown here that a single equiangular spiral arm backed by a closely spaced conducting surface displays a very wide impedance bandwidth that is indicative of non-resonant performance.

Non-resonant behavior can also bе expected from transmission medium with periodic or log-periodic undulations that produce fast-wave terms in the space spectrum of the near field. Examples are the log-periodic zigzag (LPZZ) wire or strip antennas<sup>2</sup>. An electromagnetic dual of the LPZZ constructed by using a slot line in a large ground plane. Broadband impedance is observed regardless of the angle between the two halves of the LPZZ slot antenna. However, since unidirectional radiation does not result for small included angles of the wedge-shaped ground surface, best patterns have been obtained when microwave absorber is placed in the interior of the wedge.

### 2. BROADBAND IMPEDANCE-MATCHING NETWORKS FOR CBS ELEMENTS

Construction and testing of external matching networks for cavity-backed slots are greatly simplified by using microstrip feeder to excite the slot. A typical two-port CBS antenna is shown in Figure 1. Although the cavity shown there is relatively deep (0.675-in), similar results can be obtained with shallower ones. Using the two-port feed allows one to evaluate the element for use in a series-fed array. The feed can be readily converted to one-port by shorting the microstrip to the ground plane on the side of the slot opposite the generator. Feeding the slot directly in the center presents a worst-case condition with respect to matching to 50-ohms since the slot impedance at resonance is very much higher (425 ohms). Center feed guarantees symmetry of the radiation patterns about the vertical plane through the center.

Contract of the State of the St

The design of a broadband matching network follows the theory of bandpass filters except for the difference in level of the input and output resistances. In the vicinity of the first resonance, the slot impedance varies as that of a shunt resonant circuit. The matching network for such a load involves coupled quarter-wave sections of line<sup>3</sup>. If the input and output resistances were equal, the coupled sections would be symmetrical; data for the design of such sections in microstrip are available in the literature. However, since the resistances are not equal, the required coupled sections are asymmetrical.

An extensive search of the literature failed to produce design equations for asymmetrical coupled sections in microstrip. However, the shunt resonance can be changed into a series resonance by using a uniform section of line that is approximately one-quarter wavelength long at the resonant frequency of the slot. This section can also be used to substantially lower the resistance that must be matched to 50 ohms. The matching network for a series resonant load involves only shorted stubs and it is thus easy to realize in microstrip. The form of the matching network for four resonators (N=4) is shown in Figure 2b where  $\mathbf{Z}_{\mathbf{A}}$  represents the impedance of the slot after transformation through the quarter-wave section.

If the CBS impedance locus conformed exactly to a series resonant circuit, design equations in the literature would yield a good result. However, the deviations from the ideal impedance will cause less than optimal performance from the network so designed. Hence, only the form of the matching network was taken from the published design procedure and the actual element values were determined by using a computer to minimize the magnitude of  $S_{11}$  over the desired operating band. Figure 3 shows the behavior of three different matching networks. Case A simply uses two quarter-wave transformers in cascade to bring the resistance level close to 50 ohms at the resonant frequency (1.1 GHz) of the slot. The limited bandwidth obtained in this way is obvious and it is presented primarily for comparison purposes.

Cases B and C show the results obtained from a network with N=3 designed to operate over a 30% bandwidth. These two cases differ in that a weighting factor was applied in Case C to emphasize the error in the desired value of  $S_{11}$  at resonance. This was needed to equalize the minima for the case N=3.

The theoretical performance of the matching network displays significant increase in the impedance bandwidth of a single CBS antenna. However, any practical realization of this network will deviate somewhat from the theoretical representation due to errors in construction and modeling. Figure 4 shows measurements made on three different matching networks designed according to the foregoing procedure with no trimming to attempt to achieve the theoretical performance. Note that the frequency of best This indicates that the theoretical stub match is shifted. lengths were not achieved. Note also that the match deteriorates progressively away from resonance, not displaying the multiple minima for  $S_{11}$  that are characteristic of the theoretical performance of the designed network. This indicates that the network will require more precise modeling to accomplish the theoretical performance.

### 3. A LOG-PERIODIC ARRAY OF CAVITY-BACKED SLOTS

evel legislated statement legislate, (colorate) program.

The success of log-periodic dipole arrays indicates that it is possible to combine several resonant elements in a structure that has wideband impedance and patterns<sup>4,5</sup>. However, the higher the Q of each element, the higher the value the scale

factor τ must be to achieve a given level of frequency independent performance. It is therefore expected that an array of CBS elements with very shallow cavities will require a rather high value of  $\tau$  (close to unity). Furthermore, since it would be inconvenient to scale the cavity depth from element to element, it may be necessary to modify the value of  $\tau$  along the structure in order to compensate for the changing Q of the Figure 5 shows a top view of a modified LPCBS array elements. having only four elements. The value of  $\tau$  is taken equal to 0.94 for the first two elements and equal to 0.92 for the remainder. This antenna was constructed from double-clad Rexolite 2200 (relative permittivity of 2.6) substrate 0.125-in thick. The walls of the cavities were formed by placing screws at 0.5-in intervals around the largest cavity and at correspondingly smaller spacings for the other cavities.

The MLPCBS antenna of Figure 5 was excited by a meandering microstrip like that shown in Figure 6. The excess line between adjacent cavities is required to produce backfire phasing of the active region. Figure 7 shows azimuthal radiation patterns illustrating that a backfire beam is indeed obtained over a bandwidth that is consistent with the small number of elements on this antenna. Although the front-to-back ratio remains almost constant from below 1 GHz to above 1.1 GHz, the particular parameters of this antenna may not represent those that produce the best obtainable value. Figure 8 shows the S<sub>11</sub> measured for

an MLPCBS antenna illustrating reasonable impedance performance over the aforementioned band. Values of  $S_{11}$  below 1 GHz are affected by the matched load placed on the end of the feeder. This is illustrated by the measured values of  $S_{21}$  shown in Figure 9.

# 4. LOG-SPIRAL TRANSMISSION LINE ANTENNAS

To achieve more nearly frequency-independent performance from cavity-backed spirals, a fundamentally different mode of operation has been studied. Rather than exciting one spiral arm against another as is customarily done, one or more spiral arms have been excited against a closely spaced conducting surface. Figure 10 shows the outline of a slot cut in a conducting plane using two equiangular spirals to form the edges of the slot. Near the small end of this structure a single arm of a spiral conductor can be excited as the continuation of a TEM mode transmission line. Figure 11 shows the details of feeding the spiral arm against a closely spaced conducting plane using a coaxial cable. The spiral arm can be a considered to be a strip transmission line that has curvature and expanding width. measurements confirmed that this line is capable of radiating enough energy so that its termination at sufficient distance from the feedpoint does not affect the impedance observed at the feedpoint. This elimination of the large-end truncation effect is, of course, essential in achieving frequency-independent performance from a structure with finite size. Elimination of

the truncation effect was also established by measuring S<sub>11</sub> over an extended frequency band and the results are shown in Figure 12. Although some truncation effect is apparent near 1 GHz, the locus quickly converges to a rather compact region at higher frequencies. However, there is a pronounced tendency for the center of the impedance locus to move down the real axis as the frequency is increased. Near-field measurements were made by inserting a small probe through the conducting surface behind the spiral arm. Although these measurements confirmed that the field was small at the large end of the spiral at the higher frequencies, the variation with distance from the feedpoint was not the simple exponential that had been observed and computed earlier for two-arm, balanced spirals in free space.

Modifications of the antenna were made to conform more closely to the theoretically ideal self-scaling structure. First, the spiral arm was pulled away from the conducting backplane at the large end, thus making the spiral coincide more closely to a conical surface. Near-field measurements on this structure do display an exponential law for decay. They also indicate that the field along one edge of the spiral arm is much larger than that along the other edge and that the wave along the edge with the larger field has phase velocity that is greater than the intrinsic value for free space. The measured values of S11, although compact over relatively wide bands, again display a path which wanders over the Smith Chart as shown in Figure 13.

special reference references between specials and specials.

Recent modifications in the antenna have included using a planar spiral arm backed by a closely spaced conical conducting surface. Attention to the details of the feedpoint region is very important in the achievement of a tight impedance locus over a very wide band. Figure 14 shows the results that have been obtained using a 0.085-in diameter coaxial cable to feed a log-spiral transmission line antenna that starts with zero curvature at the feedpoint. In this case, the transition to log-spiral geometry takes place rather quickly, about 1-in from the feedpoint. Antennas with less abrupt transitions are under investigation.

The one-arm spiral antenna produces a single beam. The pattern is nearly circularly polarized over most of the beam. Figures 15-17 show patterns measured with a spinning dipole to illustrate the polarization as a function of elevation angle. Four cuts at different azimuth angles are shown for each frequency. Asymmetries present in these patterns are believed to be associated with the rather slow rate of spiral used in this antenna (a=0.2). Work is also currently underway to test spirals with tighter wrap.

## 5. A LOG-PERIODIC ZIGZAG SLOT ANTENNA

CAMPARTON SONOTON SONOTON SONOTON SONOTON SONOTON SONOTON

Log-periodic zigzag wires and strips have long been known to produce frequency-independent performance<sup>2</sup>. A typical LPZZ strip antenna is shown in Figure 18. The parameters of this antenna are the angle  $\alpha$  which defines the extremities of the conductors,

the angle  $\beta$  which defines the width of the strip, and the angle  $\gamma$ between the planes of the conductors. The conversion of this geometry to a zigzag slot is illustrated in Figure Excitation across the gap at the small end produces a traveling wave along the slot in a manner similar to the traveling wave that is excited by placing a generator between the tips of the strips in Figure 18. Figure 20 shows measured values of S, for an LPZZ slot antenna with the parameters given in Figure 19. Once again, the compact locus indicates the absence of large-end truncation effects. Unlike that of the LPZZ strip, however, the median value of impedance, approximately 80 ohms, is influenced by the angle between the two sides of the wedge-shaped conducting surface. This is due to the basic difference in field configuration for the slot antenna in that the electric field is developed between the edges of the slot, and not between the two sides of the wedge.

The aforementioned differences in fields between the LPZZ strip and slot antennas also cause differences in pattern performance. Whereas unidirectional patterns are obtained from LPZZ strip antennas with small wedge angles, such is not the case with the LPZZ slot. The unidirectional patterns shown in Figure 21 were obtained by placing absorber within the wedge.

#### CONCLUSIONS

THE RESERVE RESIDENCE OF THE PROPERTY OF THE P

Several techniques that show promise for producing very broadband impedance and pattern performance from low-profile

antennas have been presented. Although the use of external impedance-matching networks has been shown to be theoretically capable of increasing impedance bandwidths of high-Q elements from only a few percent up to 30 percent or more, the practical realization of increases this large will be dependent upon reducing the differences between the physical networks and the theoretical models thereof. The technique would be useful in reducing the Q of narrow-band elements that might be used as elements in a log-periodic array. Although it has been shown that log-periodic arrays of high-Q elements can be made to operate in a frequency-independent manner if the value of scaling factor  $\tau$  is taken to be sufficiently large, reduction in the Q of the elements would permit a similar reduction in  $\tau$  without loss in performance. Greater bandwidth could then be covered by an antenna having the same physical size as another but a lower value of  $\tau$ .

A new mode of operation of logarithmic spirals, involving excitation against a closely spaced conducting surface, produces negligible large-end truncation effect. Exponential decay of the near fields is due to fast-wave phase velocity induced by the curvature of the arm. With proper attention to maintaining self-scaling geometry, the log-spiral transmission line antennas can have very nearly constant input impedance over bandwidths greater than 10 to 1. Although the patterns display beams of predominantly circular polarization, asymmetries are observed

AL CANADA STANDARD STANDARD STANDARD STANDARD

that are likely associated with the rate of spiral.

Log-periodic zigzag slot antennas have also been observed to have little large-end truncation. This leads to stable input impedance over wide frequency bands. Near-constant, unidirectional beams are obtained from wedge-shaped LPZZ slot antennas by placing absorber inside the wedge.

#### **ACKNOWLEDGMENTS**

Financial support from the University of Illinois Research Board, the Andrew Corporation, AT&T, and TRW is gratefully acknowledged.

#### REFERENCES

- 1. Dyson, J. D. (1959) The equiangular spiral intenna, <u>IRE</u>
  Trans. Antennas Prop. AP-7:181-187.
- 2. Mayes, P. E. (1964) Balanced backfire zigzag antennas.

  Paper presented at IEEE Inter. Conv., New York.
- 3. Matthaei, G. L., Young, L., and Jones, E. M. T. (1964)

  Microwave Filters, Impedance-Matching Networks and Coupling

  Structures McGraw-Hill, New York.
- 4. Isbell, D. E. (1960) Log-periodic dipole arrays, <u>IRE Trans.</u>
  Antennas Prop. AP-8:260-267.
- 5. Carrel, R. L. (1961) Analysis and design of the log-periodic dipole antenna, Tech. Rept. 52, Contract AF33(616)-6079, Antenna Laboratory, University of Illinois, Urbana.

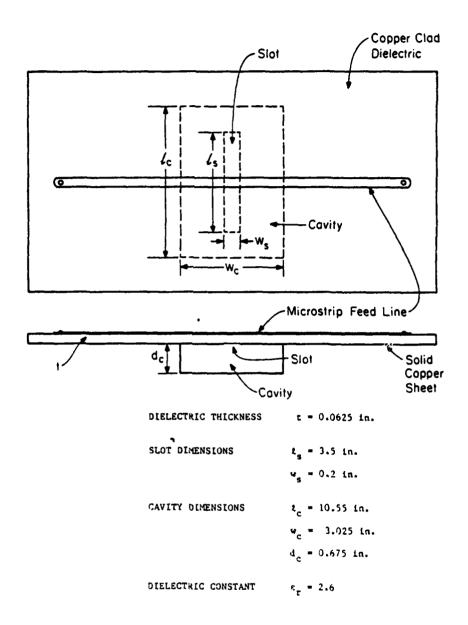
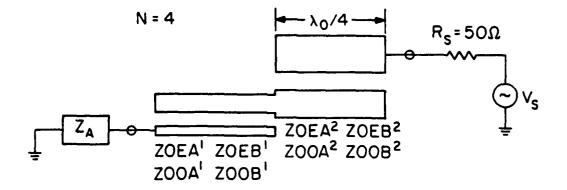
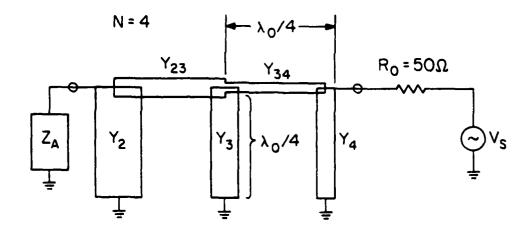


Figure 1. Cavity-backed slot antenna with microstrip feeder.



# a). MATCHING NETWORK FOR A SHUNT-RESONATED LOAD



# b). MATCHING NETWORK FOR A SERIES-RESONATED LOAD

(ONE CASE IS THE DUAL OF THE OTHER)

established bestead bestead bestead bestead by

Figure 2. Parallel coupled line and shunt stub matching networks (N = 4).

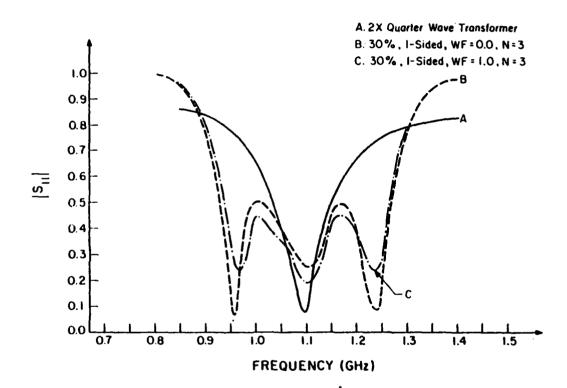
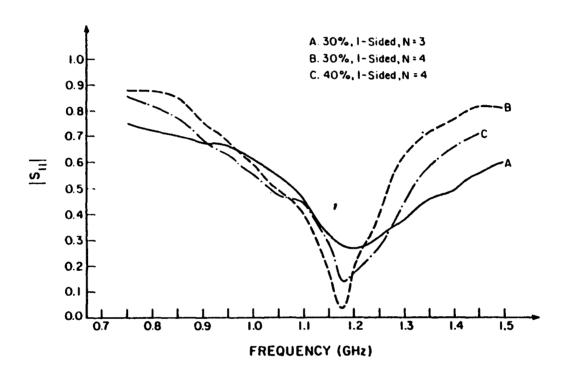


Figure 3. Plots of theoretical calculations for three matching networks. (BW = 30%)



term reservoir sustante expenses expenses reservoir reservoir (passesses syntheta) (reservoir appropriate appropriate despenses appropriate despenses appropriate despenses desp

Figure 4. Measured results for three matching networks.

the restance severes introduce

SOCIATION SECURISE SECURISE (SECURISE)

Parameter acceptant for the property of

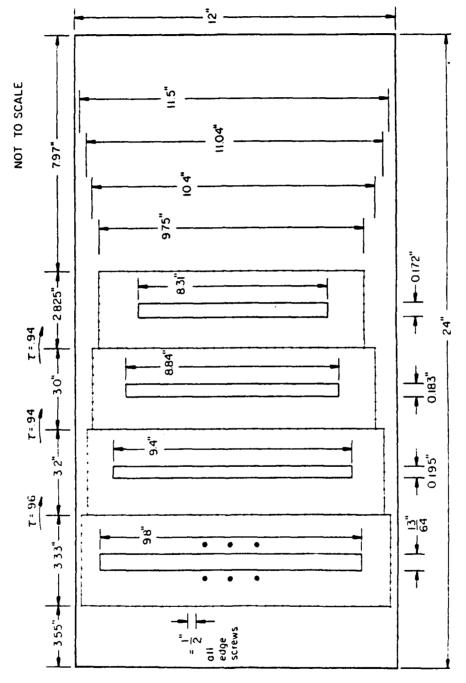


Figure 5. Construction layout of a modified log-periodic cavity-backed slot array.

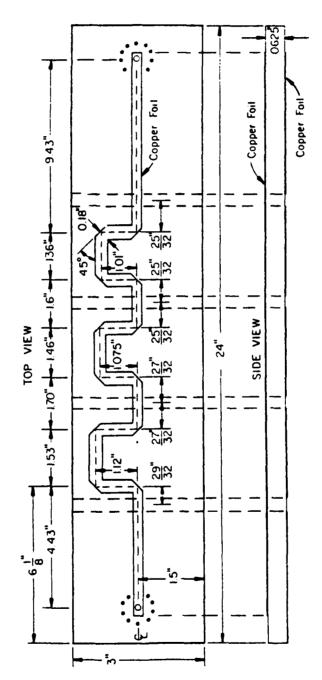


Figure 6. Layout of microstrip feedline for MLPCBS array.

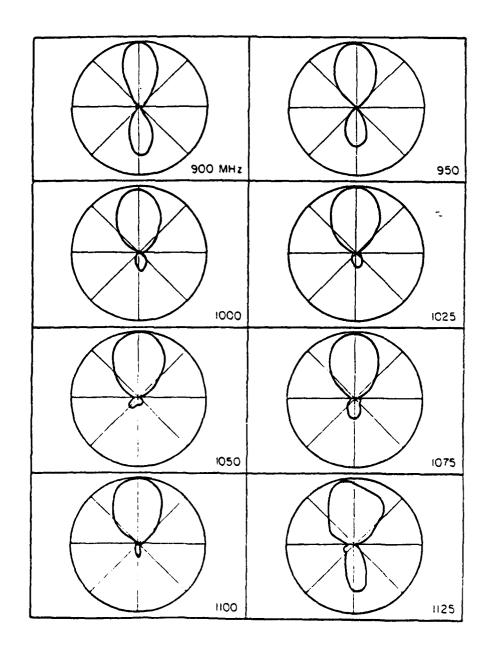


Figure 7. Azimuthal plane principal polarization radiation patterns for MLPCBS array.

Secret Department Department Represent Represent Department of the Secretarian Department of the

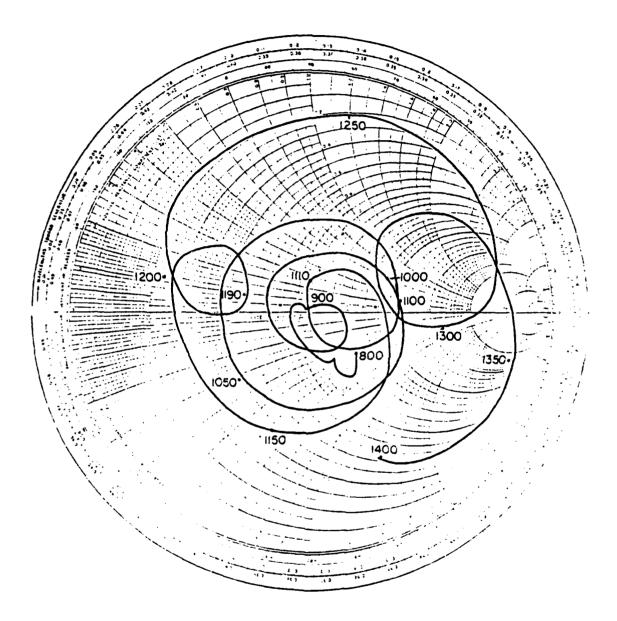


Figure 8.  $S_{11}$  versus frequency for a modified LPCBS array.

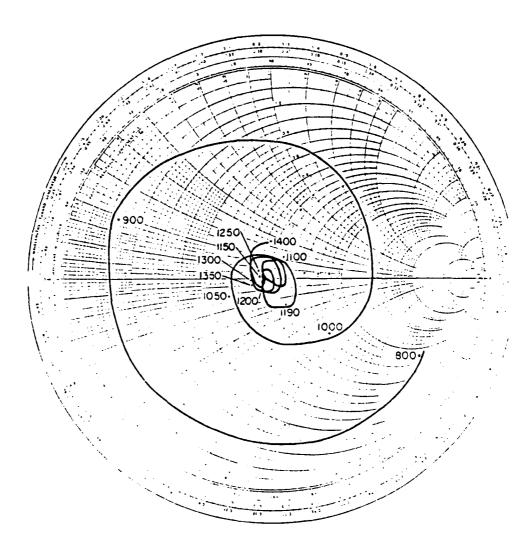


Figure 9.  $S_{21}$  versus frequency for a modified LPCBS array.

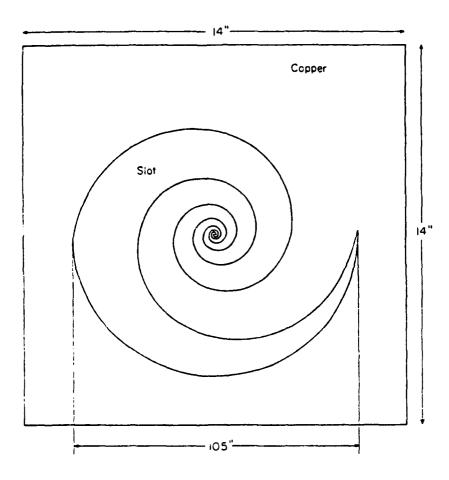


Figure 10. Top view of a planar log-spiral transmission line antenna.

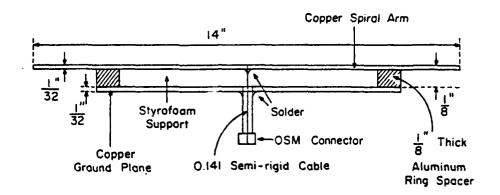


Figure 11a. Side view of the planar log-spiral transmission line antenna.



Figure 11b. Photograph of the planar one-arm log-spiral transmission line antenna.

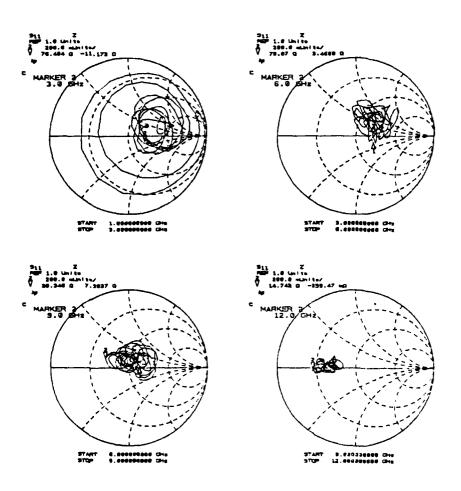


Figure 12. Input impedance of a planar one-arm log-spiral transmission line antenna.

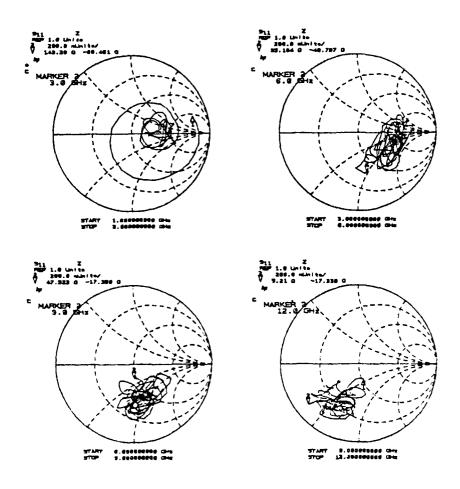


Figure 13. Input impedance of a planar one-arm log-spiral transmission line antenna.

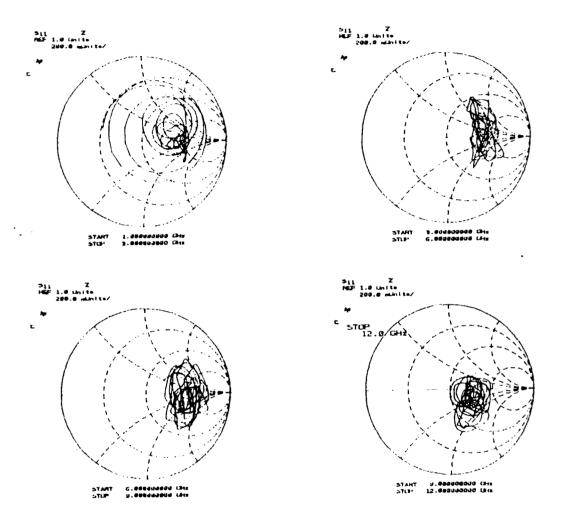


Figure 14. Measured results for a 0.085-in diameter coaxial cable feeding a log-spiral transmission line antenna.

See al Especial Merorana describe a secondario de conservario de c

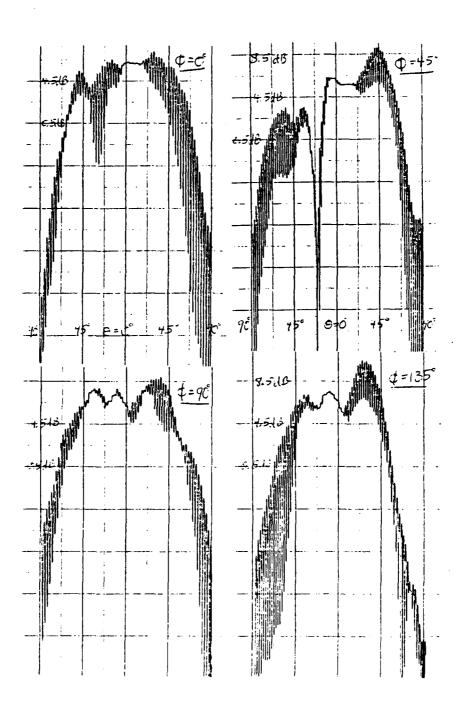


Figure 15. Radiation patterns for the conical one-arm: 5 GHz.

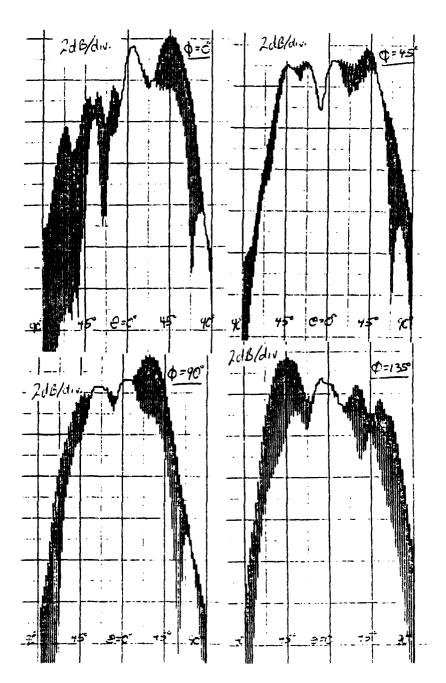


Figure 16. Radiation patterns for the conical one-arm: 6 GHz.

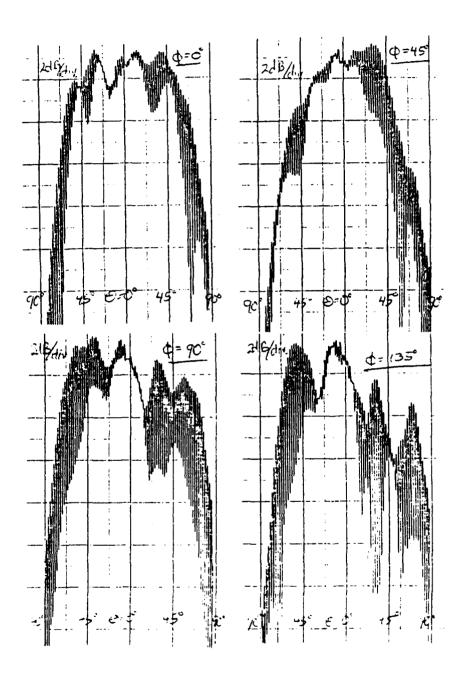


Figure 17. Radiation patterns for the conical one-arm: 7 GHz.

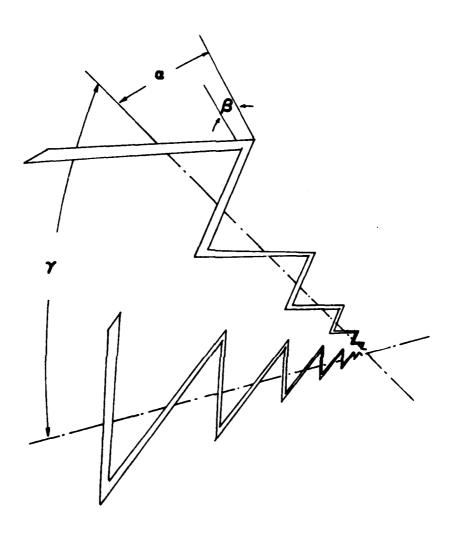


Figure 18. A log-periodic zigzag strip antenna.

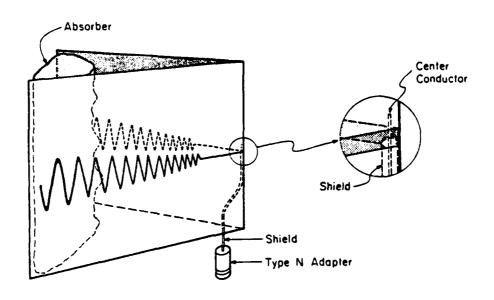
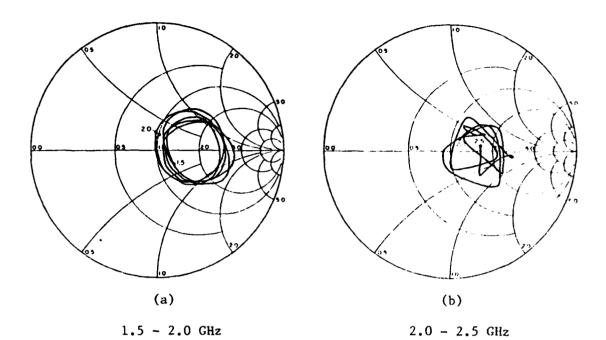


Figure 19. A log-periodic zigzag antenna.



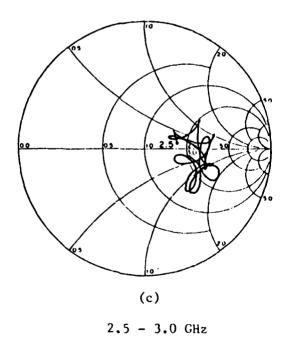
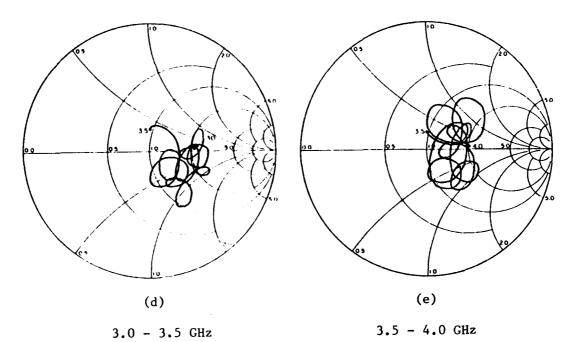
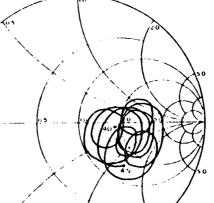


Figure 20. Measured input impedance of an LP ZZ slot antenna.





4.0 - 4.5 GHz

(f)

Figure 20. Continued.

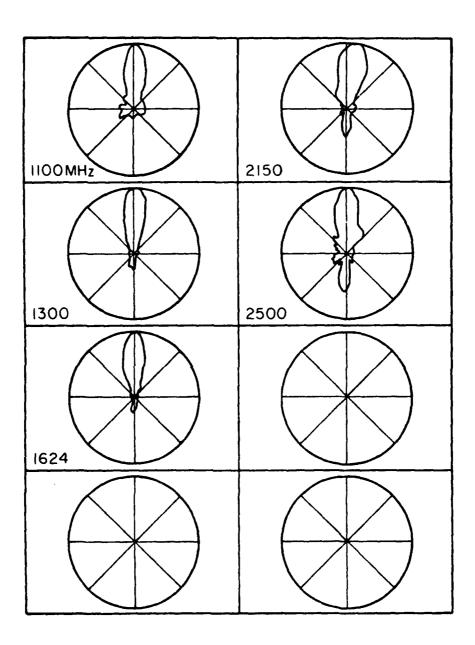


Figure 21. Measured principal plane patterns of an LP ZZ slot antenna.

# A DUAL FEED DUAL POLARIZED LOG-PERIODIC HF ANTENNA SYSTEM

D.V. Campbell, P. Dubowicz
B. Feigenbaum, K. Loffer
U.S. Army Communications Electronics Command
Fort Monmouth, New Jersey 07703

### Abstract

This paper describes а lightweight antenna log-periodic HF system incorporating separate feeds and capable of horizontal, vertical or mixed polarization. This antenna system evolved from a narrow band HALF SQUARE ANTENNA prototype. The elevated dual feed system allows this antenna to operate with minimal dependence on the earth and it provides for polarization diversity reception and optional low-angle or high-angle radiation modes.

A full-size experimental antenna was built to cover the 8 to 30 MHz frequency range. Tests confirm that this experimental antenna exhibits the expected broadband impedance certain behavior peculiar to Computer modeling by the log-periodic structures. method-of-moments indicates that this antenna system is capable of good gain and pattern performance.

### 1. Introduction

Effective high frequency antennas, which are also compatible with the varied and demanding requirements peculiar to military tactical communication, are by no means easily engineered. Military radios operate from 2 to 30 MHz or higher and vary in power from watts to kilowatts. The communication systems may be fixed, transportable, vehicular, man portable, or airborne and employ ground wave or ionospheric propagation over short, medium, or long range paths.

The required mobility dictates small antenna size

but electrical performance will be compromised if the antenna is made too small in terms of the wavelength.

The broad frequency range which spans four octaves complicates the design of efficient antennas.

This paper is concerned with an experimental HF log-periodic wire antenna intended to use on short, medium and long range ionospheric paths. Because this antenna incorporates a dual feed system, it can be used for polarization diversity reception or to radiate at high or low take off angles to suit the skywave transmission path.

#### HALF SOUARE ANTENNA PROTOTYPE

## 2.1 Single feed half square antenna

TO BESTURE PROPERTY RECEIVED FOR SOME STATES AND SOME AND SOME STATES AND SOME STATES AND SOME SOME

The log-periodic antenna, which is the subject of this paper, evolved from a prototype known as the HALF SQUARE antenna [1]. This antenna consists of a half wave horizontal wire connected to quarter wave vertical wires at either end. As originally described in the amateur radio literature, one of the vertical wires is fed against ground while the opposite end of the antenna is "open circuited" so that it does not connect to ground. See Fig. 1.

## 2.2 Method-of-moments analysis

The method-of-moments was used to determine the performance of the antennas discussed in this paper.

Solutions were obtained using the MINI-NUMERICAL [2] ELECTROMAGNETICS CODE-MININEC and the NUMERICAL ELECTROMAGNETICS CODE-NEC [3]. These codes provide numerical solutions for the antenna currents from which all of the important antenna properties, such as impedance and radiation patterns, can be computed. These codes are capable of including ground effects. MININEC is a very small code written in BASIC which can be run on a desk top computer. The NEC program is written in FORTRAN and requires a large computer.

# 2.3 Current distribution-single feed

The current distribution on the HALF SQUARE ANTENNA corresponds to that of a full wave antenna having a current node at its midpoint and current loops a quarter wave from each end. See Fig. 2. This distribution causes the currents in the vertical wires to be in phase and radiation to be bidirectional and broadside to the antenna. The E-field polarization is predominantly vertical.

# 2.4 Dual feed half square antenna

By adding a second feed to the HALF SQUARE ANTENNA, and by locating these feeds at the current loops, the antenna can then be excited in two different modes-one favoring low-angle radiation and the other high-angle radiation. By feeding at the current loop, a low

impedance is obtained which is compatible with the impedance of standard coaxial cable transmission line.

Current coupling from one half of the antenna to the other is eliminated by cutting the horizontal wire at its midpoint and inserting an insulator. This separation also reduces the effects of structural unsymmetries.

The half square antenna with dual feed is shown in Fig. 3. This antenna is the basic element used in constructing the log-periodic antenna discussed in section 3.

# 2.5 Current distribution-inphase mode

When the exciting voltages cause the currents in the vertical wires to be inphase, the dual feed HALF SQUARE ANTENNA will then perform essentially the same as the single fed antenna discussed in section 2.3. The current distribution is shown in Fig. 4.

# 2.6 Radiation patterns-inphase mode

The azimuthal and elevation gain patterns for inphase excitation are shown in Figs. 5 and 6. The elevation pattern (Fig. 6.) shows that the HALF SQUARE ANTENNA is a good low-angle radiator and therefore suitable for medium or long range (1500-4000 kilometer) ionspheric paths.

## 2.7 Current distribution-antiphase mode

When the two feeds are excited so that the vertical wire currents are antiphase, the antenna will then favor high-angle radiation and horizontal polarization. The current distribution is given in Fig. 7.

## 2.8 Radiation Patterns-antiphase mode

The azimuthal and elevation gain patterns for antiphase excitation are shown in Figs. 8 and 9. The elevation pattern (Fig. 9.) indicates that the HALF SQUARE ANTENNA radiates effectively at high take-off angles when excited antiphase. High take-off angle radiation is suitable for short range (800 kilometer) ionospheric paths.

#### 3. DUAL FEED LOG-PERIODIC ANTENNA

## 3.1 Description of log-periodic antenna

The dual feed HALF SQUARE ANTENNA prototype discussed above has been incorporated in a log-periodic structure to secure increased gain, unidirectional radiation, wide bandwidth and increased flexibility. The log-periodic antenna is shown in Fig. 10. This antenna is composed of dual feed half square elements dimensioned according to log-periodic design procedures.

### 3.2 Experimental antenna

An experimental 15 element log-periodic antenna was constructed to cover the upper two octaves of the high frequency range. This antenna is designed to operate

from 8 to 30 MHz. The antenna is composed of HALF SQUARE elements made of #14 gauge wire and is supported by two lightweight 40 foot masts. The antenna occupies an area measuring approximately 120 feet long and 70 feet wide. The antenna height decreases to 4 feet at the shortest element.

The antenna elements are arranged and fed in more-or-less the same manner as a conventional log-periodic antenna-except for the dual feed system. Open wire transmission lines are used to feed each half of the antenna. These transmission lines have a characteristic impedance of approximately 300 ohms.

## 3.3 Voltage-standing-wave-ratio

The measured VSWR of the experimental log-periodic antenna between 8 and 32 MHZ is given in Fig. 11. This measurement confirms the broadband impedance behavior of this antenna for both modes of excitation. For this test the antenna was fitted with a 50 ohm combiner and a pair of four-to-one impedance matching transformers.

# 3.4 Theoretical radiation patterns

A computer model of the log-periodic antenna was investigated using NEC. This model was based on the dimensions used in the experimental antenna but only the ten shortest elements were included to reduce computer time.

The calculated radiation patterns at 10 MHz for both modes of excitation are given in Figs. 12, 13, 14, and 15. In general the patterns indicate that the antenna radiates effectively at low angles when excited in the inphase mode and at high angles when excited in the antiphase mode. Similar patterns have been calculated at 15 MHz and at 8 MHz. It is likely that the radiation patterns will not change significantly up to 30 MHz but this has not been confirmed.

## Conclusions

Use of the dual feed HALF SQUARE ANTENNA as the basic element in a log-periodic antenna has been demonstrated experimentally and by numerical modeling. The two independent feeds enable this antenna to be excited inphase or antiphase so that the radiation pattern can be adapted to low-angle or high-angle ionospheric propagation. The dual feed capability also lends itself to polarization diversity reception. This antenna has not been tested with a diversity combiner, however.

#### References

- [1] Vester, B. (1974) The Half Square Antenna, <u>QST</u>

  (March) <u>The American Radio Relay League</u>,

  Newington, Conn.
- [2] Li, S.T., Rockway, J.W., Logan, J.C. and

Tam, D.W.S. (1983) Microcomputer Tools
for Communications Engineering, Artech
House, Inc., Dedham, Mass.

[3] Burke, G.J. and Poggio, A.J. (1981)

Numerical Electromagnetics Code (NEC) 
Method of Moments, NOSC TD116, Naval

Ocean Systems Center, San Diego, CA.

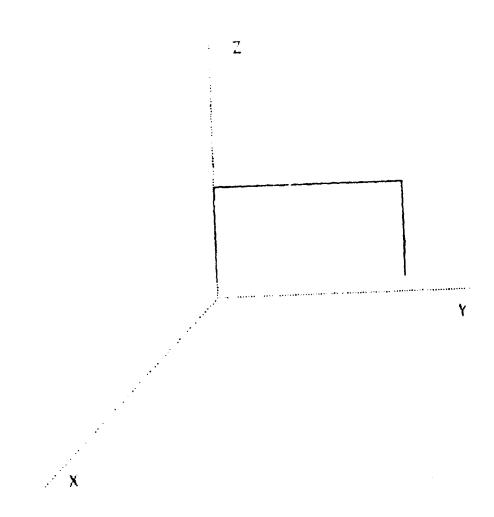


Fig. 1. Single feed half square antenna

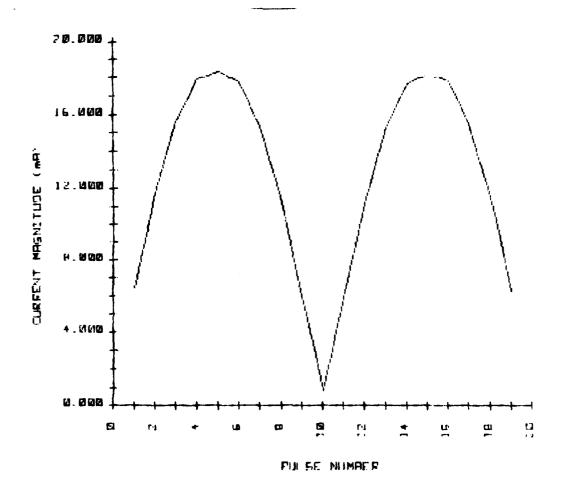


Fig. 2. Current distribution - single feed half square antenna

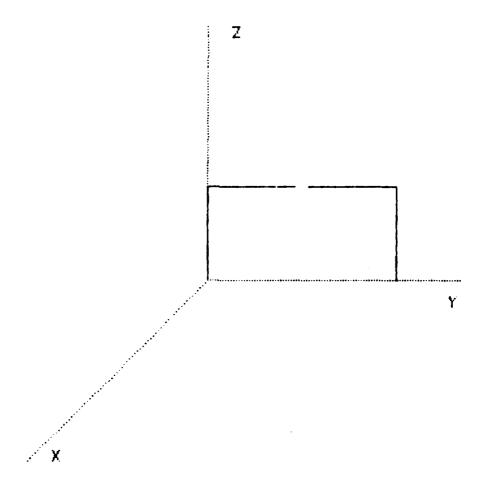
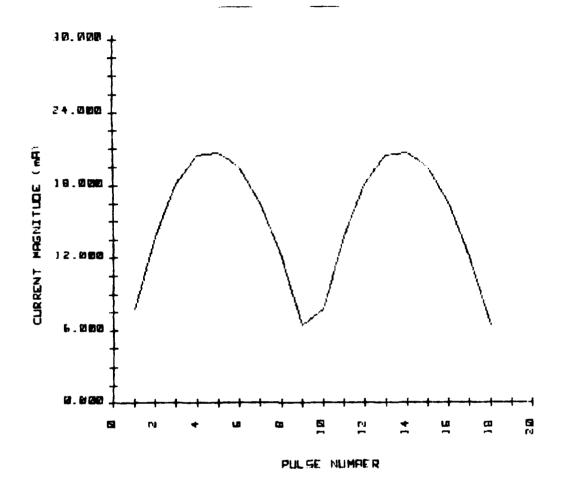


Fig. 3. Dual feed half square antenna

teres consisses, especies estresses menerally process requires incresses meninger (presented possible)



STATES STATES SECTION SECTIONS OF SECTIONS

ASSESSED ASSESSED TO THE PASSESSED TO THE PASSESSED ASSESSED TO THE PASSESSED TO THE PASSES

Fig. 4. Current distribution - inphase mode-Dual feed half square antenna

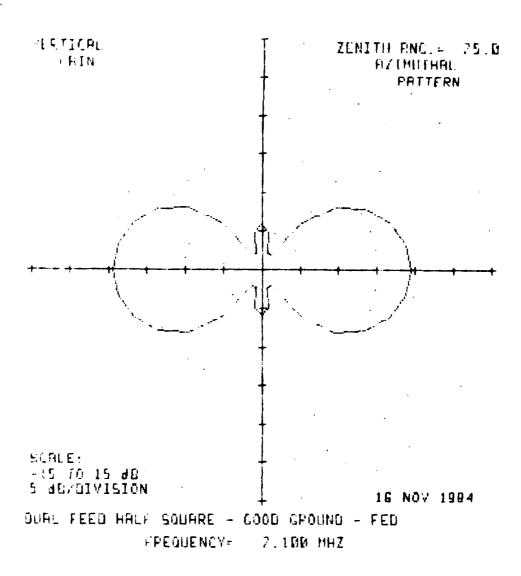


Fig. 5. Azimuthal pattern - inphase mode Dual feed half square antenna

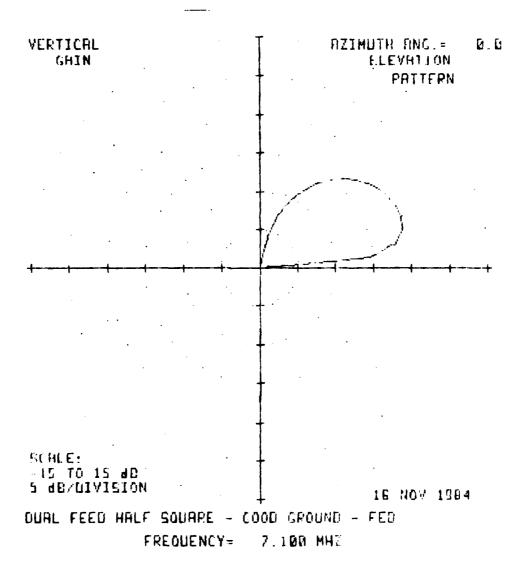


Fig. 6. Elevation pattern - inphase mode Dual feed half square antenna

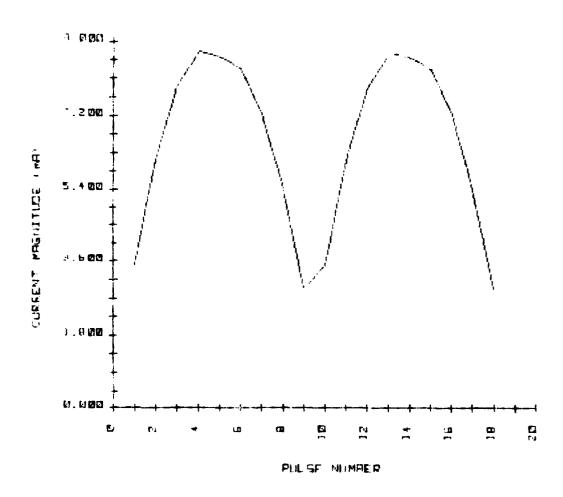


Fig. 7. Current distribution - antiphase mode Dual feed half square antenna

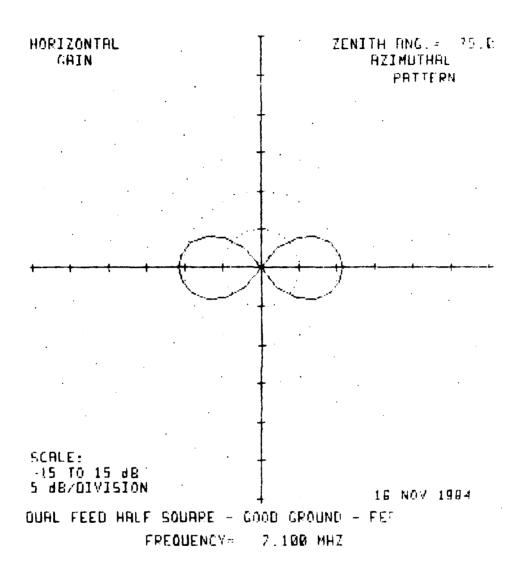


Fig. 8. Azimuthal pattern - antiphase mode Dual feed half square antenna

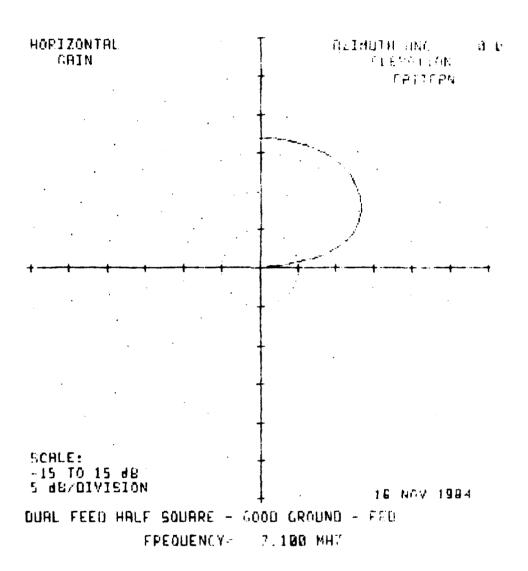


Fig. 9. Elevation pattern - antiphase mode Dual feed half square antenna

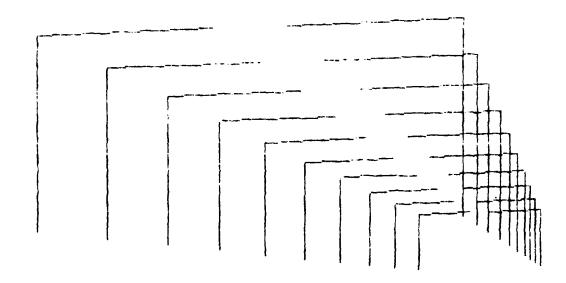
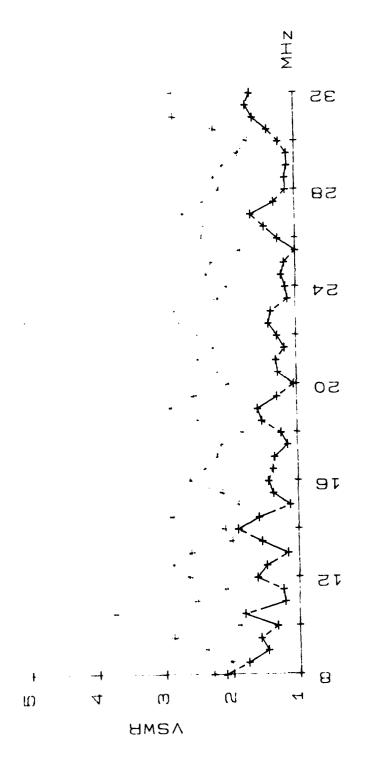


Fig. 10. Dual feed dual polarized log-periodic antenna



Measured VSWR - experimental dual feed log-periodic antenna

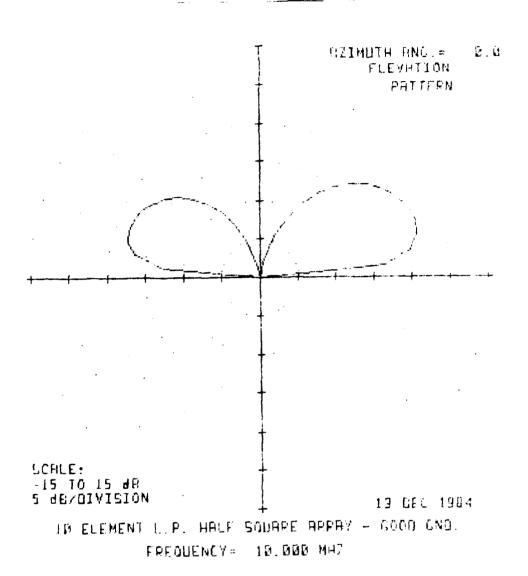


Fig. 12. Elevation pattern - inphase mode Dual feed log-periodic antenna

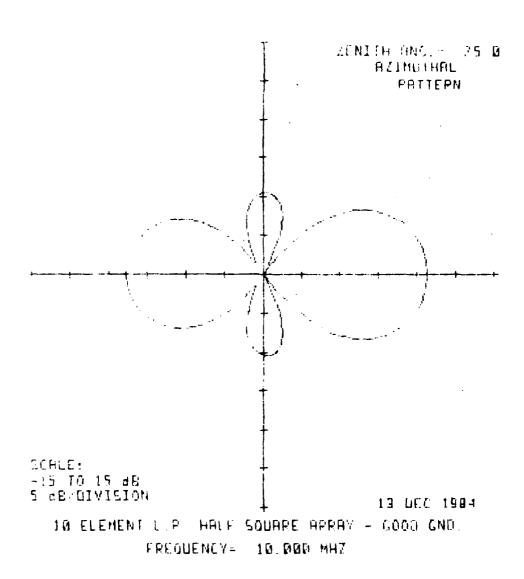


Fig. 13. Azimuthal pattern - inphase mode Dual feed log-periodic antenna

department of the second of th

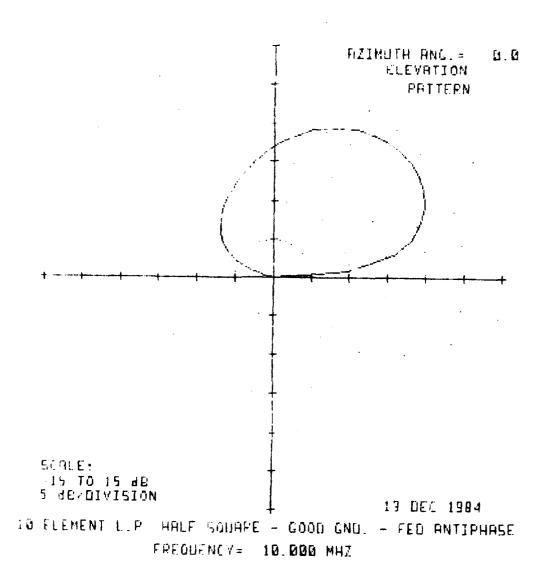


Fig. 14. Elevation pattern - antiphase mode Dual feed log-periodic antenna

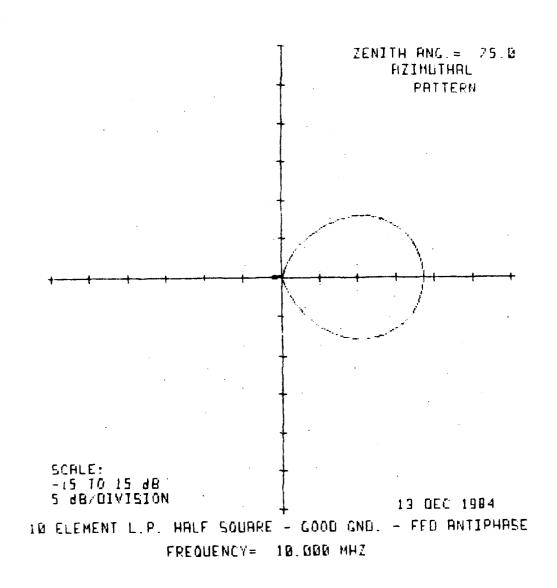


Fig. 15. Azimuthal pattern - antiphase mode Dual feed log-periodic antenna

CONTRACTOR STATES OF THE RESIDENCE SECTION OF THE S

## A DUAL FREQUENCY MICROSTRIP ANTENNA FOR Ka BAND

Richard Q. Lee and Maurice F. Baddour National Aeronautics and Space Administration Lewis Research Center Cleveland, Ohio 44135

#### SUMMARY

For fixed satellite communication systems at Ka band with downlink at 17.7 to 20.2 GHz and uplink at 27.5 to 30.0 GHz, the focused optics and the unfocused optics configurations with monolithic phased array feeds have often been used to provide multiple fixed and multiple scanning spot beam coverages. It appears that a dual frequency microstrip antenna capable of transmitting and receiving simultaneously is highly desirable as an array feed element. This paper describes some early efforts on the development and experimental testing of a dual frequency annular microstrip antenna. The antenna has potential application for use in conjunction with a monolithic microwave integrated circuit device as an active radiating element in a phased array of phased array feeds. The antenna is designed to resonate at TM<sub>12</sub> and TM<sub>13</sub> modes and tuned with a circumferential microstrip ring to vary the frequency ratio. Radiation characteristics at both the high and low frequencies are examined. Experimental results including radiating patterns and swept frequency measurements are presented.

#### INTRODUCTION

Microstrip antennas are attractive as radiating elements for space communication systems because of their inherent advantages of compact structure, weight and cost. Dual frequency microstrip antennas have the additional feature that a single antenna element can transmit or receive in two discrete bands simultaneously. The research on dual frequency microstrip antenna has been extensive, and many different configurations have been described (refs. 1 and 2). However most of the work reported thus far are for low frequency applications. Recently, a hybrid multiport theory for analyzing these antennas has been developed (ref. 3). Theoretical results based on this theory are found to be in excellent agreement with measured results.

The annular microstrip antenna appears uniquely suited for dual frequency application. Unlike rectangular microstrip antennas, the resonant frequencies of such antennas are not harmonically related. Thus, the frequency ratio of any two modes can be varied by choosing the inner and outer radii. In addition, higher gain and easier matching can be achieved, for the size of the annular microstrip is generally larger than the rectangular microstrip antenna at Ka band.

This paper describes some early efforts on the design and experimental testing of dual frequency annular microstrip antennas at Ka band. Preliminary experimental results for a single annular microstrip antenna and a 2 by 2 microstrip array are presented. No attempt has been made to optimize the antenna performance. Thus, the results obtained thus far primarily established the feasibility of this approach and the potential for future improvement.

## Annular Microstrip Antenna Design

Based on a radial cavity model for a thin microstrip antenna and with the application of the usual magnetic wall boundary conditions, the resonant frequency of an annular microstrip antenna, as pictured in figure 1, can be computed from the characteristic equation for the resonant modes (ref. 4):

$$J_{n}^{\prime}(ka)Y_{n}^{\prime}(kb) - J_{n}^{\prime}(kb)Y_{n}^{\prime}(ka) = 0$$

with 
$$k = \frac{\omega}{c} \sqrt{\epsilon_d}$$

where a and b are the inner and outer radii respectively;  $\omega$  is the resonant radian frequency; c is the speed of light, and  $e_d$  is the relative dielectric constant of the substrate. The quantities  $J_n'(x)$  and  $Y_n'(x)$  are the derivatives of the Bessel functions of the first and second kind of order n respectively. The integer n is the azimuthal mode number.

To design the annular microstrip antenna for dual frequency operation, the high and low frequency bands are chosen to satisfy the design requirements of polarization, frequency ratio, antenna dimension and input impedance. In general, the antenna dimension and the resonant frequencies can be easily determined by computing the roots of the characteristic equation for any given radii a and b. However, a more rigorous analysis (ref. 3) must be applied for accurate prediction of the input impedance and radiation patterns.

It has been reported (refs. 5 and 6) that the  $TM_{12}$  mode of the annular microstrip antenna has relatively wide bandwidth and hence is more suitable for antenna applications. Based on this information, the  $TM_{12}$  and  $TM_{13}$  modes have been chosen as operating modes for the Ka band. In order to illustrate the frequency separation between different modes with respect to antenna radii a and b, the resonant frequencies for the lower-order modes of the annular microstrip antenna have been computed numerically using the iteration technique. The results are plotted in figures 2 and 3 as a function of b/a, the ratio of outer radius to inner radius. Figure 2 shows the resonant frequencies of the lower-order modes as a function of b/a with a = 0.1 cm and bvaried; figure 3 shows the same with b = 0.9 cm and a varied. As demonstrated graphically, the variation of the outer radius b produces a greater impact on the resonant frequencies as compared to the inner radius a. With the radii a and b properly chosen, it appears that the frequency requirement for dual frequency operation at Ka band can be satisfied with little frequency tuning required. The resonant frequencies for the TM12 and the TM13 mode and their corresponding frequency ratio for various radii a and b are tabulated in table 1. From these tabulated results, the following observations are made: (1) the frequency ratios decrease with increasing b/a, (2) for cases considered, the frequency ratio is found to be around 1.6, and (3) by holding the inner radius constant, the resonant frequency generally decreases with an increase in the center radius b.

#### EXPERIMENTAL RESULTS

Based on results of table 1, a single annular microstrip antenna with an inner radius a=0.1 cm and an outer radius b=0.93 cm has been fabricated and experimentally tested. Table 2 compares the calculated and the measured

resonant frequencies for the  $TM_{12}$  and the  $TM_{13}$  modes. As shown, the resonant frequencies predicted by the characteristic equation agree reasonably well with the experimentally measured values. The deviation between the calculated and the measured values is found to be about 3 %. The swept frequency measurements for the two frequency bands are displayed in figures 4 and 5. These results clearly demonstrate the feasibility of dual frequency operation at Ka band with a single antenna. The corresponding radiation patterns for the same antenna are shown in figures 6 to 9.

A 2 by 2 microstrip array of identical radiating elements as described above has been fabricated and experimentally tested. The spacing between elements is 2 cm. The array is tested with a symmetric microstrip power dividing network. The radiation patterns for the high and the low frequency bands are shown in figures 10 to 13.

The usefulness of the dual frequency microstrip antennas is greatly enhanced if the frequency ratios can be varied over a wide range. In fact, the bandwidth of the microstrip antenna can be broadened if the two discrete bands of the high and low frequencies has a frequency ratio approaching unity. There exist three well established techniques for frequency tuning. Using these techniques, the frequency ratio of a rectangular microstrip antenna has been effectively reduced to about 1.07 at x-band frequencies or less (ref. 7). Because of the small antenna size at Ka band, frequency tuning of the annular microstrip antenna has been attempted using a circumferential microstrip line. This technique has been found very effective for the TM<sub>12</sub> mode, but less effective for the TM<sub>13</sub> mode. Experimental results illustrating frequency tuning of an annular microstrip antenna are shown in figure 14.

#### CONCLUSION

Preliminary experimental data demonstrate that an annular microstrip antenna can be designed for dual frequency operation at Ka band. By properly choosing the inner and the outer radii of the antenna, a frequency ratio of approximately 1.6:1 between the high and the low frequency bands can be achieved. The resonant frequency of the  $TM_{12}$  mode can be varied over a range of about 1 GHz with a circumferential microstrip line. Further improvement in the antenna performance is possible with better impedance matching and more effective frequency tuning of the  $TM_{13}$  mode.

#### REFERENCES

- 1. Garg, R., and Rao, K.V.S. (1983) Dual Frequency Microstrip Antenna, <u>Electron. Lett.</u> 19:357-358.
- 2. Derneryd, A.G. (1978) Microstrip Disc Antenna Covers Multiple Frequencies, Microwave J. 21:71-99.
- 3. Lo, Y.T., Skupien, C.E., and Zhong, S.S. (1982) A Study of Microstrip Antennas for Multiple Band Operation, RADC-TR-82-236. Final Report, Contract AF-AFOSR-0234-81, Illinois University.

- 4. Wu, Y.S., and Rosenbaum, F.J. (1973) Mode Chart for Microstrip Ring Resonators, IEEE Trans. Microwave Theory Tech. 21:487-489.
- 5. Ali, S.M., Chew, W.C., and Kong, J.A. (1982) Vector Hankel Transform Analysis of Annular-Ring Microstrip Antenna, <u>IEEE Trans. Antennas Propag.</u> 30:637-644.
- 6. Dahele, J.S. and Lee, K.F. (1982) Characteristics of Annular-Ring Microstrip Antenna, <u>Electron</u>. <u>Lett.</u> 18:1051-1052.
- 7. Wang, B.F. and Lo, Y.T. (1984) Microstrip Antennas for Dual-Frequency Operation, IEEE Trans. Antennas Propag. 32:938-943.

TABLE 1. - RESONANT FREQUENCIES FOR  $TM_{12}$  AND  $TM_{13}$  MODES VERSUS ANTENNA RADII a AND b ( $\epsilon_r$  = 2.1)

(a) a fixed, b varied

a	Ь	b/a	f <sub>12</sub>	f <sub>13</sub>	f <sub>13</sub> /f <sub>12</sub>
0.1	0.75	7.5 8.0	22.2	35.9 33.7	1.62
0.1	0.85	8.5 9.0	19.7	31.7	1.60
0.1	0.95	9.5	17.7	28.4 27.0	1.59

# (b) b fixed, a varied

0.06 0.08 0.10 0.12	0.9 0.9			30.1 29.9	1.58 1.59 1.60 1.62
0.14	0.9	6.40	18.3	30.1	1.64

Table 2. - CALCULATED AND MEASURED RESONANT FREQUENCIES FOR THE ANNULAR MICROSTRIP ANTENNA (a = 0.1 cm, b = 0.93 cm,  $\epsilon_r$  = 2.2)

Modes, m,n	Calculated resonant frequency, GHz	Measured resonant frequency, GHz	Deviation, percent
(1.2)	17.7	17.4	1.7
(1.3)	28.3	29.2	3.0

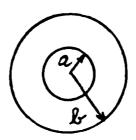


Figure 1. - Annular microstrip antenna.

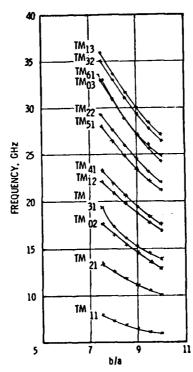


Figure 2 - Resonant frequencies vs b/a with a = 1 cm and b varied,

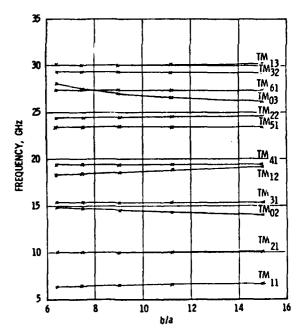


Figure 3, - Resonant frequencies vs b/a with b • .9 cm and a varied,

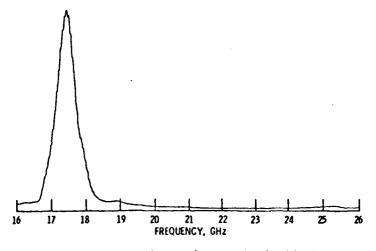


Figure 4 - Relative power vs frequency for an annular microstrip antenna, (Low band),

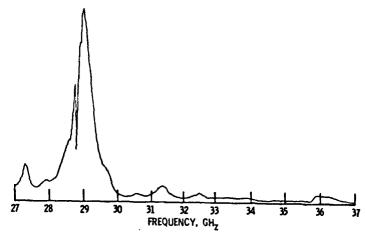


Figure 5. - Relative power vs frequency for an annular microstrip antenna. (High band),

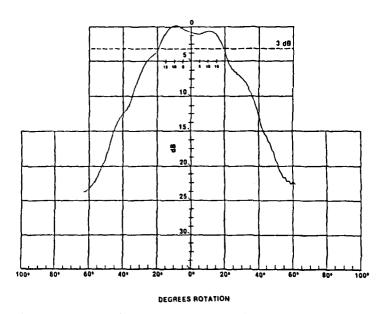


Figure 6. - H - plane radiation pattern of an annular microstrip antenna (f - 17.4 GHz).

SAME INTO THE STATE OF STATES OF STA

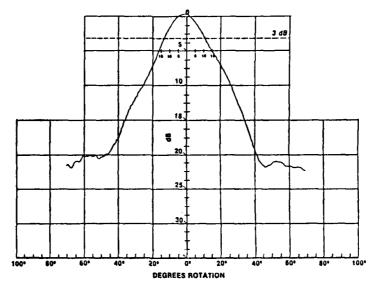
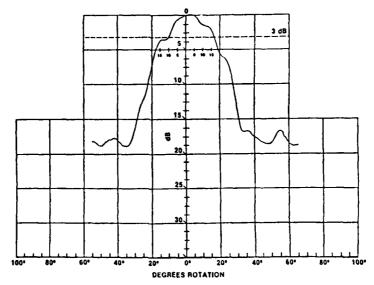


Figure 7. - E - plane radiation pattern of an annular microstrip antenna (f • 17.4 GHz).



ACCOSCONO DE CONTRACTO DE CONTR

Figure 8, - H - plane radiation pattern of an annular microstrip antenna (f = 29, 2 GHz),

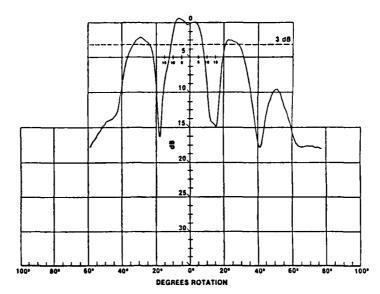


Figure 9. - E - plane radiation pattern of an annular microstrip antenna (f • 29. 2 GHz).

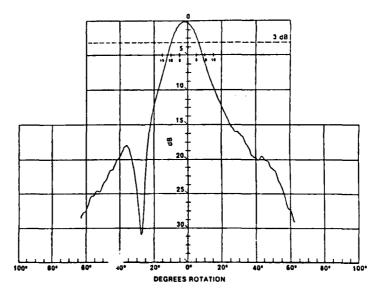


Figure 10. - H - plane radiation pattern of a 2x2 annular microstrip array (f - 17. 4 GHz).

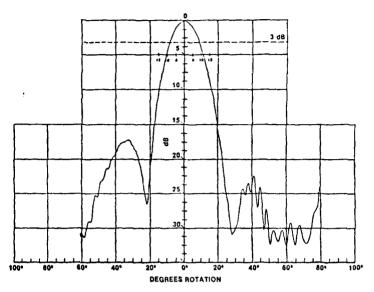
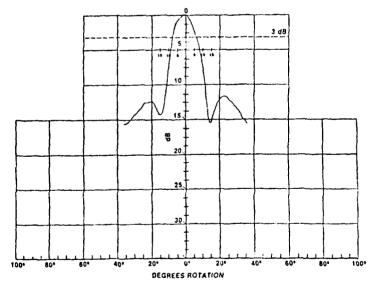


Figure 11. - E - plane radiation pattern of an 2x2 annular microstrip array (f • 17.4 GHz).



THE THE THE PROPERTY OF THE PR

Figure 12. - H - plane radiation pattern of a 2x2 annular microstrip array (f = 29. 2 GHz).

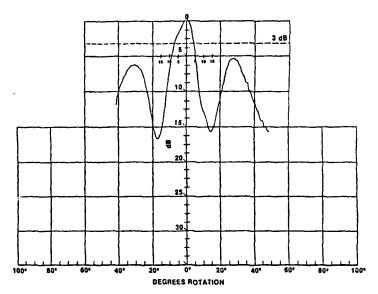


Figure 13, - E - plane radiation pattern of a 2x2 annular microstrip array (f • 29, 2 GHz).

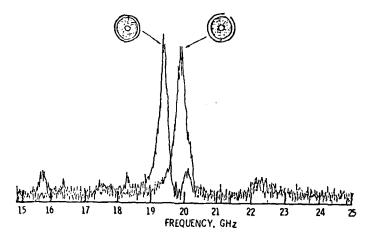


Figure 14 - Frequency tuning of an annular microstrip antenna.

A PROCESSOR BUTTON TO THE PROCESSOR BEST AND THE PROCESSOR BUTTON TO THE PROCE

# A DUAL FREQUENCY MICROSTRIP ANTENNA FOR KA BAND

Richard Q. Lee and Maurice F. Baddour National Aeronautics and Space Administration Lewis Research Center Cleveland, Ohio 44135

#### **SUMMARY**

For fixed satellite communication systems at Ka band with downlink at 17.7 to 20.2 GHz and uplink at 27.5 to 30.0 GHz, the focused optics and the unfocused optics configurations with monolithic phased array feeds have often been used to provide multiple fixed and multiple scanning spot beam coverages. It appears that a dual frequency microstrip antenna capable of transmitting and receiving simultaneously is highly desirable as an array feed element. This paper describes some early efforts on the development and experimental testing of a dual frequency annular microstrip antenna. The antenna has potential application for use in conjunction with a monolithic microwave integrated circuit device as an active radiating element in a phased array of phased array feeds. The antenna is designed to resonate at  $TM_{12}$  and  $TM_{13}$  modes and tuned with a circumferential microstrip ring to vary the frequency ratio. Radiation characteristics at both the high and low frequencies are examined. Experimental results including radiating patterns and swept frequency measurements are presented.

#### INTRODUCTION

Microstrip antennas are attractive as radiating elements for space communication systems because of their inherent advantages of compact structure, weight and cost. Dual frequency microstrip antennas have the additional feature that a single antenna element can transmit or receive in two discrete bands simultaneously. The research on dual frequency microstrip antenna has been extensive, and many different configurations have been described (refs. I and 2). However most of the work reported thus far are for low frequency applications. Recently, a hybrid multiport theory for analyzing these antennas has been developed (ref. 3). Theoretical results based on this theory are found to be in excellent agreement with measured results.

The annular microstrip antenna appears uniquely suited for dual frequency application. Unlike rectangular microstrip antennas, the resonant frequencies of such antennas are not harmonically related. Thus, the frequency ratio of any two modes can be varied by choosing the inner and outer radii. In addition, higher gain and easier matching can be achieved, for the size of the annular microstrip is generally larger than the rectangular microstrip antenna at Ka band.

This paper describes some early efforts on the design and experimental testing of dual frequency annular microstrip antennas at Ka band. Preliminary experimental results for a single annular microstrip antenna and a 2 by 2 microstrip array are presented. No attempt has been made to optimize the antenna performance. Thus, the results obtained thus far primarily established the feasibility of this approach and the potential for future improvement.

#### Annular Microstrip Antenna Design

Based on a radial cavity model for a thin microstrip antenna and with the application of the usual magnetic wall boundary conditions, the resonant frequency of an annular microstrip antenna, as pictured in figure 1, can be computed from the characteristic equation for the resonant modes (ref. 4):

$$J_n'(ka)Y_n'(kb) - J_n'(kb)Y_n'(ka) = 0$$
with  $k = \frac{\omega}{c} \sqrt{\epsilon_d}$ 

where a and b are the inner and outer radii respectively;  $\omega$  is the resonant radian frequency; c is the speed of light, and  $e_d$  is the relative dielectric constant of the substrate. The quantities  $J_n(x)$  and  $Y_n(x)$  are the derivatives of the Bessel functions of the first and second kind of order n respectively. The integer n is the azimuthal mode number.

To design the annular microstrip antenna for dual frequency operation, the high and low frequency bands are chosen to satisfy the design requirements of polarization, frequency ratio, antenna dimension and input impedance. In general, the antenna dimension and the resonant frequencies can be easily determined by computing the roots of the characteristic equation for any given radii a and b. However, a more rigorous analysis (ref. 3) must be applied for accurate prediction of the input impedance and radiation patterns.

It has been reported (refs. 5 and 6) that the  $TM_{12}$  mode of the annular microstrip antenna has relatively wide bandwidth and hence is more suitable for antenna applications. Based on this information, the TM12 and TM13 modes have been chosen as operating modes for the Ka band. In order to illustrate the frequency separation between different modes with respect to antenna radii a and b, the resonant frequencies for the lower-order modes of the annular microstrip antenna have been computed numerically using the iteration technique. The results are plotted in figures 2 and 3 as a function of b/a, the ratio of outer radius to inner radius. Figure 2 shows the resonant frequencies of the lower-order modes as a function of b/a with a = 0.1 cm and bvaried; figure 3 shows the same with b = 0.9 cm and a varied. As demonstrated graphically, the variation of the outer radius b produces a greater impact on the resonant frequencies as compared to the inner radius a. With the radii a and b properly chosen, it appears that the frequency requirement for dual frequency operation at Ka band can be satisfied with little frequency tuning required. The resonant frequencies for the TM12 and the TM13 mode and their corresponding frequency ratio for various radii a and b are tabulated in table 1. From these tabulated results, the following observations are made: (1) the frequency ratios decrease with increasing b/a, (2) for cases considered, the frequency ratio is found to be around 1.6, and (3) by holding the inner radius constant, the resonant frequency generally decreases with an increase in the center radius b.

#### EXPERIMENTAL RESULTS

Based on results of table 1, a single annular microstrip antenna with an inner radius  $\,a=0.1\,$  cm and an outer radius  $\,b=0.93\,$  cm has been fabricated and experimentally tested. Table 2 compares the calculated and the measured

resonant frequencies for the  $TM_{12}$  and the  $TM_{13}$  modes. As shown, the resonant frequencies predicted by the characteristic equation agree reasonably well with the experimentally measured values. The deviation between the calculated and the measured values is found to be about 3 %. The swept frequency measurements for the two frequency bands are displayed in figures 4 and 5. These results clearly demonstrate the feasibility of dual frequency operation at Kaband with a single antenna. The corresponding radiation patterns for the same antenna are shown in figures 6 to 9.

A 2 by 2 microstrip array of identical radiating elements as described above has been fabricated and experimentally tested. The spacing between elements is 2 cm. The array is tested with a symmetric microstrip power dividing network. The radiation patterns for the high and the low frequency bands are shown in figures 10 to 13.

The usefulness of the dual frequency microstrip antennas is greatly enhanced if the frequency ratios can be varied over a wide range. In fact, the bandwidth of the microstrip antenna can be broadened if the two discrete bands of the high and low frequencies has a frequency ratio approaching unity. There exist three well established techniques for frequency tuning. Using these techniques, the frequency ratio of a rectangular microstrip antenna has been effectively reduced to about 1.07 at x-band frequencies or less (ref. 7). Because of the small antenna size at Ka band, frequency tuning of the annular microstrip antenna has been attempted using a circumferential microstrip line. This technique has been found very effective for the TM<sub>12</sub> mode, but less effective for the TM<sub>13</sub> mode. Experimental results illustrating frequency tuning of an annular microstrip antenna are shown in figure 14.

#### CONCLUSION

Preliminary experimental data demonstrate that an annular microstrip antenna can be designed for dual frequency operation at Ka band. By properly choosing the inner and the outer radii of the antenna, a frequency ratio of approximately 1.6:1 between the high and the low frequency bands can be achieved. The resonant frequency of the  $TM_{12}$  mode can be varied over a range of about 1 GHz with a circumferential microstrip line. Further improvement in the antenna performance is possible with better impedance matching and more effective frequency tuning of the  $TM_{13}$  mode.

#### REFERENCES

1. Garg, R., and Rao, K.V.S. (1983) Dual Frequency Microstrip Antenna, Electron. Lett. 19:357-358.

SAN THE SECOND STATE OF THE SECOND STATE OF THE SECOND SEC

- 2. Derneryd, A.G. (1978) Microstrip Disc Antenna Covers Multiple Frequencies, Microwaye J. 21:71-99.
- 3. Lo, Y.T., Skupien, C.E., and Zhong, S.S. (1982) A Study of Microstrip Antennas for Multiple Band Operation, RADC-TR-82-236. Final Report, Contract AF-AFOSR-0234-81, Illinois University.

- 4. Wu, Y.S., and Rosenbaum, F.J. (1973) Mode Chart for Microstrip Ring Resonators, <u>IEEE Trans. Microwave Theory Tech.</u> 21:487-489.
- 5. Ali, S.M., Chew, W.C., and Kong, J.A. (1982) Vector Hankel Transform Analysis of Annular-Ring Microstrip Antenna, <u>IEEE Trans. Antennas Propag.</u> 30:637-644.
- 6. Dahele, J.S. and Lee, K.F. (1982) Characteristics of Annular-Ring Microstrip Antenna, <u>Electron</u>. <u>Lett.</u> 18:1051-1052.
- 7. Wang, B.F. and Lo, Y.T. (1984) Microstrip Antennas for Dual-Frequency Operation, IEEE Trans. Antennas Propag. 32:938-943.

TABLE 1. – RESONANT FREQUENCIES FOR  $\text{TM}_{12}$  AND  $\text{TM}_{13}$  MODES VERSUS ANTENNA RADII a AND b ( $\epsilon_r$  = 2.1)

(a) a fixed, b varied

a	b	b/a	f <sub>12</sub>	f <sub>13</sub>	f <sub>13</sub> /f <sub>12</sub>
0.1 0.1 0.1 0.1 0.1	0.75 0.80 0.85 0.90 0.95	7.5 8.0 8.5 9.0 9.5	22.2 20.9 19.7 18.7	35.9 33.7 31.7 29.9 28.4	1.62 1.61 1.60 1.60 1.59

(b) b fixed, a varied

0.06 0.08 0.10 0.12	0.9 0.9		30.1 29.9	1.58 1.59 1.60 1.62
0.14		 18.3		1.64

Table 2. - CALCULATED AND MEASURED RESONANT FREQUENCIES FOR THE ANNULAR MICROSTRIP ANTENNA (a = 0.1 cm, b = 0.93 cm,  $\epsilon_r = 2.2)$ 

Modes, m,n	Calculated resonant frequency, GHz	Measured resonant frequency, GHz	Deviation, percent
(1.2)	17.7	17.4	1.7
(1.3)	28.3	29.2	3.0

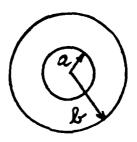
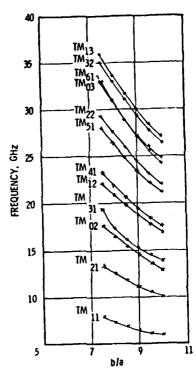


Figure 1. - Annular microstrip antenna.



ACTOR TO THE STATE OF THE STATE

Figure 2 - Resonant frequencies vs b/a with a • 1 cm and b varied.

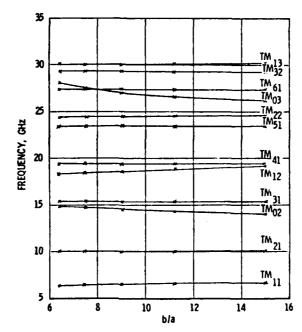


Figure 3. – Resonant frequencies vs b/a with b  $\,\bullet\,$  , 9 cm and a varied,

CONTROL BUSINESS STATES

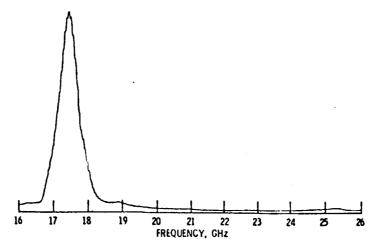


Figure 4. – Relative power vs frequency for an annular microstrip antenna. (Low band).

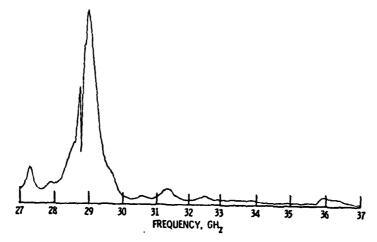


Figure 5. – Relative power vs frequency for an annular microstrip antenna. (High band),  $\,$ 

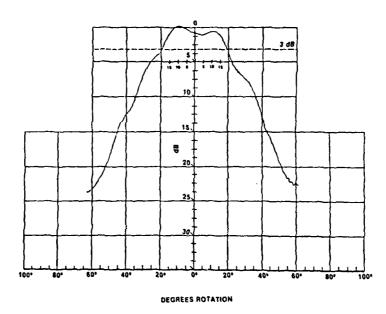


Figure 6. - H - plane radiation pattern of an annular microstrip antenna (f = 17.4 GHz).

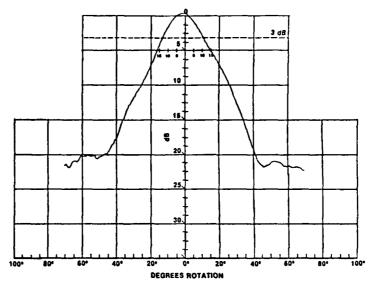


Figure 7. - E - plane radiation pattern of an annular microstrip antenna (f = 17.4 GHz).

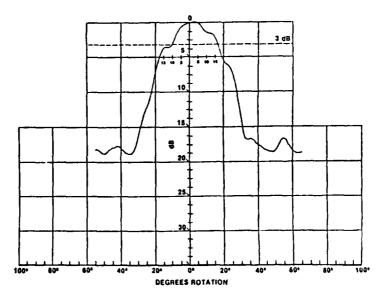
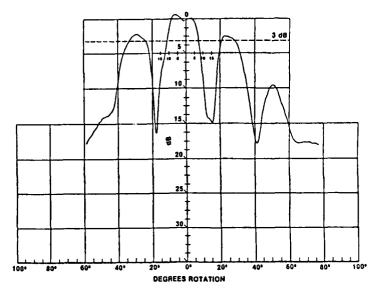


Figure & - H - plane radiation pattern of an annular microstrip antenna (f = 29, 2 GHz).



areases seems seems seems seems

Figure 9. - E - plane radiation pattern of an annular microstrip antenna (f • 29. 2 GHz).

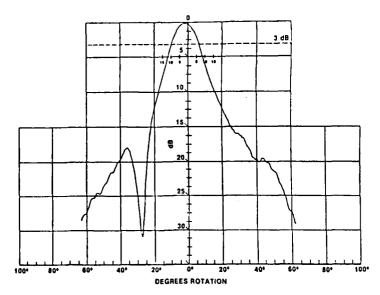


Figure 10. - H - plane radiation pattern of a 2x2 annular microstrip array (f - 17. 4 GHz).

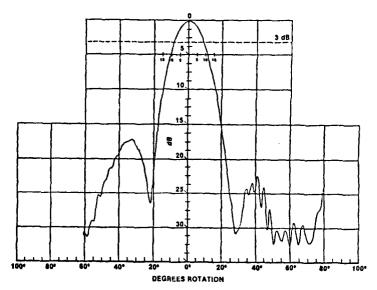
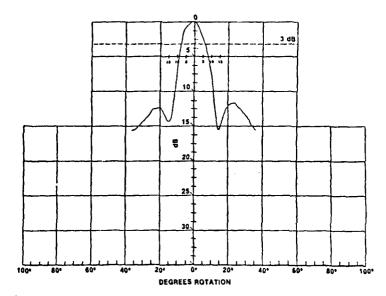


Figure 11, - E - plane radiation pattern of an 2x2 annular microstrip array (f • 17, 4 GHz).



DOCUMENT CONTRACTOR OF THE PROPERTY OF THE PRO

Figure 12. - H - plane radiation pattern of a 2x2 annular microstrip array (f = 29, 2 GHz).

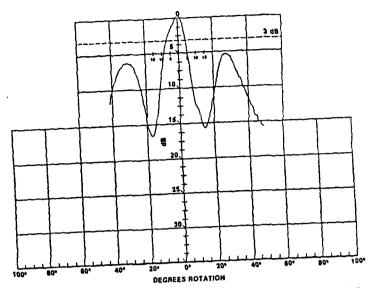


Figure 13. - E - plane radiation pattern of a 2x2 annular microstrip array (f • 29. 2 GHz).

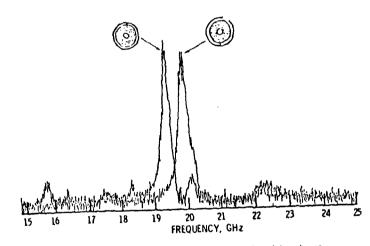


Figure 14. - Frequency tuning of an annular microstrip antenna,

# TRAVELING-WAVE DIPOLE APRAY FOR HE-VHE-UHF TACTICAL DE SYSTÈMS

SAMIC. KUO, HOLLY COOK \*, HOWARD HOCHMAN

GTE GOVERNMENT SYSTEMS

P.O. BOX 7188

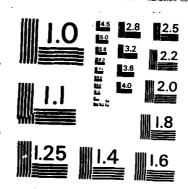
MOUNTAIN VIEW, CALIFORNIA 94039

# **ABSTRACT**

Dipole antennas are often used in tactical direction-finding (DF) systems. Dipoles, however, are basically narrowband antennas, not ideally suited for this application. A modified dipole, called the "traveling-wave dipole", overcomes the drawbacks of the conventional dipole. The TWD has fairly constant input impedance and radiation properties as a function of length and frequency, which allow a DF system performance superior to that available with the conventional dipole.

<sup>\*</sup>H. Cook was formerly with GTE G3C WD and is now with Ford Aerospace & Communication Corp., Palo Airo, CA.

PROCEEDINGS OF THE 1985 ANTENNA APPLICATIONS SYMPOSIUM VOLUME 1(U) ROME AIR DEVELOPMENT CENTER GRIFFISS AFB NY DEC 85 RADC-TR-85-242-VOL-1 MD-8166 754 374 UNCLASSIFIED F/G 9/5 NL



MICROCOPY TEGOLOTION TEST CHART
NATIONAL BUREAU OF STANDARDS-1963-A

# 1.0 INTRODUCTION

The most common antenna configuration used in tactical HF-VHF-UHF direction-finding systems consist of four vertical dipoles arranged in a square, in the manner of a four-element Addock array as shown in Figure 1. Four sets of dipole antennas are used to cover the 20 to 1000 MHz range. The arrays are stacked vertically on a metallic supporting mast according to frequency band, with the smallest array on top of the mast. The direction of an incoming signal is determined by comparing the times of arrival of the RF signal at each baseline, which usually consists of two adjacent dipole antennas. The DF accuracy of the antenna arrays depends on the following:

- A. The Spacing Between Dipole Antennas in Each Baseline
  - The larger the baseline, the better the DF accuracy. However, the maximum spacing is limited by the wavelength at the highest operating frequency. If the spacing exceeds one-half wavelength, ambiguities will occur.
- B. The Impedance and Radiation Pattern Characteristics of The Dipole Antennas

The performance of the dipole antennas in each frequency band is determined by the number of arrays used to obver the required frequency range of 20 to 1000 MHz. It should be noted that

different bands have different operating bandwidth. The lower—frequency bands typically have larger bandwidths while the higher—frequency bands are required to cover only octave frequency bands. Dipole antennas, are inherently not broadband antennas. The overall system performance will be better if the frequency coverage of each array is kept relatively small. Unfortunately, each additional array means a higher mast, more RF distribution components, or more receivers, which will increase the mechanical components and cost.

C. The Similarity in Performance of Different Dipole Antenna.

The far-field phase characteristics of each dipole should be nearly identical, although calibration can eliminate some of the errors; however, it is time-consuming and costly.

Although this type of system usually consists of four or more sets of antenna arrays. A three array system has recently been proposed.

# 2.0 TECHNICAL DISCUSSION

Conventional dipoles are relatively narrow band antennas. For a relatively thin dipole (L/D  $\geq$  40), a VSWR of 3:1 can be obtained over approximately a 60% bandwidth. For dipoles with an L/D ratio less than 10, a VSWR of less than 3:1 can be obtained over almost an obtave. The LP ratio,

however, cannot be reduced indefinitely because of the increase in weight and wind resistance. The common approach to design the cipoles for the 20 to 150 MHz band is to make the dipoles as long as possible before the radiation patterns split and have rulls on or near the horizon at the highest operating frequency. The pattern split usually occurs when the 'ength of the dipole antenna approaches  $1.4\chi$ . Therefore, if the length of the dipole antenna is limited to 1.4 $\lambda$  at 150 MHz, it will be less than 0.2 $\lambda$  at 20 MHz. A conventional dipole antenna whose electrical length is less than Ū.2λ is characterized by low efficiency and extremely high VSWR. in practice, however, the dipole antennas are made even shorter, on the order of 1.0  $\lambda$  or less at 150 MHz to reduce mutual coupling between the dipole pairs and between the dipoles and the metallic supporting most, thus further degrading the VSWR at 20 MHz. The high VSWR's are especially undesirable for this type of DF system because of the interaction between the components, which introduces additional phase errors and degrades the systems accuracy. Hence, DF systems using conventional dipoles often use attenuators at the output of the antenna in order to improve the impedance match between the dipoles and the RF processing components. This is demonstrated by the measured impedance of a conventional dipole which was designed for a prototype 20 to 150 MHz tactical DF system. Figure 2 illustrates the swept input impedance of this dipole for 20 to 150 MHz in free space (no mutual coupling). The dotted line represents the input impedance measured at the input to the dipole, and the solid line represents the input impedance at the output of the transformer with a 4 dB attenuator in series. These attenuators, valued in the 4 to 5dB range,

STATE OF THE PARTY OF THE PARTY

RESERVED TO THE PROPERTY OF TH

unfortunately reduce the systems sensitivity over the entire operating frequency range. Although the lower frequencies of the 20 to 150 MHz band are in the externally-noise-limited range, a 4 or 5 dB loss in the antenna gain can be easily recovered with RF amplifiers. A 4 or 5 dB loss at the higher frequencies in the 20 to 150 MHz band, however, will severely degrade the system sensitivity. A broadband dipole antenna is needed for this application.

One of the candidates proposed for this DF system is the traveling-wave dipole antenna. The traveling-wave dipole, first introduced by Altshuier in 1960, is capable of operating over a broader frequency range than the conventional dipoles because of a resistor which is inserted in each nait of the dipole at approximately one-quarter  $\lambda/4$  from the end of the dipole at a frequency near the high end of the operating range.

al bosphine besteres besteres convers possessa convers

<sup>1.</sup> Altshuler, Edward E., (July 1961) pp. 324—329, "The Traveling Wave Linear Antenna". IRE Trans, APS.

This antenna operates on the principle that a pure traveling wave can be created by terminating a transmission line in its characteristic impedance. If the transmission line is terminated in an open circuit, a single traveling wave can be obtained by placing a resistor equal to the characteristic resistance of the line in series with the line one-quarter from the open circuit termination. The linear dipole is in two ways similar to the transmission line with the open circuit termination. First, it ends in an open circuit. Second, a standing wave current distribution exists on the antenna. It seemed reasonable to assume that it is possible to create a traveling wave on a dipole antenna by placing a resistor one-quarter wavelength in series from the end.

When this arrangement was carried out experimentally, a traveling-wave current distribution was measured or, the dipole when the proper value resistor was used. VSWR of less than 2.8:1 over a 3.8:1 frequency range was reported by Altshuler. An inductor in parallel with the resistor was later introduced<sup>2</sup> in order to improve the efficiency of the dipole antenna at the lower operating frequencies where a considerable amount of the excitation currents are dissipated in the resistor.

<sup>2.</sup> Guertier, R.J.F., Collyer, G.E., (April 1974) p. 18, "A Broad Band Traveling-Wave Dipole", Amateur Radio (Australia).

# 3.0 EXPERIMENTAL RESULTS

A comparison of traveling wave dipoles and conventional dipoles for use in a HF-VHF direction-finding system is presented next:

3.1 One important difference between the traveling wave dipole and the conventional dipole antenna is the variation of the input impedance with operating frequency. As the electrical length of the antenna varies, the input impedance of the traveling wave dipole remains nearly constant while that of the conventional dipole changes considerably as shown in Figure 2.

The measured input impedance of a 6.5 ft traveling wave dipole, designed to operate from 20 to 150 MHz is shown in Figure 3. We measured the impedance at the output of a balun transformer and was not corrected for its insertion loss. Compared with the input impedance of the conventional dipole, this is well behaved. The VSWR is less than 2.5-1 over about two octaves.

We measured the gain of this traveling wave dipole antennal at the output of the balun transformer: the results are shown in Figure 4. The gain of a conventional dipole antenna, which was designed to cover the 20 to 150 MHz band of a prototype DF system, was also tested and the results are also shown in Figure 4 for comparison.

- 3.2 The second advantage of the traveling-wave dipole for this particular application is in its radiation pattern characteristics. It can be operated over a relatively large frequency range with small variations. Although the radiation pattern of a conventional dipole starts to split when the length of the dipole approaches  $1.4\,\lambda$ , the radiation pattern of a traveling-wave dipole of the same length does not, and it still provides good coverage on the horizon, as shown in Figure 5. Thus, the traveling wave dipoles can be made electrically longer thus improving the VSWR at the lower operating frequencies.
- Another advantage of the traveling wave dipole used for this application is that it is less sensitive to its surroundings when it is placed in a four element square array, with a center mast, because of the traveling wave current distribution. We measured the mutual coupling of two pairs of dipoles; one conventional and the other traveling wave, from 100 to 600 MHz; the results are shown in Figure 6. The length of the conventional dipoles was 18 inches and that of the traveling wave dipoles was 40 inches. It can be observed that the coupling between the two traveling wave dipoles is at least 10 dB better than that of the two conventional dipoles above approximately 300 MHz. Hence, if was not surprising to discover resonance problems and gain dropouts at discrete frequencies (at the higher operating frequencies) when the gain of the individual conventional dipoles was measured in the array configuration. When the four conventional dipoles of the prototype 20 to 150 MHz. DF array were replaced with traveling wave dipoles, the gain dropouts disappeared.

# 4.0 CONCLUSION

Present HF-VHF-UHF tactical direction-finding systems use conventional dipoles to cover the frequency range from 20 to 1000 MHz. In some cases five sets of dipoles are used to cover the range with reasonable phase and sensitivity performance. In some cases, to reduce the physical size of the array, only three sets of dipoles are used; attenuation is added to improve the phase performance at the sacrifice of sensitivity and pattern performance. The traveling wave dipole offers the advantages of both systems. A system consisting of three bands of traveling wave dipoles can offer the performance of a conventional four-band system and the size reduction of a three band system, without the degraded performance.

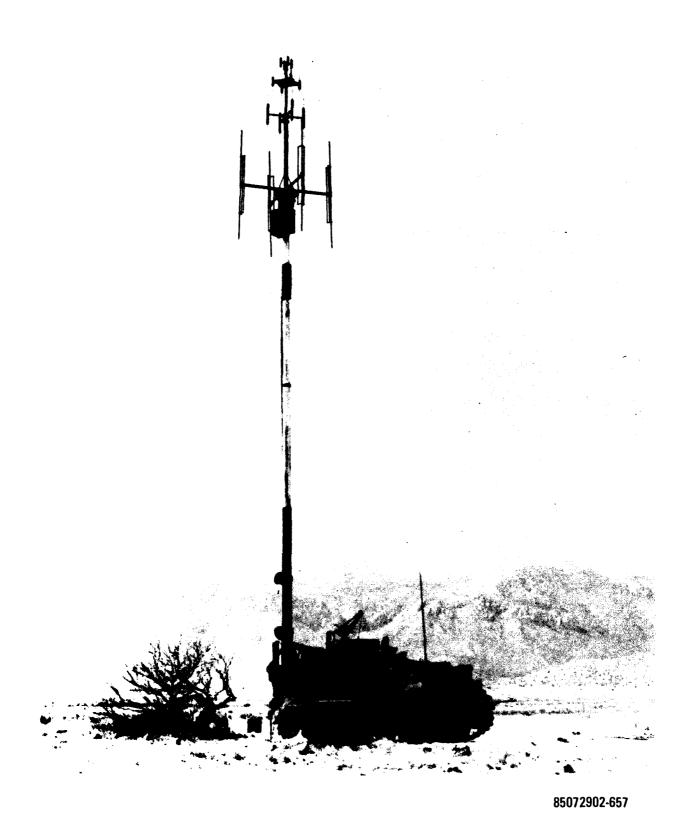


Figure 1. A Tactical HF/VHF/UHF Direction-Finding System

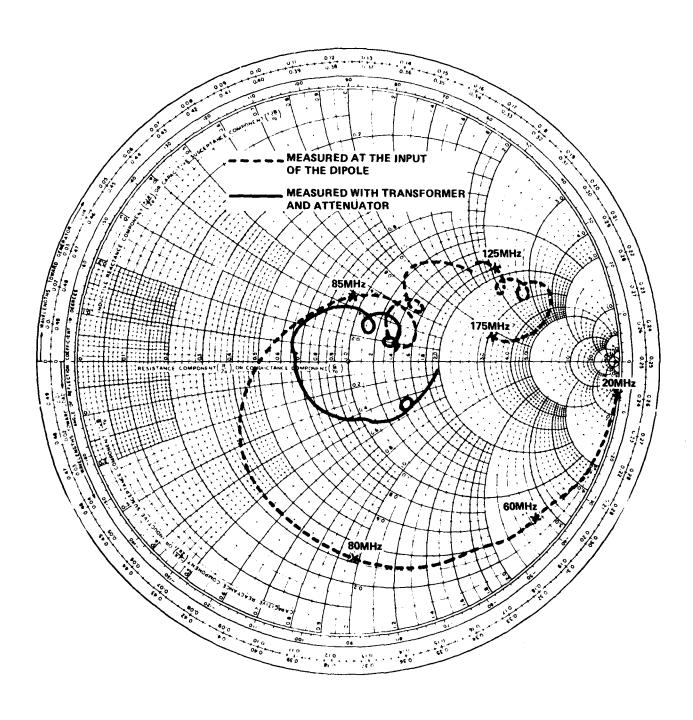


Figure 2. Input Impedance of the Conventional Dipole, Designed for a 20-150 MHz Tactical DF System

AND PROPERTY SOUTH SERVICE SOUTH

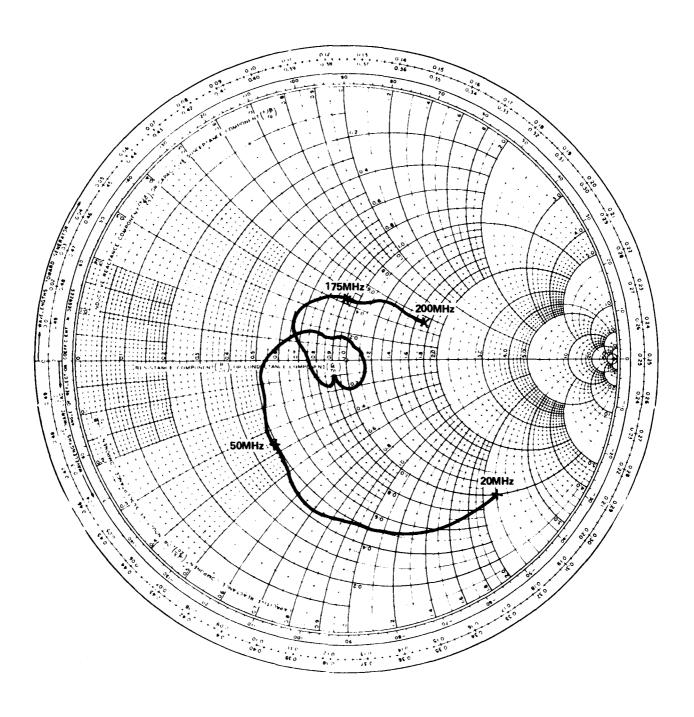
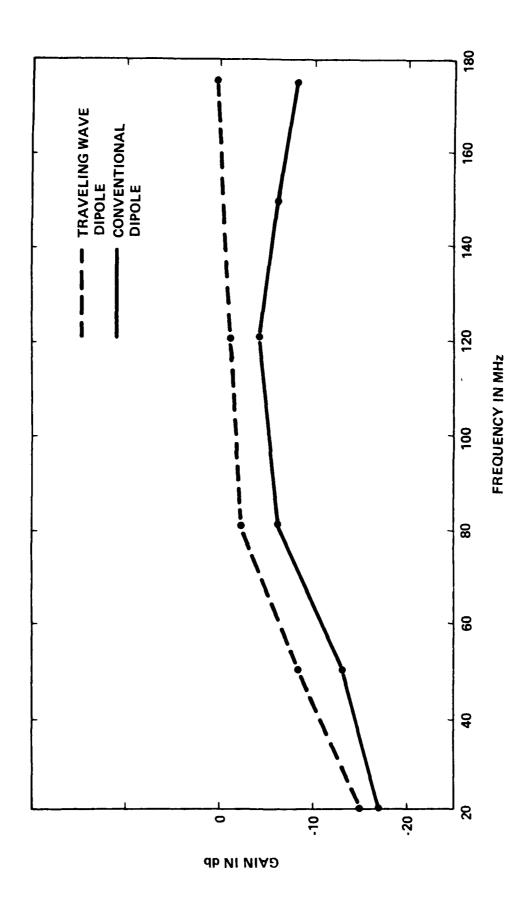


Figure 3. Input Impedance of a Traveling Wave Dipole



rece conserve, substitute michiga

CONTRACT CONSTRUCTION OF THE CONSTRUCTION OF T

Measured Gain of Conventional Dipole Versus Traveling Wave Dipole Figure 4.

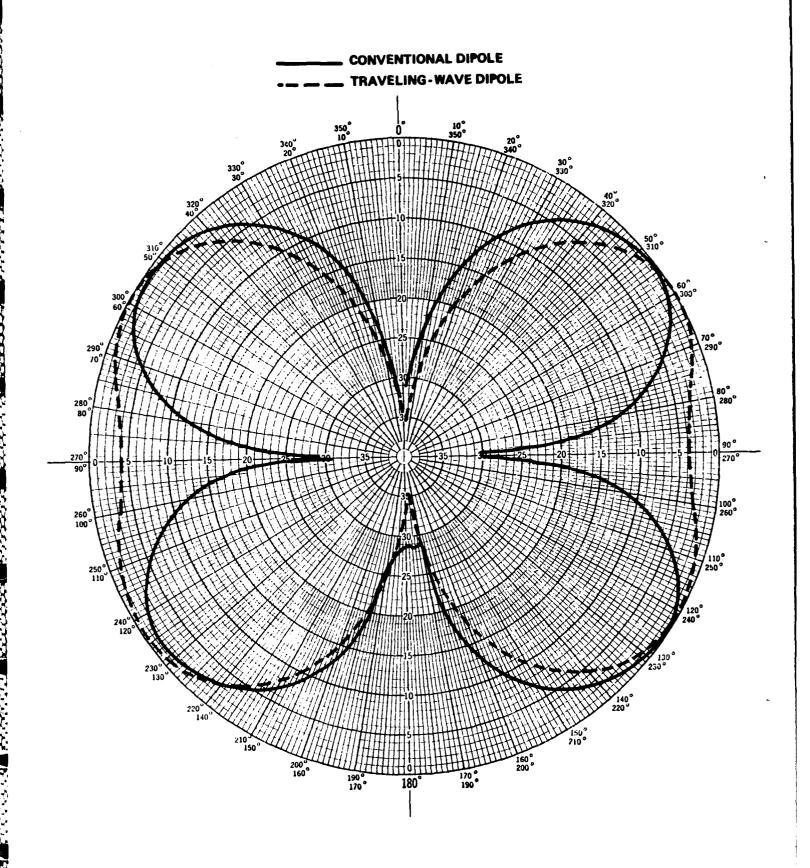
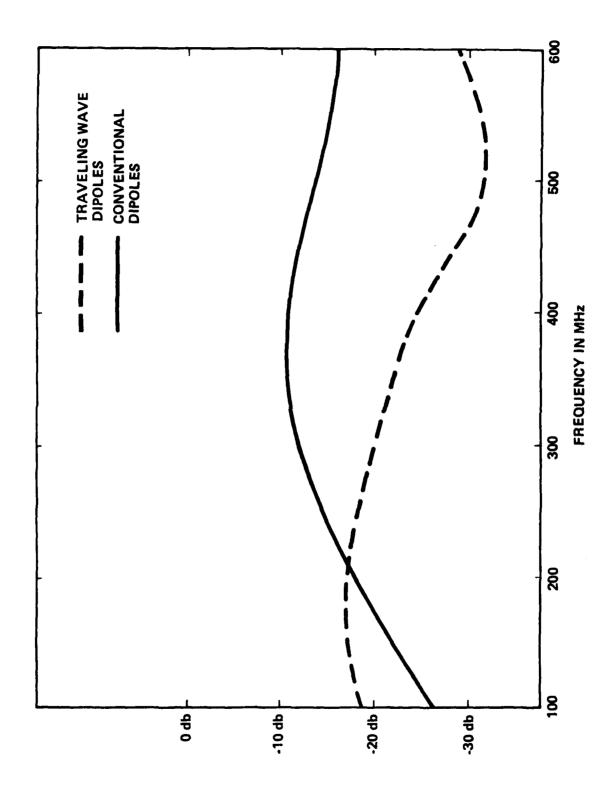


Figure 5. Radiation Patterns of Dipoles, 1.4 Wavelength



Measured Coupling Between Two Dipoles Spaced at 8 Inches Apart Figure 6.

# REDUCTION OF COUPLING BETWEEN COSITED ANTENNAS BY SEPARATION OF NEAR FIELDS

D.V. Campbell, P. Dubowicz, R. Hoverter U.S. Army Communications Electronics Command Fort Monmouth, NJ

## Abstract

Duplex radio communication systems often experience crosstalk interference caused by strong interaction of the cosited transmitting and receiving antennas. This paper explains an easily implemented method whereby high interantenna decoupling may be achieved between two cosited antennas over a broad frequency range. This approach is based on minimizing radiation coupling by separating the antenna near fields and by suppressing extraneous parasitic rf currents on the outer conductors of the coaxial cable antenna feed lines.

An experimental VHF antenna system consisting of two cosited biconical antennas was tested to evaluate feasibility ο£ this near field separation Experiments show that an interantenna isolation exceeding 30 dB from 30 to 90 MHz can be achieved for an antenna spacing of only 8 feet. conventional installation would require at least 40 foot antenna separation to achieve the same isolation. Computer modeling by the method-of-moments theoretical model based on Hertz dipoles support the experimental findings.

#### 1. Introduction

The performance of a duplex radio communication system may be impaired and unpredictable unless the mutual coupling between its cosited antennas is minimized.

For a given separation, it is well known that colinear antennas provide greater interantenna

isolation than parallel side-by-side antennas. For example, colinear dipoles separated by 1.5 wavelengths will provide 35 decibels isolation. On the other hand, a separation of 7 wavelengths would be required to obtain 35 decibels isolation with the parallel side-by-side antenna arrangement.

By providing enough spacing, interantenna isolation can, in principle, be reduced to an acceptable level as dictated by system requirements. At VHF, however, where one wavelength may be 10 meters, neither the colinear nor parallel side-by-side antenna arrangement is practical because of the large separation required.

The antenna system discussed below provides high interantenna isolation with close spacing by means of polarization mismatch which decouples the near fields. With this simple approach one can obtain 35 dB isolation or more between antennas separated by only a fraction of the wavelength. However, since the antennas are tilted with respect to the vertical, the resulting equatorial plane radiation pattern becomes non-circular. The pattern distortion may be tolerable, however.

2. ISOLATION BETWEEN HERTZ DIPOLES IN FREE SPACE

## 2.1 Radiation Coupling

Free space radiation coupling sets an upper bound

for the achieveable interantenna isolation. It can be controlled by antenna spacing and orientation. To establish this upper bound a simplified model consisting of two short dipoles (Hertz dipoles) may be used. See Fig 1.

The interantenna isolation is defined as the fraction of the total power radiated by one antenna which is intercepted by the other. The isolation between Hertz dipoles arranged as in Fig 1. is given by

$$P_R/P_T = 9/16(1/x^6 - 1/x^4 + 1/x^2)\cos^2 A$$
 (1) where  $x=2 \pi r/\lambda$ , r is the spacing,  $\lambda$  is the free space wavelength, and A is the angle between the dipoles. The isolation is shown in Fig. 2. For spacings greater than 0.5 wavelength, the isolation is

$$P_R/P_T = (9/16x^2)\cos^2 A$$
 (2)

with an error of less than 10%. The Friis transmission formula [1] reduces to (2) when the antennas consist of current elements.

# 2.2 Impedance Mismatch

Impedance mismatch adds to the interantenna isolation and is given by [2]

$$g = 1 - (s-1)^2/(s+1)^2$$
 (3)

where S is the voltage standing wave ratio. Either antenna may be mismatched.

#### 3. ORTHOGONAL HALF WAVELENGTH DIPOLES ABOVE GROUND

# 3.1 Method-of-Moments Analysis

The model discussed above provides a good estimate of the achieveable isolation between two dipoles in free space. In this model only radiation coupling was considered.

Scattering from the ground affects the antenna radiation patterns and the interantenna isolation. To determine these effects the method-of-moments was used to model the antenna system. The solution was obtained by means of the MINI-NUMERICAL ELECTROMAGNETICS CODE-MININEC [3]. MININEC solves for all rf currents in the radiating system and calculates input impedances and radiation patterns.

The antenna system modeled consists of a pair of half-wave dipoles over ground. See Fig. 3. In order to include scattering from the transmission line, vertical and horizontal conductors were also incorporated in the computer model.

# 3.2 Calculated Antenna Patterns

The calculated azimuthal radiation patterns of the E-field vertical component at 30, 60 and 90 MHz are

given in Figs. 4, 5 and 6. At 30 MHz and at 60 MHz the patterns are circular within about +/- 1.5 dB. At 90 MHz, the pattern varies by about +/- 4 dB. This pattern distortion is attributed to ground reflections and the mixed polarization of the tilted dipoles.

## 3.3 Calculated Isolation

The theoretical interdipole isolation obtained from MININEC is shown in Fig. 7. The isolation was calculated by means of

$$P_R/P_T = 1/2 \text{ Re } (V_R I_R^*)/1/2 \text{ Re } (V_T I_T^*)$$
 (4)

where  $\mathbf{V}_{R}$  is the receiving antenna load voltage,  $\mathbf{I}_{R}$  is the load current and  $\mathbf{V}_{T}$  ( $\mathbf{I}_{T}$ ) are the transmitting antenna input voltage (current).

#### 4. EXPERIMENTAL RESULTS

## 4.1 Experimental Antenna

SOCIAL SECTION PROPERTY SECTION

A broadband antenna system consisting of a pair of cosited biconical VHF antennas was tested to determine the interantenna isolation and radiation patterns when arranged for minimum coupling. See Fig. 8. In the experimental system the antennas were horizontally separated 3.7 meters and located 9 meters above ground. The biconical antennas were tilted 45 degrees with respect to the vertical and 90 degrees with respect to each other to effect polarization mismatch and near

field separation.

# 4.2 Parasitic Current Suppression

During the experiments, high impedance cable chokes were added in series with the coaxial transmission lines to suppress induced parasitic rf currents [4]. These cable chokes increased and smoothed the interantenna isolation by eliminatng extraneous coupling due to scattering from the transmission lines.

## 4.3 Measured Patterns

The measured equatorial plane patterns of the E-field vertical component at 30, 60 and 90 MHz are shown in Figs. 9, 10 and 11. Pattern distortion is attributed, in part, to scattering from buildings and metal structures at the test site.

## 4.4 Measured Isolation

The measured interantenna isolation is shown in Fig. 12. The isolation varies from 35 decibels to 50 decibels over the 30 to 90 MHz frequency range.

#### Conclusions

The mutual coupling between cosited linear antennas may be controlled and reduced to an acceptable level by means of polarization mismatch and adequate antenna separation. Interantenna isolation exceeding 35 decibels has been demonstrated with only a modest

antenna separation. The method is easily implemented and is practical even at VHF wavelengths. The simplicity of this method is offset, to some degree, by the resulting pattern distortion in the equatorial plane caused by tilting of the antennas. This pattern distortion may, however, be tolerable.

#### References

- [1]. Schelkunoff, S.A. and Friis, H.T. (1952)

  Antennas Theory and Practice, John Wiley & Sons, New York.
- [2]. Stutzman, W.l. and Thiele, G.A. (1981) Antenna
  Theory and Design, John Wiley & Sons, New
  York.
- [3]. Li, S.T., Rockway, J.W., Logan, J.C. and Tam,
  D.W.S. (1983) Microcomputer Tools for
  Communications Engineering, Artech House,
  Inc., Dedham Mass.
- [4]. Campbell, D.V., Fich, S., and Schwering, F.K. (1980) Suppression of Parasitic Currents on Feed Lines of Colinear Dual Antenna Systems, IEEE Trans. Antenna Propagation, Vol. AP-28.

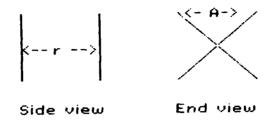


Fig. 1. Hertz dipoles in free space

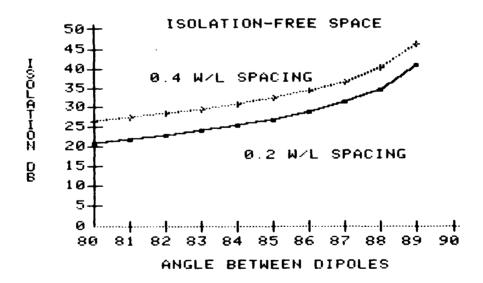


Fig. 2. Isolation between Hertz dipoles in free space

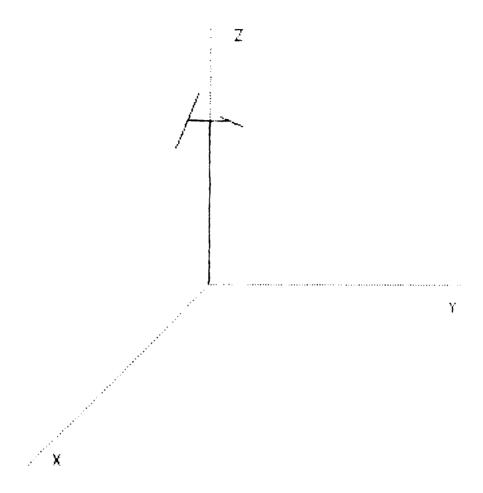


Fig. 3. Crossed half wave dipoles above ground

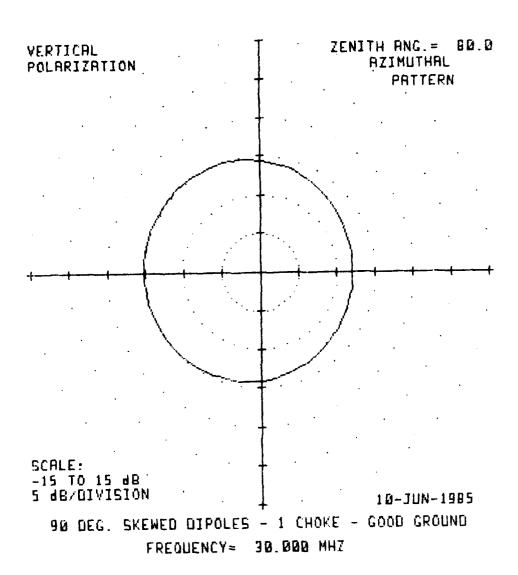


Fig. 4. Calculated pattern of crossed half wave dipoles over ground - 30 MHz

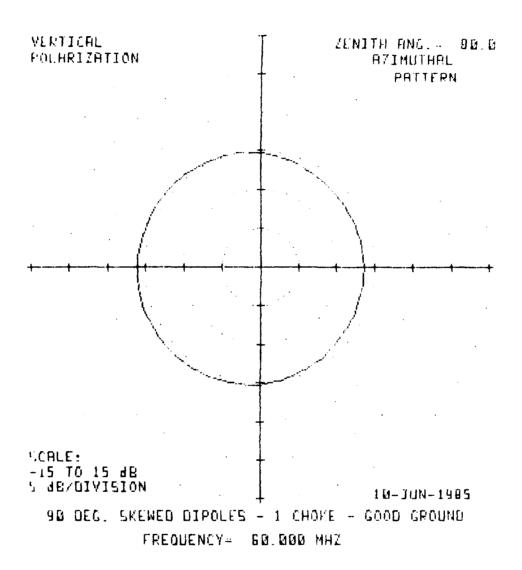


Fig. 5. Calculated pattern of crossed half wave dipoles over ground -  $60~\mathrm{MHz}$ 

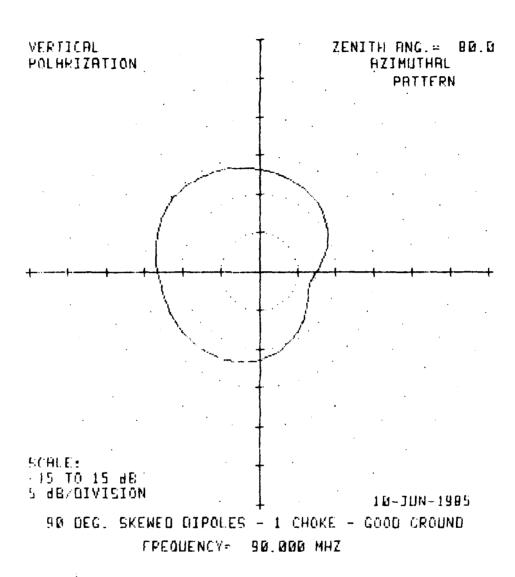


Fig. 6. Calculated pattern of crossed half wave dipoles over ground - 90 MHz

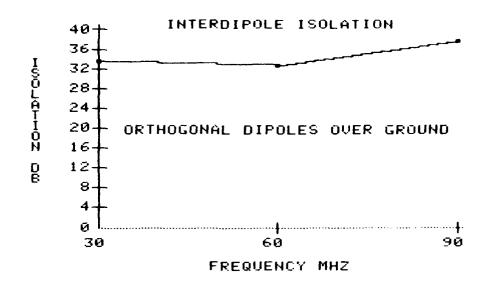


Fig. 7. Calculated isolation between crossed half wave dipoles over ground

Orthogonal Biconical Antennas

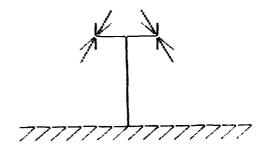


Fig. 8. Crossed biconical antennas over ground

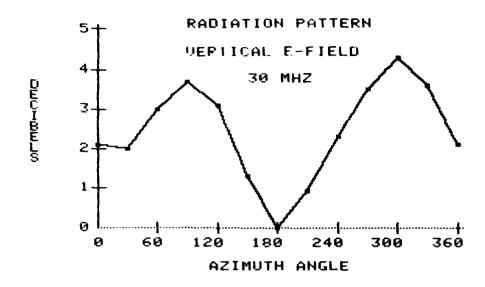


Fig. 9. Measured pattern of crossed biconical antennas over ground - 30 MHz

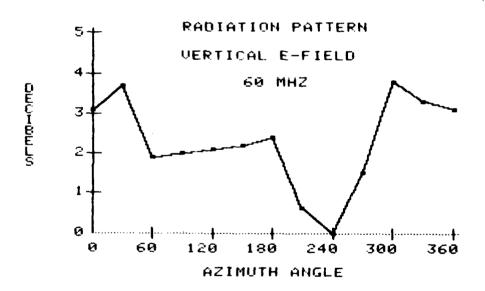


Fig. 10. Measured pattern of crossed biconical antennas over ground - 60 MHz

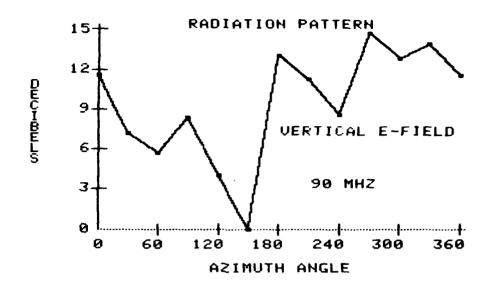


Fig. 11. Measured pattern of crossed biconical antennas over ground - 90 MHz

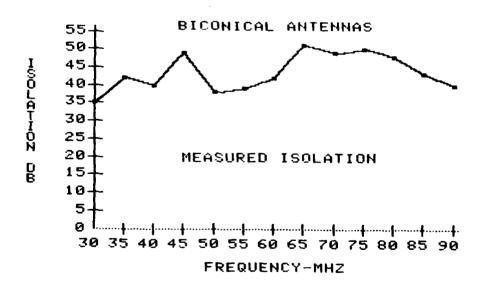


Fig. 12. Measured isolation between crossed biconical antennas over ground

STATES SECTIONS SECTION SECTION STATES

# K & S BAND FEED SYSTEM FOR AN 18-METER HIGH-EFFICIENCY CASSEGRAIN ANTENNA.

B.X. Nguyen, R. Rudolph, G.H. Schennum, and C.H. Tsao

Ford Aerospace & Communications Corporation

Western Development Laboratories

Palo Alto, California 94303

#### ABSTRACT

This paper describes the design and performance of a dual frequency band (K & S) feed system for an 18-meter high-efficiency Cassegrain antenna. The feed system consists of an S-band circular polarized feed with a TE21 tracking coupler, a frequency selective surface, and a K-band circular polarized feed employing TE01 and TM01 tracking couplers. The frequency selective surface (FSS), consisting of four layers of metallic cross dipoles on a flat dielectric substrate, is tranparent at S-band, reflective at K-band, and capable of handling 20 Kw Cw power at S-band with a power safety factor of 5.7. The use of a novel K-band feed system containing an offset ellip- soid subreflector and the FSS provides identical amplitude and phase tapers across the Cassegrain subreflector over both K and S frequency bands with minimum distortion to

the S-band performance, and minimum feed system blockage.

The whole dual frequency feed system is installed on an integrated supporting structure which is easily attached to the main reflector vertex.

The paper discusses the function of each feed system component, the feed system design, and presents results showing good agreement between predicted and measured data for the feed system.

## 1.0 Introduction

Many existing large reflector antennas have been designed with dual shaped reflectors (both main and subreflector are shaped) for high antenna efficiency. However, for those antennas operating with two widely separated frequency bands, it is very difficult to achieve high efficiency over both frequency bands; therefore, they have been designed to have high efficiency in one frequency band only. It is often desirable to up grade these antennas for high efficiency in both frequency bands.

Ford Aerospace and Communications Corporation (FACC) has successfully designed a K- and S-band feed system to achieve these objectives over both frequency bands for an 18-meter shaped surface Cassegrain antenna. The feed system, as shown in Figure 1, consists of an S-band circular polarized feed with a TE21 tracking coupler, a frequency selective surface (FSS), and a K-band circular polarized feed employing TE01 and TM01 trackings couplers. The frequency selective surface, consisting of four layers of metallic cross dipoles on a flat dielectric substrate, is transparent at S-Band, reflective at K-band, and capable of handling 20 KW CW power at S-band with a power safety factor of 5.7. The use of a novel K-band feed system containing an offset ellipsoid and the FSS allows the same amplitude and phase tapers across the Cassegrain subreflector surface over

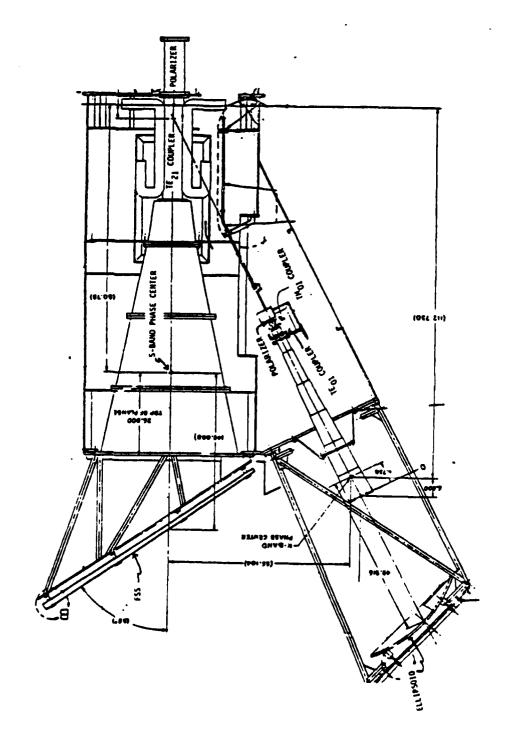


Figure 1. K- & S-Band Feed System Assembly.

both K and S frequency bands with minimum distortion to the S-band performance, and minimum feed system blockage.

This paper discusses the function of each feed system component, the feed system design, and presents results showing good agreement between predicted and measured data for this dual frequency feed system.

#### 2.0 K & S Feed System Components

FACC's K- and S-band feed system has a separated feed system for each frequency band. The S-band feed system uses a corrugated horn to illuminate the Cassegrain subreflector surface with a 15 dB amplitude taper over the desired S-band frequency band. The first ten groves of the horn were varied in depth to smooth the transition from the horn to the circular waveguide of the TE21 tracking coupler which is a scaled model of the Ku-TE21 coupler designed by Choung and Goudey[1]. As shown in Figure 2, this coupler has eight coupling arms for sensing two orthogonal TE21 modes by properly combining the outputs. Between the TE21 coupler and the diplexer is an S-band circular polarizer having 12 fins with Chebyshev distribution to convert a linear polarized wave into a circular polarized wave. To provide the desired subreflector illumination in the offset reflector geometry, the K-band feed system employs a low phase error corrugated horn.

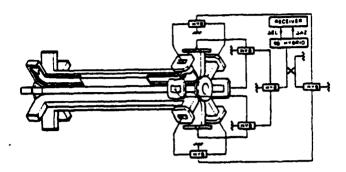


Figure 2. Layout of TE<sub>21</sub> Mode Coupler.

The horn has its far field phase center within two inches of the aperture, and a near field amplitude pattern exhibiting a 15 dB taper at the angle of 10 degrees off axis with its phase center about 6 inches from the aperture. The horn is matched to the circular waveguide, leading to the circular polarizer similar to the S-band polarizer, by a ring loaded corrugated waveguide which has four resonant axially oriented slots for TEO1 mode coupling. The circular waveguide section caries two transverse slots for TMO1 mode coupling. By maintaining proper phase between the TEO1 and TMO1 modes, the tracking system can be sensitive to circular or linearly polarized signals. This type of tracking coupler is inherently narrow band (about 1%).

With the use of an offset reflector, and a frequency selective surface, the K-band feed patterns are imaged to the phase center of the S-band feed patterns.

# 3.0 Frequency Selective Surface

This section briefly discusses the design and performance of the FSS used in the dual frequency feed system shown in Figure 1. A full detail on the theory and design of this FSS will be given in a future paper [4]. As shown in Figure 3, the angle in incidence varies from 20° to 50° across the FSS surface. Based on FACC's experience with the FSS for the MJS' 77 (Voyager) program, and the availability of a computer program analyzing the cross dipole performance, the cross dipole configuration was selected as the baseline resonating element for this FSS design.

From the empirical data and analysis, it was determined that a four-layer FSS will meet the K and S-Band requirements with adequate margin in gain loss and bandwidth. In addition, this design is capable of operating at incident angles up to 60 degrees. The dipole configuration and FSS construction detail are shown in Figures 4 and 5, respectively. The spacing between the second and third FSS layers are tapered linearly in one plane by tapering the center nomex honeycomb core such that the spacing varies from 0.92 inches to 1.34 inches as the angle of incidence varies from 20 to 50 degrees across the FSS surface as shown in Figure 6. This center nomex core also has a large hole (approximately 2-foot) hole in it in order to minimize the heat generated by the film adhesive at S-band radiated power. Cross dipoles need not extend much beyond the 34-inch diameter center of reflection of the FSS.

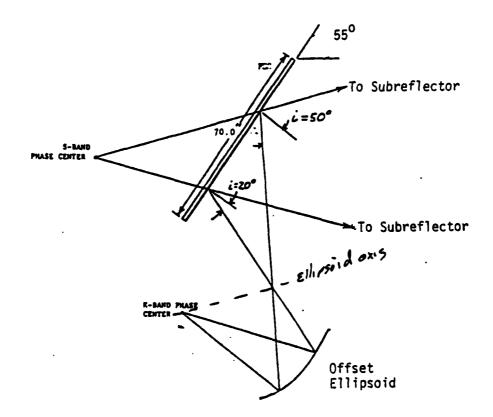


Figure 3. K- & S-Band Feed System Geometry.

THE STATE OF THE PROPERTY OF T

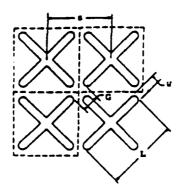


Figure 4. FSS Dipole Configuration.

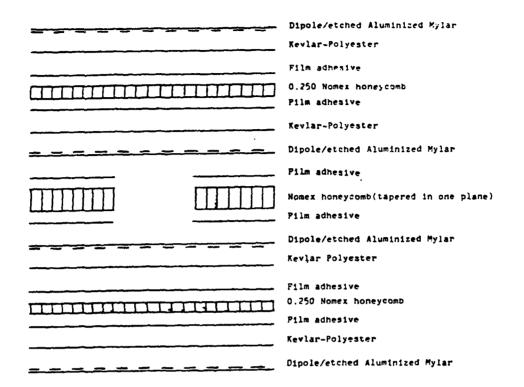


Figure 5. FSS Construction Detail.

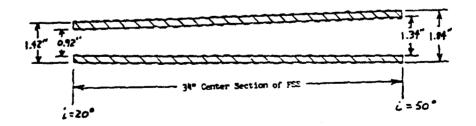


Figure 6. FSS Optimized Taper for S-Band Matching.

# 3.1 K-Band Reflectivity

terrors of secretarist betreated assessed separation

A 13" x 13" four-layer FSS test sample with a 1.5 inch nomex center core with the construction detail shown in Figure 5 was tested for performance. The transmissivity was measured from 12.0 to 16.0 GHz using the test setup sketched in Figure 7. The transmitted power to the receive horn is referenced to the response with the FSS removed. The measured responses are shown in Figures 8 to 11 for incidence angles of 30 and 60 degrees for the E-plane and H-planes. Since the insertion loss of the FSS is theoretically negligible, the reflection loss can be calculated from the relationship  $P_R = 1-P_T$ , where  $P_T$  is the absolute transmitted power and PR is the absolute receive power. Transmissivity data shows that the maximum transmission is greater than 20 dB down from the reference for all incidence angles and all frequencies within the operating band. A 20 dB level indicates a reflection loss of less than 0.05 dB. The theoretical response of the four-layer test sample for the H-plane and E-plane are given in Figures 12 and 13, respectively, over the frequency range of 11 to 17 GHz. Unfortunately, the test equipment setup was unable to record data beyond a 12 to 16 GHz band, so that a comparison of measurement and theory at the band edges could not be made. The theory used is termed a periodic moment method in the literature, and consists of a plane wave expansion in

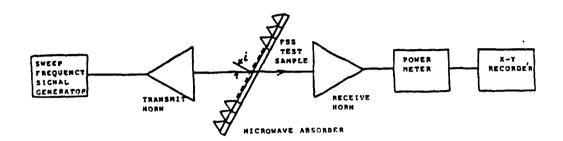


Figure 7. PSS Transmissivity Test Set-Up.

conjunction with mode matching at the dipole interfaces. This method yielded excellent correlation over a broad band of frequencies when compared to the single layer Voyager data. A typical response plot showing this correlation is given in Figure 14. This comparison was made of a test sample in a waveguide simulator so that the angle of incidence varies from 28 to 48 degrees across the frequency band (sin  $i = \lambda/2A$ ) as indicated in the figure. This excellent correlation gives a high credibility to the multiple layer predictions.

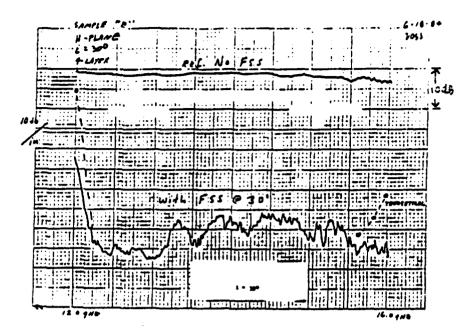


Figure 8. Measured H-Plane Response of 4-Layer FSS.

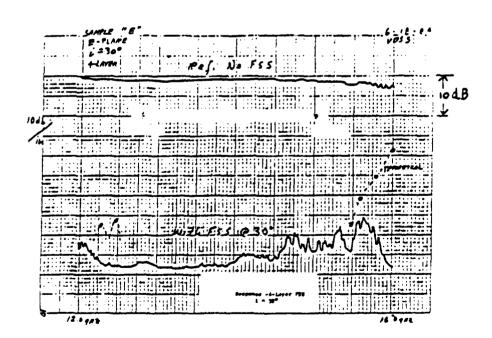


Figure 9. Measured E-Plane Response of 4-Layer FSS.

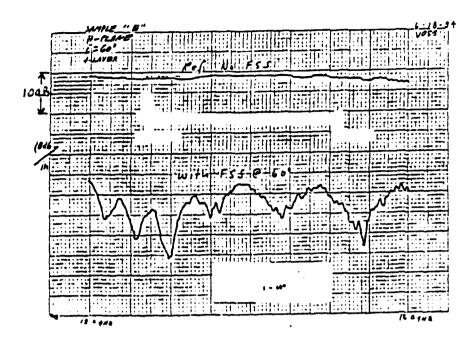


Figure 10. Measured H-Plane Response of 4-Layer FSS with i=60°.

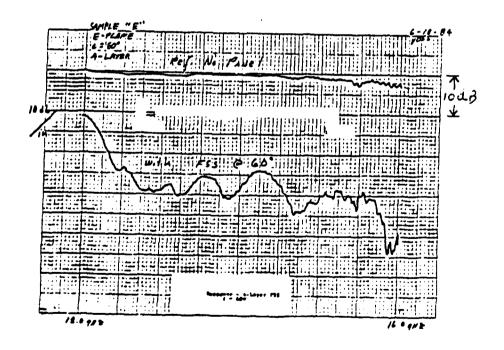


Figure 11. Measured E-Plane Response of 4-Layer FSS. with  $i=60^{\circ}$ .

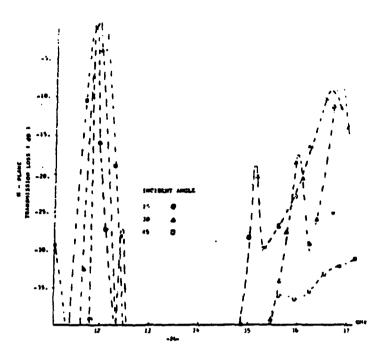


Figure 12. Calculated 4-Layer H-Plane Response

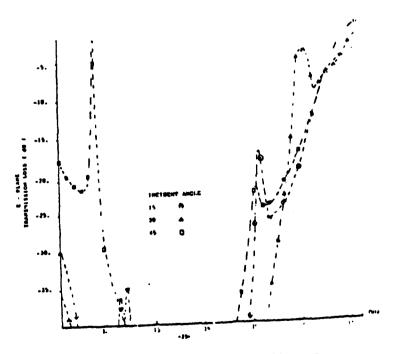


Figure 13. Calculated 4-Layer E-Plane Response.

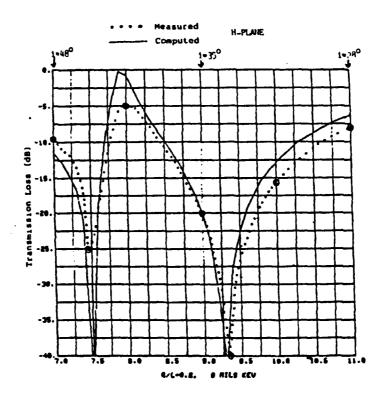


Figure 14. Comparision of Measurement versus Theory for Single Layer FSS.

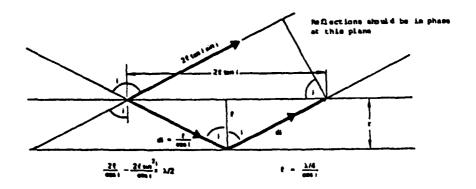


Figure 15. Derivation of Approximate Spacing for a 2-Layer FSS.

#### 3.2 S-Band Transmissivity

In order to minimize the FSS loss at S-Band, a matching layer was added to the 2-layer K-Band design so that the FSS configuration will total four layers. The matching technique is illustrated in Figure 15 for a 2-layer FSS. This analysis is an approximation as it ignores multiple reflections, but it does show the principles involved. The important result is that the spacing should vary inversely with the angle of incidence. For mechanical simplicity it was decided to use a linear taper in one plane to match at S-Band as previously shown in Figure 6. The calculated performance for the selected spacing is shown in Figure 16. The performance was rigorously calculated using the same method as for the K-Band analysis, and the optimization of spacing was obtained by iteration. The calculated transmission loss of the four-layer FSS over the S-Band are shown in Figure 16 for E and H planes. The 13" x 13" 4-layer test sample described in Section 3.1 was measured for S-Band performance and compared to theory. The reflectivity was measured at 1.7 GHz, 2.0 GHz and 2.3 GHz for an angle of incidence of 300 using the test setup sketched in Figure 17. The reflected power to the receive horn was referenced to the response of a metal plate of the same shape and area as the FSS. The measured results are given in Table It should be noted that the purpose of this test was to correlate measurement with theory. The test sample spacing was

1.5 inches between layers two (2) and three (3) which is optimum for an incidence angle of 50°. The test chamber in which the measurements were made restricted data taking to a maximum single of incidence of 30° because of the chamber size. The accuracy of the measurements given in Table 1 is limited by the coupling between the horns which was measured to be 18 dB or an error of 0.07 dB in transmission loss. The correlation between measurement and theory is considered good based on the results and measurement error.

## 3.3 S-Band Power Handling

The power density based on a near-field calculation at the FSS surface is shown plotted in Figure 18. The calculation assumed a transmit power of 20 KW degraded by a loss of 0.56 dB to include the loss between the transmitter and feed. The maximum power density, as shown in the figure, is about 42 watts/in<sup>2</sup> and occurs between 3 and 4 degrees off the z-axis.

The power loss at the FSS surface is given by the relationship:

$$P \alpha \text{ ft } \tan \delta \sqrt{\epsilon_r} E^2$$
 (1)

Where f = frequency

t = dielectric thickness

 $tan\delta = loss tangent of dielectric$ 

fr = effective dielectric constant

E = magnitude of the electric field

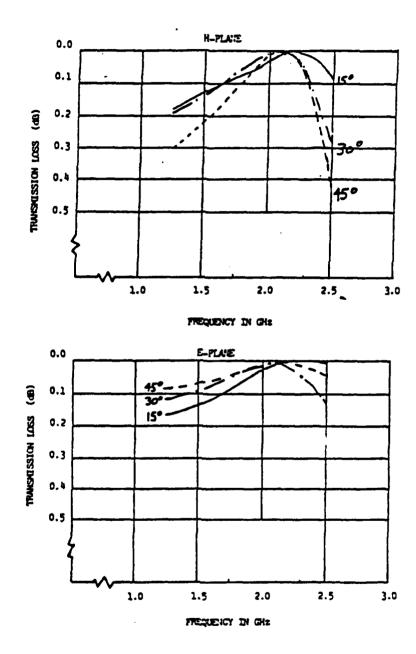


Figure 16. S-Band Calculated Loss.

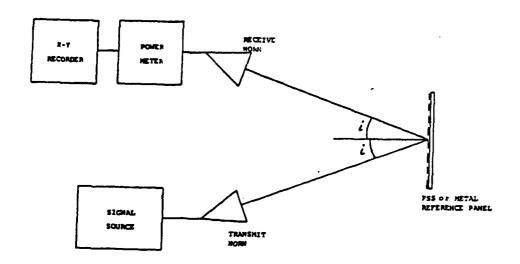


Figure 17. FSS Reflectivity Test Set-Up.

Table 1. Measurements of Four-Layer Test Sample at  $i = 30^{\circ}$ .

Trequency (GHz)	Calculated Transmission Loss(dB)		Measured Transmission Loss(dB)	
	H-Plane	E-Plane	H-Plane	E-Plane
1.7 *	.01	.01	.04	.02
2.0	.12	.03	.11	.11
2.3	. 35	. 30	. 37	.21

From equation (1), it can be seen that the dielectric properties of the materials nearest the peak electric fields primarily determine the power handling of the FSS. The test results and analysis indicate that the electric fields are very concentrated at the tips of the cross dipoles; therefore, the dielectric materials near the dipoles should be carefully selected. The test sample based on this design and previously tested for reflectivity and transmissivity (see Figure 5) was power tested using the test set-up sketched in Figure 19.

It can be shown that the maximum power density inside a waveguide is given by the expression:

$$P_{d} = 2P_{t} / (ab) \tag{2}$$

Where Pt = maximum power density which occurs at a/2

Pt = transmit power

a = waveguide "a" dimension

b = waveguide "b" dimension

For the test set-up of WR 430 waveguide

$$(a = 4.3 inches, b = 2.15 inches)$$

$$P_{d} = 0.216 P_{t}$$
 (3)

The insertion loss between the directional coupler and the point at which the FSS was suspended (0.5 inches from waveguide aperture) was calculated to be 0.33 dB. The relationship between the power density at the FSS test sample and the power density at the plane of the test coupler is then given by

$$P_{d} = .20 P_{tm}$$
 (4)

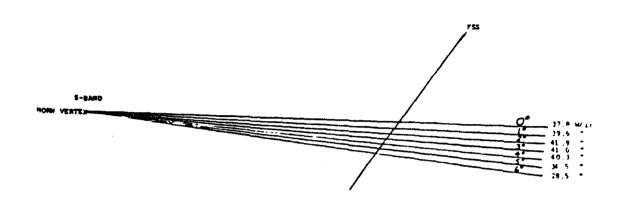


Figure 18. Power Density Distribution Along PSS Surface.

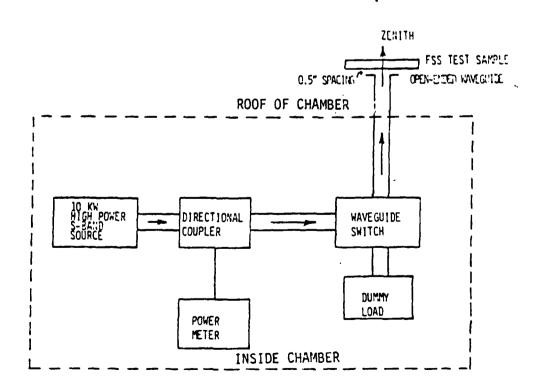


Figure 19. High Power Test Set-Up.

Where Ptm = transmit power at measuring plane of test coupler.

The test results performed on the final four-layer test sample are summarized in Table 2. The results show that the test sample passed with a margin of + 7.6 dB over rated power in the region without nomex core between layers 2 and 3. The sample was not warm to the touch at the conclusion of the test so the margin is probably significantly more than the test margin of + 7.6 dB or a power safety factor of 5.7. The failure at +6.3 dB occurred at the epoxy bond line which bonded layer 2 to the nomex center core in the outer region of the test sample. The epoxy in this region is only separated from the cross dipoles by the 2 mill mylar to which the dipoles are bonded. As the result of this power test, the center nomex core of the final FSS panel will have a large 2-foot hole around the highest power density area to increase the power handling capability.

#### 3.4 FSS Depolarization Effects

CALL DESCRIPTION OF THE PROPERTY OF THE PROPER

The axial ratios of the S-band horn alone, and those of the FSS/S-Band horn combination were measured with a linear rotating source technique. Based on these results, the axial ratios of the FSS were computed at both K and S frequency bands. The results are shown in Table 3. As shown in this table, these predicted axial ratios are in good agreement with

those computed from the reflection and transmission coefficients generated by FACC's computer program.

Table 2. FSS High Power Test Results on 4-Layer Test Sample at 1.8 Ghz.

Region on Test Sample	Power Density	Test Duration	Safety Factor(dB)	Comment s
Corner of Sample. Nomex Core bonded between layers 2 and 3.	120 watts/in <sup>2</sup>	90 minutes	+ 4.6	Sample passed.
Corner of Sample. Normex Core bonded between layers 2 and 3.	180 watts/in <sup>2</sup>	120 minutes	+ 6.3	Sample (ailed. Core disection showed charring of the epoxy which bonds layer 2 and Honex core.
Center of Sample. No Nomex Core in this region.	180 watts/in <sup>2</sup>	120 minutes	+ 6.3	Sample passed. Core disection showed no internal failures.
Center of Sample. No Nomex Core in this region.	240 watts/in <sup>2</sup>	120 minutes	+ 7.6 d5	Sample passed. Layers 3 and 4 previously re- moved allowed look at layer 2. Dample did not even feel warm immediately after test.

Table 3. Tabulated Axial Ratios.

Frequency	(I) Axial Ratio of Feed	Axial Ratio of Feed & FSS	(3) Axial Ratio of FSS (Based on (1) & (2))	(4) Axial Ratio of FSS (Computer Results)	(5) Percentage Difference
1800 MHz	1.091 (or 0.75 dB)	1.223 (or 1.75 dB)	1.191 (ar 1.52 dB)	1.146 (or 1.18 dB)	+3.8%
2200 MHz	1.103 (or 0.85 d8)	1.349 (or 2.6 dB)	1.219 (or 1.72 dB)	1.247 (or 1.91 dB)	+2.3%
13.0 GHz		1.023 (or 0.2 d8)		}	
15.0 GHz		1.274 (or 2.1 dB)			

<sup>(1)</sup> Measured data without the FSS.

<sup>(2)</sup> Measured data with the FSS.

<sup>(3)</sup> Computed data based on (1) and (2).

<sup>(4)</sup> Computed data from computer program.

<sup>(5)</sup> Percentage Difference = Voltage Ratio in (4) - Voltage Ratio in (3)

#### 4.0 K- & S-BAND FEED SYSTEM DESIGN

The system design has been constrained by a requirement to use an existing main reflector and its supporting structure; therefore, the following design procedure is served as a guided line.

- \* Design a shaped subreflector surface such that the current main reflector surface can be reused.
- \* Design an S-band feed horn such that its patterns are approximately within ±4dB of the ideal surface shaping feed pattern (Gaussian) at 150 off axis.
- \* Design a K-band feed system employing an offset reflector and an FSS to produce the same amplitude taper over the Cassegrain reflector surface as that of the S-band.
- \* Design an FSS which is transparent at S-band, reflective at K-band, and capable of handling 20 KW CW power. (The design of the FSS was presented in Section 3.0).

## 4.1 High-efficiency Cassegrain antenna

By using a special computer program, FACC was able to design the new geometry of the 18-meter high-efficiency antenna with the main reflector surface shape almost identical to the existing one; therefore, the current main reflector and its supporting structure can be reused.

With the new antenna geometry, as shown in Figure 20, a Gaussian feed pattern with 15 dB amplitude taper at 15 degrees will produce an uniform amplitude distribution over the main reflector aperture plane.

## 4.2 K- & S-band feed system geometry

The S-band feed system geometry is the same as that of a conventional high-efficiency Cassegrain antenna; therefore the design of the S-band feed system involves only the design of an S-band horn which produces the near field patterns aproximate to the ideal pattern in Section 4.1 at a distance equal to that between the feed pattern phase center and the Cassegrain subreflector vertex. Using the techniques described by Thomas, and James [2],[3] an S-band corrugated horn was designed, and its near field patterns were computed. A typical S-band amplitude pattern, as shown in Figure 21, exhibits a taper of 12 dB at the angle of 15° off axis.

The design of the K-band feed system is much more involved since it employs an offset reflector and an FSS as the mirrors to produce patterns at the same location and the same beamwidth as those of the S-band. In order to maximize the K-band efficiency, minimize the distortion to the S-band performance, and minimize the total feed system blockage, the following design criteria were employed.

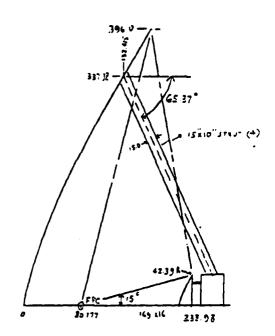


Figure 20. 18-Meter High-Efficiency Cassegrain Antenna.

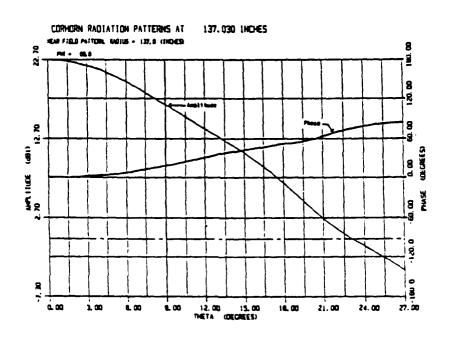
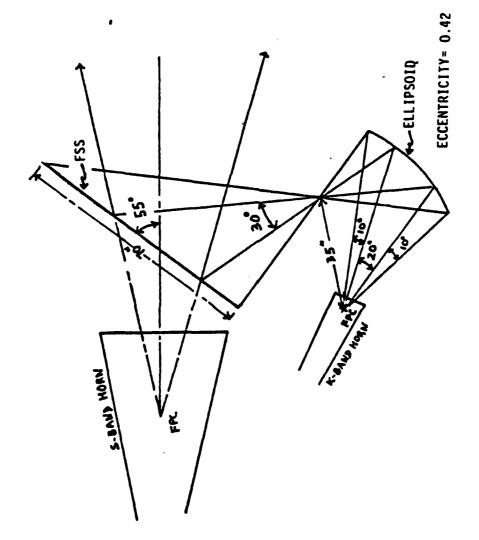


Figure 21. S-Band Feed Patterns.

- a. The offset reflector aperture must be at least 20 wavelengths to capture adequately the K-band horn radiated energy.
- b. The K-band feed system structure must be kept clear from the cone angle of 30 degrees with its vertex at the S-band phase center.
- c. The K-band feed system structure must produce minimal shadow on the main reflector aperture plane.
- d. The K-band feed system structure must be mounted along the shadow of one of the supporting struts.

The design of the K-band feed system was based on ray optics and physical optics. First, a ray tracing computer program was exercised to find a feed system geometry which could transform a 10 degrees beamwidth of the K-band horn pattern to a 30 degrees beamwidth at the S-band feed pattern location. The results of the analysis indicates that an offset hyperboloid is not a viable candidate because the feed system geometry violates the design criteria b and c. The results also shows that an offset ellipsoid is a very potential candidate, and a good combination of a position of the FSS and the eccentricity of the ellipsoid produces a minimal shadow on the main reflector aperture plane. The final geometry is shown in Figure 22. Based on this geometry and the near field patterns of the K-band horn, a special computer program developed at FACC was exercised to compute the pattern

CAMPAGAMENT CONTRACTOR DESCRIPTION OF THE PROPERTY OF THE PROP



decesses, respectes decesses applicated represent represent represent represent respects from the property of the second second

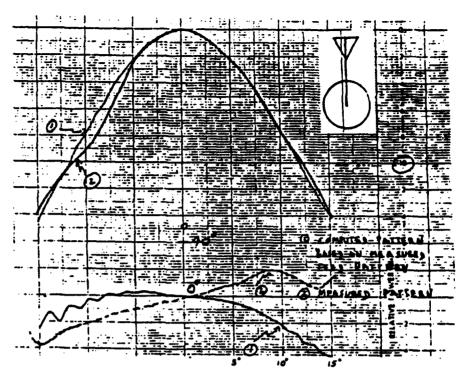
Figure 22. Final K- & S-Band Feed System Geometry.

reflected from the FSS. The computer program uses the physical optics to compute the patterns of a reflector immersed in the near field of a radiating source. The computed patterns at 15 GHz, shown in Figures 23-24, are very close to those discussed in Sectio 4.1.

# 4.3 K- & S-band feed system performance

The K- and S-band feed system was built, and their patterns were measured at FACC antenna test range in Palo Alto, California. The typical results at K- and S-band are shown in Figures 23-25. As shown in these figures, these results are in good agreement with the predicted results. Figure 26 shows an S-band feed pattern in the asymmetrical plane measured to ±180 degrees. It shows an abnormal high side lobe at 100 degrees off axis which was caused by the reflection from the FSS. Since FACC computer modeling treats the FSS as a completely transparent surface at S-band, we could not predict this sidelobe; however, our antenna wide angle sidelobe pattern computed with this feed pattern (see Figure 27) does not shown a serious degradation to the antenna system sidelobe performance.

STATES OF THE STATES STATES STATES ( SANSSES )



Pigure 23. K-Band Feed Patterns in the Symmetrical Plane.

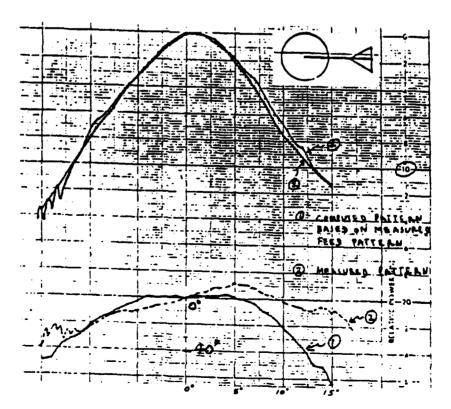
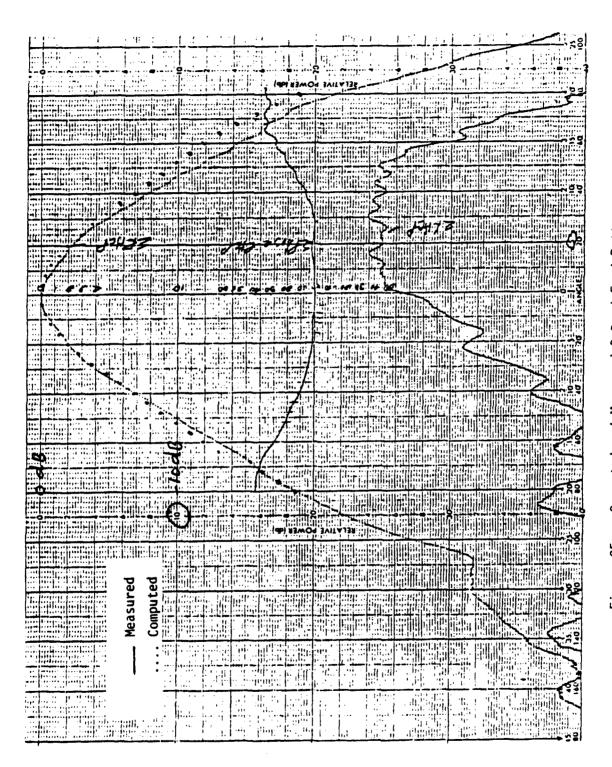


Figure 24. K-Band Feed Patterns in the Asymmetrical Plane.



igure 25. Computed and Measured S-Band Feed Pattern.

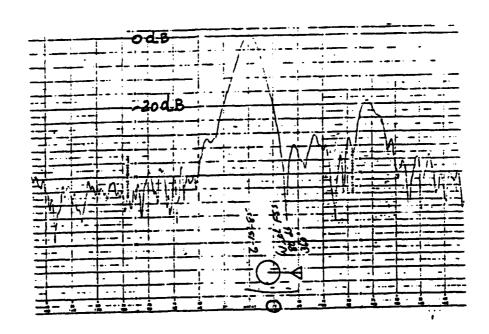


Figure 26. Wide-Angle Feed Patterns with FSS at S-Band.

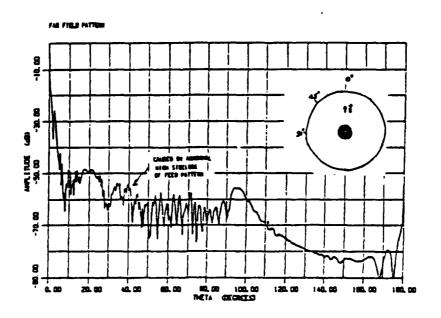


Figure 27. Antenna Wide-Angle Sidelobes at S-Band.

## 5.0 CONCLUSION

greed betifical essents. Eccesses research estimates estimated

FACC has successfully designed and manufactured a K- and S-band feed system which enables an 18-meter high-efficiency Cassegrain antenna to have high antenna efficiency over both frequency bands. The feed system employs an offset ellipsoid and an FSS to achieve the same amplitude and phase tapers across the Cassegrain subreflector. The FSS is transparent at S-band, reflective at K-band, and capable of handling 20 KW CW power with a power safety factor of 5.7. The whole feed system assembly is installed on an integrated supported structure which can be easily mounted to the main reflector vertex. Although the design presented in this paper is for an K- and S-band 18-meter high-efficiency Cassegrain antenna, the design approach can be used to design the dual frequency band feed system of any reflector antennas.

## 6.0 References

- 1. Choung, Y.H, K.R. Goudey, and L.G. Bryans, "Theory and Design of a Ku-Band TE<sub>21</sub> -Mode Coupler," <u>IEEE</u>

  <u>Trans. on AP</u>, Vol. AP-30, No. 11, Nov. 1982, pp. 1862-1868.
- 2. Thomas, B.M, "Design of Corrugated Conical Horns,"

  IEEE Trans. on AP, Vol. AP-26, No. 2, Macrh 1978, pp.

  1068-1072.
- 3. James, G.L, "TE<sub>11</sub>-to-HE<sub>11</sub> Mode Converters for Small Angle Corrugated Horns," <u>IEEE Trans. on AP</u>, Vol. AP-30, No. 6, Nov. 1982, PP. 1057-1062.
- 4. Hwang, Y.M., G.H. Schennum, and C.H. Tsao, "A Frequency Selective Surface for High Power Dual Band Ground Terminal Antenna Applications," to be presented at IEEE AP-S and URSI Symposium, June 9-13, 1986, Philadelphia, Pennsylvania.

## LOW-LOSS SYMMETRIC OFF-AXIS FLEDS FOR SYMMETRIC DUAL-REFLECTOR ANTENNAS

T. Veruttipong, V. Galindo-Israel, W. Imbriale

Jet Propulsion Laboratory California Institute of Technology Pasadena, California

#### **ABSTRACT**

Circularly symmetric dual-reflector high-gain antenna systems often require feeds placed off the system's axis because of the need for multiple feeds to use the reflector antenna. Also, the constraint requiring the hyperboloid or shaped subreflector to remain circularly symmetric is sometimes added. In a Cassegrain system, the subreflector and feed may be rotated off axis around the paraboloid focus and retain main reflector focusing. However, substantial spillover results in considerable noise in a high gain/noise temperature system. In a shaped system, rotation of the shaped subreflector and feed together results in substantial defocusing as well as spillover noise. If the subreflector is rotated approximately one-half the angle of the feed rotation in either the Cassegrain or the dual-shaped reflector antenna, it is found that spillover and noise are substantially reduced with tolerable defocusing. An extensive numerical analysis of these effects was conducted to determine the characteristics of a planned 70-meter dual-shaped versus

Service Description (Colored Description Service) (Service)

Cassegrain antenna and to determine some understanding of the cause of the observed effects.

### 1. INTRODUCTION

In large ground antenna systems, it is often necessary to use multiple feeds for the same main reflector. Thus, a number of feeds can be rotated off the axis of the symmetric main reflector, each illuminating a rotated subreflector, often the same subreflector that is rotated into position for a given feed. This type of antenna system is shown in Figures 1a and 1b.

In some systems, such as the Jet Propulsion Laboratory (JPL) 70-meter upgrade of the 64-meter antenna, the subreflector can be more than 200 wavelengths at 8.45 GHz. There is a considerable cost savings possible if a circular symmetric subreflector is used in place of an asymmetric offset subreflector. This is especially true for shaped reflectors 1,2,3 that have no parent circular symmetric reflector from which they could be cut. The circularly symmetric subreflector can also be useful for feeds located on the axis of the symmetric main reflector. This would result in "best" or "reference" performance, given the ability to "retilt" the otherwised tilted subreflector.

In the study of the off-axis feed antenna system, the tilt angle of the feed relative to the tilt angle of the subreflector

was varied; the absolute angle of the tilt was also varied. These tilt angles for the feed ( $\alpha$ ) and for the subreflector ( $\beta$ ) are shown in Figure 2.

The actual point of rotation of the feed and subreflector depends upon the type of reflector design used. For a Cassegrain (parabola/hyperbola) system, the obvious choice for a rotation point is the paraboloid focus. For a dual-shaped reflector system, the choice is not obvious. The "optimum" choice for the shaped reflectors is discussed later.

In either case, when large (in wavelengths) reflectors are used, the off-axis displacements of the feeds may be many tens of wavelengths. Consideration will be given to the characteristics of a 70-meter dual-reflector antenna that is an upgrade of a National Aeronautics and Space Administration/Deep Space Network (NASA/DSN) 64-meter design with off-axis feeds (see Figure 2).

### 2. GAIN RESULTS VERSUS OFF-AXIS ROTATION

LOS PROPOSOS, ARRIGIOS PERSONAS POPOSAS ERROPANIOS PALABORAS DELEGOS POPOSOS ERROPARIOS ERROPAS ERROPAS

There are two types of off-axis rotations of the feed and subreflector. In one case,  $\beta=\alpha$ : that is, the subreflector and feed are rotated by the same angle. For the Cassegrain system, note that, in this case, the phase on the main reflector remains correct except where the main reflector becomes underilluminated.

In a second case,  $\beta=\alpha/2$ . For this choice of  $\beta$ , we find that the main reflector remains neither under- nor overilluminated. However, it is clear that a phase error is introduced for the Cassegrain system. The significance of the proper amplitude illumination of the main reflector is that spillover past the main reflector results in a large receiving noise from a relatively hot Earth behind the main reflector. In the case when  $\beta=\alpha/2$ , the feed is always pointed toward the center of the subreflector.

As a function of  $\alpha$ , the Cassegrain system maintains a better gain curve than the shaped reflector antenna for  $\beta = \alpha$  (except for noise considerations). The dual-shaped reflector system maintains a significantly better gain curve than the Cassegrain for  $\beta = \alpha/2$  (providing an optimum rotation point is chosen).

The gain versus  $\alpha$ -angle curves for the 70-meter designs are shown in Figure 3 for the Cassegrain and in Figure 4 for the dual-shaped reflector systems.

The gain versus  $\alpha$  curve for  $\beta = \alpha$  in Figure 3 is relatively flat, although the noise temperature increases with  $\alpha$ . The principal cause of a loss in gain is reduced illumination on one side of the main reflector (discussed in detail later). This reduction could be eliminated by choices of an offset asymmetric hyperboloid. However, the offset asymmetric subreflector can be

used for only one  $\alpha$  angle and is more costly. The  $\beta=\alpha/2$  gain curve for the Cassegrain antenna drops off rapidly with increasing  $\alpha$  because of an increasing aperture phase error. In this case, however, the illumination amplitude across the main reflector aperture has considerably less spillover and, therefore, there is considerably less noise collected. Note also that for the  $\beta=\alpha$  case, there is no beam-pointing shift. The beam points in the  $\theta=0$  direction for all  $\alpha$ . For the case with  $\beta=\alpha/2$ , there is an approximately linear shift of beam-pointing direction as indicated in Figure 3.

The geometry and dimensions for the Cassegrain system under study are shown in Figure 5. An experimental corrugated horn feed was used for the dual-shaped reflector antenna geometry shown in Figure 6. The overall dimensions of the two antenna systems were kept approximately the same. The Cassegrain subreflector was illuminated with a -10 dB taper at the edge of the subreflector.

The dual-shaped subreflector was illuminated with a -16 dB taper at the edge of the subreflector. The dual shaping was chosen for a maximum gain. There was a small taper allowed near the edge of the main reflector. A slight extension of the main reflector beyond the geometric optics edge was introduced to reduce the noise temperature increase that normally comes from the tapering edge of the subreflector scattered pattern. The

subreflector was synthesized with a vertex plate blended into the synthesis.  $^{\mathbf{l}}$ 

The gain versus  $\alpha$  results for the dual-shaped reflector is shown in Figure 4. For  $\alpha=0$ , the gain of the dual-shaped reflector is about 0.75 dB higher than for the Cassegrain system. The relative aperture efficiencies (spillover and depolarization accounted for) are 80.5% for the Cassegrain and 96.5% for the dual-shaped system (in both cases for  $\alpha=0^{\circ}$ ).

The actual frequency for these computations was 8.45 GHz. The radius of the main reflector was taken as 986.3 wavelengths. The computations were greatly facilitated by the use of a GTD analysis of a subreflector and a Jacobi-Bessel<sup>4,5,6</sup> analysis of the main reflector scattered field. Various global and local interpolation methods were employed to analyze the shaped subreflector and main reflector.

The gain versus  $\alpha$  angle results for the dual-shaped antenna (see Figure 4) show that the performance for the case  $\beta = \alpha$  degrades rapidly and badly because of the introduction of both a phase and an amplitude error in the main reflector aperture distribution by the rotation of the feed and sub-reflector as a unit. The degradation in gain caused by the underillumination of amplitude only is greater here than for the Cassegrain antenna because the object illumination function resulting from dual shaping is nearly uniform.

TO SECURE AND ADDRESS OF THE PROPERTY OF THE PASSAGE AND ADDRESS OF THE PAS

When the shaped subreflector is rotated by the angle  $\beta = \alpha/2$  around the appropriate point of rotation, the results in gain versus  $\alpha$  angle are comparable to the Cassegrain gain versus  $\alpha$  angle results for the  $\beta = \alpha$  case. Note that the shaped reflector system has the advantage over the Cassegrain of a lower noise amplitude distribution. Further explanation for this result will follow in the next section.

A relevant question at this point is: Why is  $\beta = \alpha/2$  an "optimum" value of  $\beta$  as opposed to some other fractional portion of  $\alpha$ ? It does turn out that  $\beta \simeq \alpha/2$ , the amplitude distribution on the main reflector, has a minimum underillumination. In Figures 7 through 9, show the gain of Cassegrain and dual-shaped antennas as a function of the  $\beta$ -angle (rotation angle of the subreflector) with the  $\alpha$ -angle (rotation angle of the feed) fixed.

For the Cassegrain antenna (with  $\alpha$  fixed at  $10.52^{\circ}$ ), note that the gain peaks when  $\beta=\alpha$ . This is expected because the aperture phase is correct at  $\beta=\alpha$ , and the phase is more critical than the amplitude. For the dual-shaped reflectors, the result is quite different. In this case, the gain peaks at approximately  $\beta=\alpha/2$  for both  $\alpha=10.52^{\circ}$  and  $\alpha=4.482^{\circ}$  (see Figures 8 and 9). Again, the phase, as well as the amplitude, is an optimum. As noted later (for the shaped reflectors), the phase function is optimum at approximately

 $\beta$  =  $\alpha/2$  when the "best" rotation point is chosen. This is related to the fact that the field scattered from the subreflector has an extended set of two caustic surfaces as opposed to the single caustic point for the Cassegrain antenna. These caustic surfaces are discussed later.

All the preceding results were for circularly symmetric subreflectors, shaped and conic. For the case  $\beta = \alpha/2$ , the Cassegrain system suffers a phase error in the main reflector aperture. For the case  $\beta = \alpha$ , the Cassegrain system suffers an amplitude distortion with subsequent increased receiver noise. Both of these deficiencies can be removed with an asymmetric hyperboloid (in the plane of rotation of the feed and subreflector). Results for comparison with asymmetric hyperboloid subreflector are shown in Table 1. For  $\alpha$  less than about 6°, there is only about 0.1 dB difference between the various cases (see Figure 3), although the asymmetric reflector does give marginally better performance. The  $\beta = \alpha/2$  case does give equivalent results with a less expensive symmetric hyperboloid. Note that when diffraction from the subreflector is ignored, the gain is increased by 0.1 dB, a direct measure of spillover loss for the Cassegrain (usually much higher for electrically smaller antennas).

A final point for consideration in this section is the determination of the point of rotation of the subreflector and

Table 1. Cassegrain Gains (dBi)

Concentric Cassegrain	β	= <b>a</b> = 0°	74.90
Asymmetric Hyperboloid	β	$\alpha = 4.5165^{\circ}$	74.86
Asymmetric Hyperboloid (No Diffraction from Sub)	β	$= \alpha = 4.5165$	74.96
Symmetric Hyperboloid	β	$= \alpha = 4.5165^{\circ}$	74.71
Symmetric Hyperboloid	α	= 4.5165 $(\beta = \frac{\alpha}{2})$	74.82

feed for the dual-shaped reflector system. Because an incoming plane wave reflected from the shaped main reflector will not come to a point virtual focus, the precise optimum point of rotation is not immediately clear. In Figure 10, all rays do intersect along a caustic line behind the subreflector (in the non-rotated position). For a Cassegrain antenna, this line degenerates into a point. Actually, this caustic arises from the curvature out of the plane of the paper. It would seem that an "optimum" point of rotation for the shaped system would lie within the limits of this caustic line.

The position may be weighted along the caustic by plotting the caustic intersection point versus position ( $\rho$ ) along a radius of the main reflector (this is also shown in Figure 10.) For the Cassegrain, all rays intersect at a fixed z position: the focus. For the shaped system, different radial positions

along the main reflector correspond to different positions of intersection along the z-axis. Because the main reflector aperture distribution is nearly uniform, an accordingly weighted mean z position may be chosen as an optimum point of rotation.

A more direct method of choosing the optimum point is observed in Figure 11. The feed lateral displacement is fixed:  $\Delta X$ . Then, the subreflector is rotated to the position  $\beta = \alpha/2$  with different points, F', of rotation. It is known from experience that  $\beta = \alpha/2$  is an approximately optimum ratio between  $\alpha$  and  $\beta$  for the shaped reflectors. The optimum position, F', of rotation is in the vicinity of the weighted curve of Figure 10.

Figure 10 notes that the main reflector line caustic z-position doubles back on itself near  $\rho$  = 975  $\lambda$ . Thus, there is an additional intersection of rays off the z-axis. This intersection is the caustic from curvature of the field in the plane of the paper.

#### 3. FAR-FIELD PATTERNS AND REFLECTOR CURRENTS

In this section, the far-field patterns of both the Cassegrain and the dual-shaped 70-meter antennas are presented as a function of the  $\alpha$  and  $\beta$  angles (the  $\beta$  =  $\alpha$ , and the  $\beta$  =  $\alpha/2$  cases). The main reflector current distributions will also be reviewed to obtain some insight into the characteristics of

these antennas with  $\alpha$  and  $\beta$  angles of feed and subreflector rotation.

Figure 12 shows the far-field patterns of the 70-meter shaped and Cassegrain systems with  $\alpha = \beta = 0$ , the concentric case. In addition to the vertex plate on the subreflector of the shaped reflectors, the shaped main reflector also has an extension that serves as a noise shield; i.e., it shields the feed from the average 240 K ground noise in that critical area of sharp energy dropoff near the main reflector edge. The shaped system attains about 96.6% efficiency, whereas the Cassegrain system attains about 70.2% efficiency (with a -10 dB feed taper and blockage not accounted for). Spillover and cross-polarization losses are accounted for in these computations.

The pattern degradation of the Cassegrain system with increasing angle  $\alpha$  is not great because the main reflector currents remain properly in phase over most of the reflector, except the underilluminated portion. The degradation is, however, more apparent for the  $\beta=\alpha/2$  case. This is illustrated in the patterns of Figures 13a and 13b. Note that the vertical gain scale is shifted for each pattern; the change in gain between patterns is noted next to each pattern. Of special interest is the actual beam pointing direction for each pattern noted next to the pattern by  $\theta_{\rm R}$ . With a 3-dB beamwidth of

esel berretest recessed bearders appress september 1980see 1980see 1980see

less than  $0.05^{\circ}$ , the beam shift from the concentric  $\alpha = \beta = 0^{\circ}$  case is many beamwidths.

The pattern degradation is very great for the shaped reflectors antenna when  $\alpha = \beta$ . This is clear because even when the subreflector and feed are rotated about an optimum point on the caustic (see Figure 10), there is substantial phase defocusing for the  $\alpha = \beta$  case. However, for the  $\beta = \alpha/2$  case, the defocusing is substantially reduced, and the beam is shifted with considerably less loss in gain and degradation in pattern structure. This is shown in Figures 14a and 14b.

Of special interest in the far field is what occurs to the phase and the amplitude monopulse patterns when the feed and subreflector are rotated so that  $\beta = \alpha/2$ . To observe this effect with the Cassegrain antenna, a "synthetic" feed monopulse pattern was used. This pattern, as well as the sum pattern for the Cassegrain feed, are shown in Figure 15. The effect of the asymmetry for the case with  $\alpha = 4.52^{\circ}$  is shown in Figure 16. Although the "null" of the amplitude pattern is not as deep as for the  $\alpha = 0^{\circ}$  case, and the phase shift of  $180^{\circ}$  at the sum pattern maxima is not as sharp, the monopulse pattern is usable.

Before the currents on the main refrector are investigated, it is of interest to look at the  $\alpha$  =  $0^{\circ}$  concentric scattered fields from the shaped subreflector and the hyperboloid subreflector. These are shown in Figure 17. The patterns are

for the near fields in the vicinity of the main reflectors. It is apparent for such large subreflectors (approximately 200  $\lambda$ ), that the vertex plate is extremely effective. Furthermore, the optical projection approximation accounting for subreflector blockage is also accurate. Also apparent is the relatively precise secant squared behavior (for high gain) achieved by the shaped reflector system.

The current distributions on the main reflectors in the plane of feed and subreflector rotation are shown in Figures 18 through 21. Both amplitude and phase, at the Cassegrain and shaped systems, and at the  $\beta$  =  $\alpha$  and the  $\beta$  =  $\alpha/2$  cases are also shown. The object is to gain some further insight into what is occurring within the reflector systems that causes the result in gains and the far-field patterns that have already been observed.

In Figure 18 shows the paraboloid currents as a function of parameter  $\alpha$  when  $\beta = \alpha$ . (The curves are displaced vertically so that their relative functional characteristics is easily compared.) Note that the phase curves remain flat except where underillumination of the paraboloid occurs (to the left). The underillumination is evident in the amplitude curves. The underillumination to the left is matched by an overillumination to the right. This over illumination increases the noise of the antenna substantially for a ground system antenna looking toward zenith. The overillumination receives the averaged approximately

THE PROPERTY OF THE PROPERTY O

240 K ground radiation, as compared to an overilluminated space antenna which would receive approximately 2.7 K galactic noise. This is one of the principal motivations for using rotation angles  $\beta = \alpha/2$  for the feed and subreflector of a Cassegrain antenna.

When  $\beta = \alpha/2$ , the over- and underillumination of the paraboloid is reduced substantially. This is observed in Figure 19 over a wide range of  $\alpha$  from  $\alpha = 0^{\circ}$  to  $\alpha = 14.52^{\circ}$ . The penalty for this well illuminated paraboloid in amplitude is a phase error illumination, which is also observed in Figure 19. A linear beam-shift phase term has been subtracted from the phase curves so that what is depicted as displaced from a flat curve is a phase error. As observed in Figure 3, the phase error is not significant (relative to the  $\alpha = \beta$  case) until  $\alpha$  is greater than  $6^{\circ}$ .

For the dual-shaped reflectors, the situation is very different. When  $\alpha = \beta$  is maintained and  $\alpha$  is increased, not only does a poorly illuminated main reflector suffer in amplitude, but also in substantial phase error. This is shown in Figure 20. Also, the amplitude over- and underillumination effects are more severe here than for the Cassegrain antenna because the illumination amplitude is nearly uniform or flat. This is a result of the secant squared subreflector scattered pattern (see Figure 17).

As a result, it is fortuitous that rotating the subreflector with  $\beta = \alpha/2$  gives such excellent results for the dual-shaped reflector antenna. The current distributions for this situation as a function of the parameter  $\alpha$  is shown in Figure 21. The phase curves are relatively flat for a large range of  $\alpha$  (after subtraction of the appropriate linear beam shift phase). The resulting gain curve as a function of  $\alpha$  (see Figure 4) is comparable to that obtained for the Cassegrain curve, although higher in value as a result of the shaping.

The main reflector current curves clarify what is occurring to the amplitude distribution on the main reflectors when  $\alpha = \beta$  and when  $\beta = \alpha/2$ . It is clear that when  $\alpha = \beta$ , a large noise temperature can occur for ground system antennas looking upward. It is also clear that setting  $\beta = \alpha/2$  will largely alleviate this problem for both the Cassegrain and the dual-shaped reflector systems.

It is also clear why the main reflector current phase behaves well (nearly flat) for the Cassegrain antenna when  $\beta = \alpha$ . However, an understanding of why the main reflector current phase curves are as flat as they are for  $\beta = \alpha/2$  requires further investigation.

4. CAUSTIC CHARACTERISTICS OF THE SUBREFLECTOR SCATTERED FIELDS Further insight into why the shaped main reflector phase current distributions are as flat as observed for  $\beta = \alpha/2$  (see

Figure 21) can be obtained by studying the caustic surfaces of the geometrical optics fields scattered from the subreflector.

In the plane of rotation of the feed and subreflector, the Gaussian curvature matrix is diagonal (by symmetry), and a line caustic for the radius of curvature out of the plane  $-R_0$  can be observed; another line caustic for the radius of curvature is parallel to the plane  $-R_0$ .

A set of the above line caustics (for different  $\alpha$ ) can be plotted relative to the subreflector and relative to the main reflector. When the caustic lines relative to the main reflector for  $\alpha = 0^{\circ}$  and for  $\alpha > 0^{\circ}$  are plotted, then a relative comparison can be made of how much the  $\alpha > 0^{\circ}$  caustic lines deviate from the ideal  $\alpha = 0^{\circ}$  caustic line. This deviation is a visual measure of the phase distortion that is observed on the main reflector for  $\alpha > 0^{\circ}$ .

For the Cassegrain antenna and  $\alpha = \beta$ , both caustic lines degenerate into a point for all  $\alpha$ . This point is the focal point of the hyperboloid and paraboloid. When  $\beta = \alpha/2$ , caustic lines are obtained as shown in Figure 22. In Figure 22, the caustic lines are plotted relative to the subreflector for all  $\alpha$ . To observe the caustics relative to the main reflector, each caustic must be rotated about the rotation point (focal point) by the value of  $\alpha$ .

ted states become meters absent applies assente

In Figure 23, the same caustic lines are observed in an enlarged diagram. The rays emanating from the caustics are tangent to the caustic surfaces. For the  $R_{\rm O}$  curves, the rays are tangent to a cusp of the surface in the plane of the paper. The rays depicted in the top diagram are all directed toward one end of the main reflector. However, because of the rotation of the feed and subreflector assembly, the main reflector is rotated for each caustic line by  $\alpha$ ; i.e., the curves are plotted relative to the subreflector. (The rays appear parallel, but they are not.) The lower diagram of Figure 23 shows rays distributed to all parts (in the plane) of the main reflector.

The computation and plotting of the caustics are performed during a geometrical optics analysis of the field scattered by the subreflector. In this analysis, two radii of curvature are computed by the equations shown in Figure 24. These radii of curvature,  $R_1$  and  $R_2$ , relate directly to  $R_0$  and  $R_p$ , but not uniquely or consistently (a branch choice must be made). In order to relate  $R_1$  and  $R_2$  to  $R_0$  and  $R_p$  through the scattered field ( $\alpha$  fixed), the expedient of making the subreflector cylindrical is used as indicated in the lower diagram of Figure 24. This immediately makes  $R_0$  extremely large (less than infinity because of the spherical wave incident upon the subreflector from the feed). The curvature  $R_p$  is not changed by this artifice. An appropriate match of  $R_1$  to  $R_0$  or  $R_p$  and of  $R_2$  to  $R_p$  or  $R_0$  is made accordingly.

SOUR INCOMESSAGE AND STATEMENT IN SECURIOR SECUR

The principal motive for examining the caustic lines is to further understand the phase characteristics of the dual-shaped reflectors. The caustic lines for the shaped subreflector scattered fields are very different from those encountered for the field scattered by the hyperboloid. This is apparently true for offset as well as circularly symmetric-shaped reflectors.

Figure 25 shows the caustic lines for the field scattered by a focused feed from an offset shaped subreflector.  $^{8}$ ,  $^{9}$  Note that the vertical scale for the inset diagram is many times greater than the scale for the full diagram; thus, the  $^{R}$  caustic is extremely large. The wavefront scattered from the subreflector is nearly planar in the plane of the diagram and near the extremities. It is also now clear that the line caustic discussed earlier and displayed in Figure 10 is an  $^{R}$  caustic or is due to curvature orthogonal to the plane of the diagram.

The  $R_p$  caustic lines for different  $\alpha$ , with  $\beta=\alpha/2$ , are displayed in Figure 26 for the 70-meter shaped reflectors. They have a character which is similar to the offset shaped case of Figure 25, but which is distinct from that of the Cassegrain system. In Figure 26, the  $R_p$  caustics are shown with respect to the subreflector. In Figure 27, the same  $R_p$  caustic lines are plotted with respect to the main shaped reflector. The subreflector is appropriately located only for the  $\alpha=0^\circ$  case.

The main reflector is to the left, fixed for all  $\alpha$  values. Note that the caustic lines, for various  $\alpha$ , all lie nearly parallel, especially for  $\alpha < 6^{\circ}$ . Thus, the phase of the geometrical optic field incident upon the main reflector will be relatively unchanged for  $\beta = \alpha/2$ . This phase compensation occurs in addition to very little over— or underillumination of the main reflector. Therefore, the shaped reflector performance with  $\beta = \alpha/2$  is very good.

In Figure 28, observe the R<sub>O</sub> (curvature orthogonal to the diagram) caustic characteristics for various O for the same 70-meter shaped reflector system. Note again that with respect to the main reflector (right-hand diagram), the caustic lines become much closer. The enlarged diagrams of Figure 29 show this more clearly.

### 5. CONCLUSION

In a circularly symmetric high-gain dual-reflector antenna system, a very substantially off-axis feed displacement can be accommodated while retaining a circularly symmetric subreflector. This can be done with little gain or gain/noise temperature (G/T) loss for both Cassegrain and dual-shaped reflectors. In both cases (the Cassegrain and the dual-shaped antennas), it is found to substantially improve the performance if the subreflector is rotated off-axis by an angle  $\beta$  that is one-half

the angle of rotation of the feed- $\alpha$ . This is imperative for the shaped reflectors because there is no unique phase center about which to rotate the subreflector and feed. However, to obtain an optimum G/T for the Cassegrain (as well as the shaped) reflectors, it is found that maintaining  $\beta = \alpha/2$  is important. Although the main reflector phase distortion is kept fairly small, the relationship  $\beta = \alpha/2$  ensures very little spillover of energy past the main reflector into a hot (270 K) ground.

In the hypothetical Cassegrain system discussed in this paper, no noise shield was used. Thus, the noise temperatures shown as a function of  $\alpha$  (feed rotation angle about the Cassegrain focal point), with  $\beta = \alpha/2$  or  $\beta = \alpha$ , are higher than can be obtained with a noise shield.

The temperatures shown in Figure 30 are more or less significantly different than the lower or higher that the total noise temperature of the antenna is found to be. A typical good system (a DSN 64-meter antenna) may have a noise temperature distribution as shown in Table 2.

If the dichroic and rear spillover noises are removed from the zenith elevation values of Table 2, about 14.6 K remains. The noise temperatures displayed in Figure 30 can be added to this value as a function of  $\alpha$  and G/T values can be obtained as a function of  $\alpha$  for the Cassegrain system used herein for  $\beta = \alpha$  and for  $\beta = \alpha/2$ . This result is displayed in Figure 31a. Note

Table 2. Noise for Very Good Cassegrain

Noise Source	Zenith K	30° Elevation
Amplifier	4.0	4.0
Waveguide at 300 K	4.7	4.7
Dichroic Surface	2.0	2.0
Galactic Noise	2.7	2.7
Atmosphere	2.6	5.2
Antenna		
Quadrapod	2.6	5.2
Rear Spillover	~0.4	~0.2
Total	~17.0 K	~22.0K

in Figure 31a that the G/T performance is superior for the  $\beta$  =  $\alpha/2$  case despite the phase error introduced by the  $\beta$  =  $\alpha/2$  value of the feed location. This is a direct result of the substantially flat and low noise temperature found for the  $\beta$  =  $\alpha/2$  case (see Figure 30). The difference in the G/T curves in Figure 31a would be even greater if a noise shield were built into the Cassegrain design. The difference is slightly less if a less optimistic noise temperature for the system is assumed:

oon valussa vanninga bebeeld benening shinees soomal opening onested onested

 $T_{\text{SYSTEM}} - T_{\text{ANTENNA}} = 20 \text{ K}.$ 

This result is shown in Figure 31b and would apply for antenna elevation angle below zenith.

#### **ACKNOWLEDGMENTS**

The work described in this paper was carried out by the Jet Propulsion Laboratory, California Institute of Technology, under contract with the National Aeronautics and Space Administration.

#### REFERENCES

- Galindo-Israel, V., and Mittra, R. (1977) Synthesis of
   offset dual shaped reflectors with arbitrary control of
   phase and amplitude. Paper presented at USNC/URSI E.M.
   Symposium, <u>IEEE Symp. Antennas and Propagat.</u>, Standford,
   California.
- Galindo-Israel, V., Mittra, R., and Cha, A. (1979) Aperture
  amplitude and phase control of offset dual reflectors,

  IEEE Trans. Antennas Propagat., AP-27: 154-164.
- 3. Galindo, V. (1963-1964) Design of dual reflector antennas and arbitrary phase and amplitude distribution, IEEE

  Proc. Int. Symp. Antennas and Propagat., Boulder,

  Colorado; also in IEEE Trans. Antennas Propagat.,

  AP-12:403-408.
- 4. Galindo-Israel, V., and Mittra, R. (1977) A new series representation for the radiation integral with

KANASAM BEESTAND INSCRING KING SALENDE

- application to reflector antennas, IEEE Trans. Antennas Propagat., 25:631-641.
- 5. Mittra, R., Rahmat-Samii, Y., Galindo-Israel, V., and
  Norman, R. (1979) An efficient technique for the
  computation of vector secondary patterns of offset
  paraboloid reflectors, IEEE Trans. Antennas Propagat.,
  27:294-304.
- 6. Rahmat-Samii, Y., and Galindo-Israel, V. (1979) Shaped reflector antenna analysis using the Jacobi-Bessel series, IEEE Trans. Antennas Propagat., 28:425-435.
- 7. Galindo-Israel, V., Imbriale, W., Rahmat-Samii, Y., and Veruttipong, T. (1984-1985) Interpolation methods for GTD analysis of shaped reflectors, <u>TDA Progress Report 42-80</u>, Jet Propulsion Laboratory, Pasadena, California.
- 8. Cha, A., Wide band diffraction improved dual-shaped reflectors, <u>TEEE Trans. Antennas Propagat.</u>, AP-30:173-176 (theoretical predictions herein subsequently totally verified experimentally).
- Cha, A., Galindo-Israel, V., and Mittra, R. (1979)
   Efficient design of offset dual-shaped reflectors for antenna and beam waveguide applications, <u>IEEE Int. Symp.</u>
   on Antennas and Propagat.

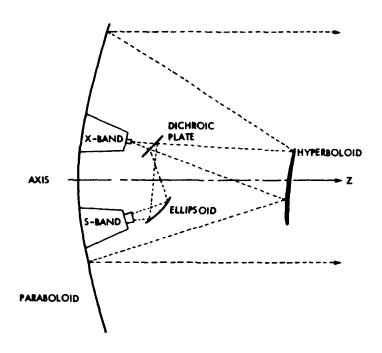
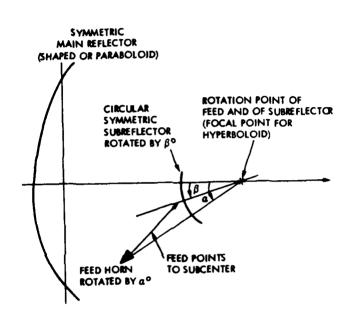


Figure 1. X-Band and S-Band Feeds Displaced
Off Axis

STORES RELEASED PROPERTY



Contract System Contract Contract

Figure 2. Geometry for Feed and Subreflector
Rotation

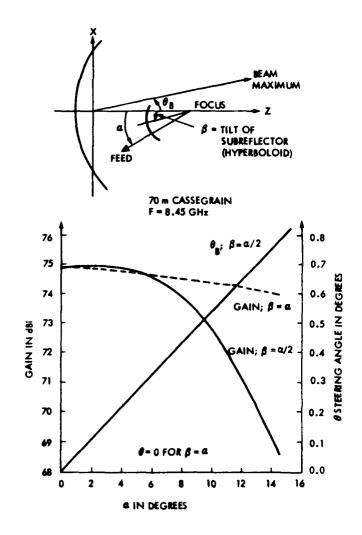


Figure 3. Gain and Steering Angle Versus

Feed Horn Rotated Angle for 70-m

Cassegrain Antenna

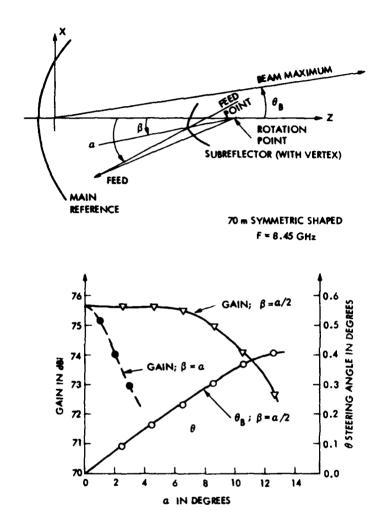


Figure 4. Gain and Steering Angle Versus

Feed Horn Rotated Angle (Q) for

70-m Symmetric-Shaped Antenna

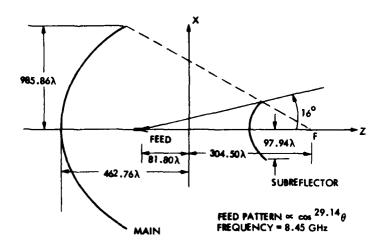


Figure 5. Geometry of Cassegrain Antenna

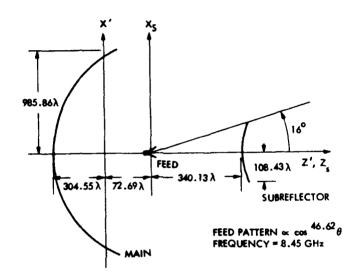
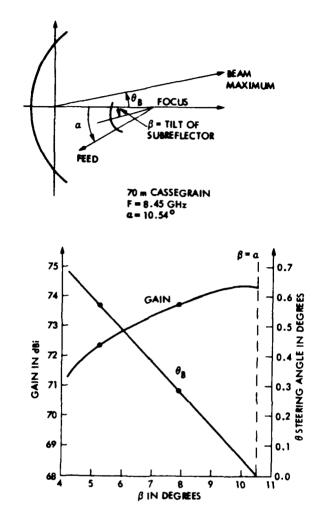
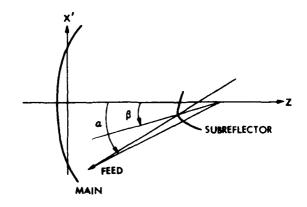
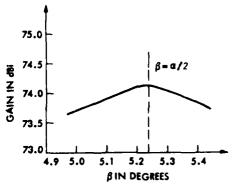


Figure 6. Geometry of Dual-Shaped Antenna





70 m SYMMETRIC SHAPED F = 8.45 GHz a = 10.482°



totat (district) residente considere consideramentalisation consider locations francisco francisco francisco fra

Figure 8. Gain Versus Tilt Angle of Subreflector ( $\beta$ ) for 70-m Symmetric-Shaped Antenna with  $\alpha$  = 10.482°

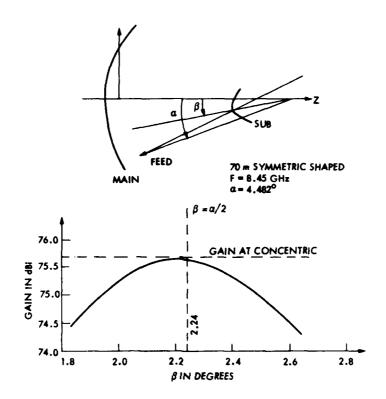
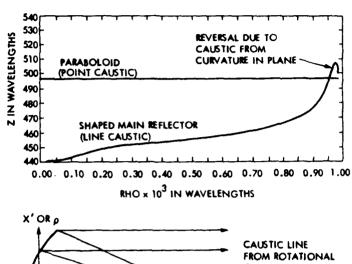


Figure 9. Gain Versus Tilt Angle of Subreflector ( $\beta$ ) for 70-m Symmetric-Shaped Antenna with  $\alpha = 4.482^{\circ}$ 

han december secretar mesessas secretar secretar assesses assesses because personal appropria anname lacific



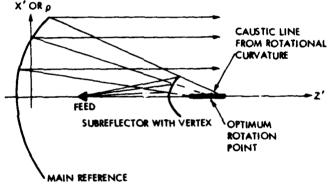
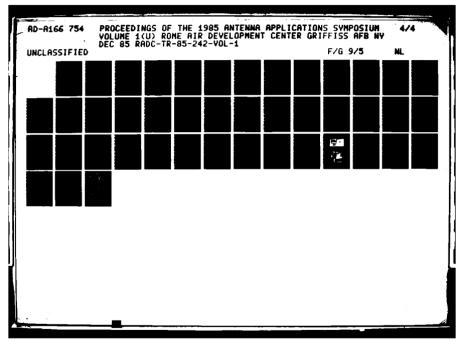
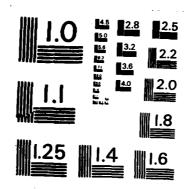


Figure 10. Z-Caustic Position Due to Rotational
Curvature (Curvature Out of Plane)

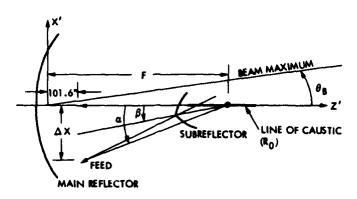
TOTAL STATE OF THE PROPERTY OF THE SERVICE OF THE S





MICROCOPY RESCUENCY TEST CHART NATIONAL BUREAU OF STANDARDS -1963 - A

the second of th



70 m SYMMETRIC SHAPED
β = a/2
θ = STEERING ANGLE
(BEAM MAXIMA)

NO.	ΔX, in.	F, in.	a, deg	GAIN, dBi	θg, deg	]
1	0.000	645.76	0.0	75.65	0.00	CONCENTRIC CASE
2	42.523	615.01	4.751	75.48	0.10	1
3	42.523	645.76	4.482	75.58	0.16	
4	42.523	710.06	4.007	75.20	0.26	1
5	42.523	641.6	4.517	75.59	0.15	BEST CASE

Figure 11. Determination of Optimum Point of Rotation

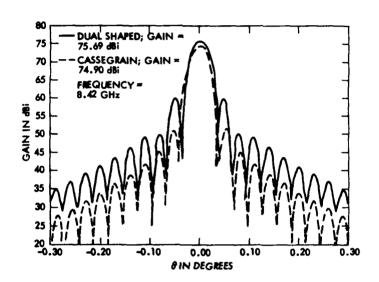


Figure 12. Far-Field Gain Patterns of the Dual-Shaped (with Vertex Plate) and Cassegrain Antennas with  $\alpha = \beta = 0 \text{ and } \alpha = \beta = 0^{\circ}$ 

B.

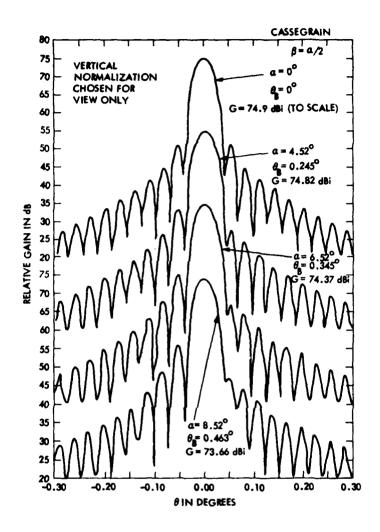


Figure 13a. Far-Field Gain Patterns of the Cassegrain Antenna with  $\beta=\alpha/2$ 

Ø,

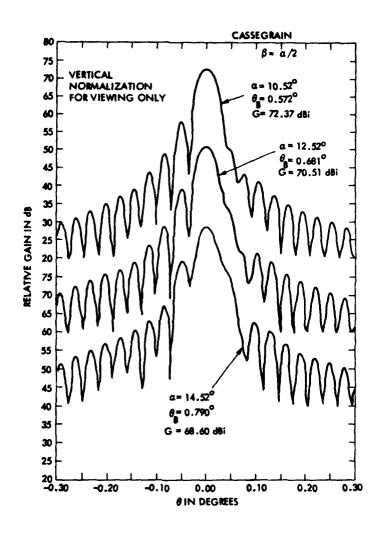


Figure 13b. Far-Field Gain Patterns of the Cassegrain Antenna with  $\beta = \alpha/2$ 

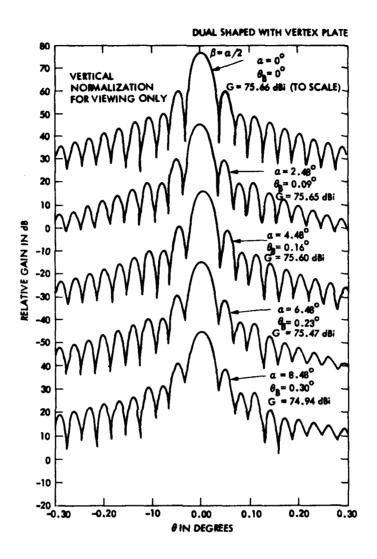


Figure 14a. Far-Field Gain Patterns of the Dual-Shaped (with Vertex Plate) Antenna with  $\beta=\alpha/2$ 

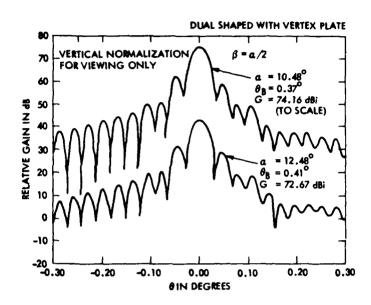


Figure 14b. Far-Field Gain Patterns of the Dual-Shaped (with Vertex Plate)  $\text{Antenna with } \beta = \alpha/2$ 

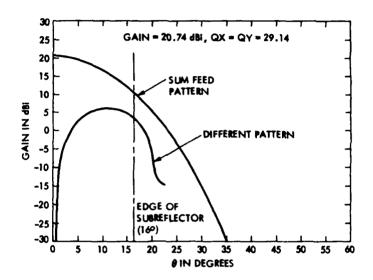


Figure 15. Feed Horn Radiation Patterns

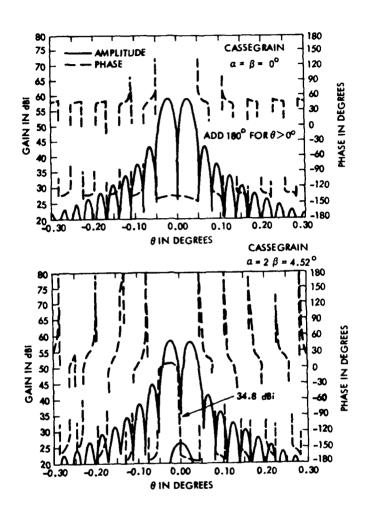


Figure 16. Difference Pattern of the Cassegrain Antenna

KARATA BARATA BARATA MARKA ARABATA BARATAN BARATAN

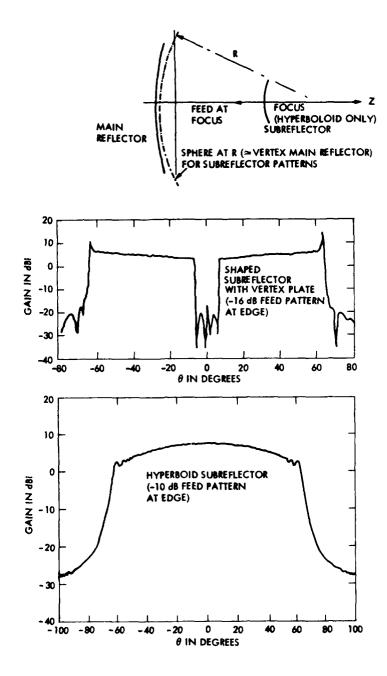


Figure 17. Subreflector Scattered Patterns

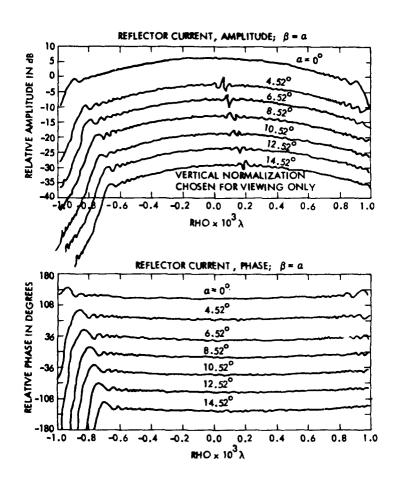


Figure 18. Aperture Current Distributions  $\qquad \qquad \text{of the Cassegrain Antenna for } \beta = \alpha$ 

ens secessos secessos estados estados

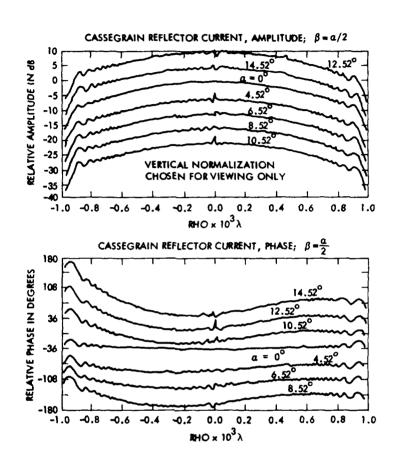
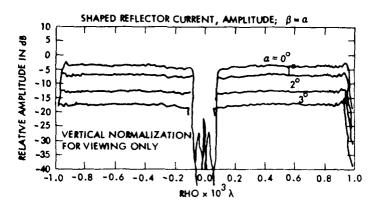


Figure 19. Aperture Current Distributions of the Cassegrain Antenna for  $\beta$  =  $\alpha/2$ 



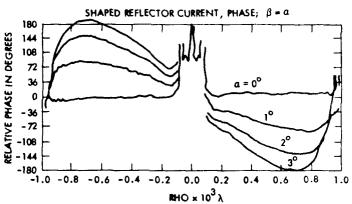


Figure 20. Aperture Current Distribution  $\qquad \qquad \text{of the Shaped Antenna for } \beta = \alpha$ 

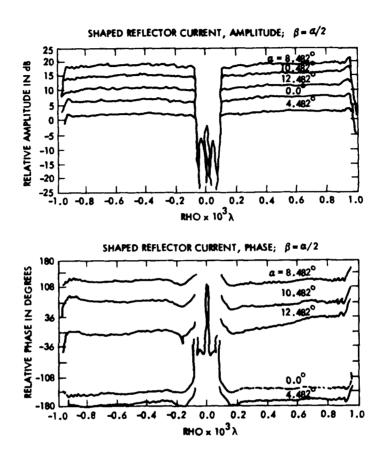


Figure 21. Aperture Current Distribution of the Shaped Antenna for  $\beta = \alpha/2$ 

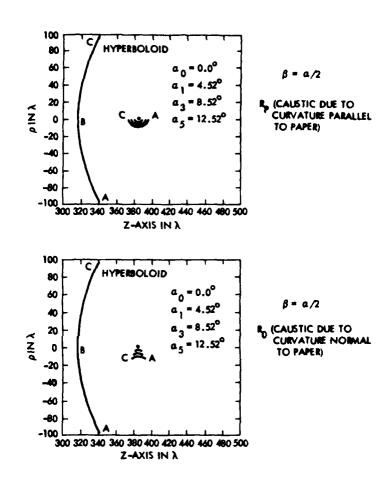


Figure 22. Caustic Surfaces of Field Scattered

from Subreflector of the Cassegrain

Antenna

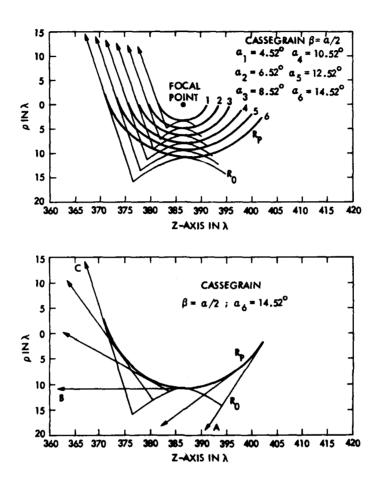


Figure 23. Caustic Surfaces of Field Scattered from Subreflector of the Cassegrain Antenna

skeed landers course broson species course course course course

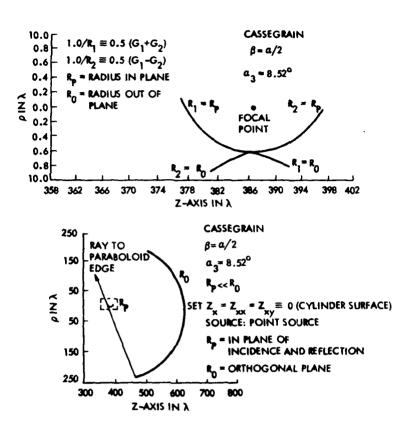


Figure 24. Caustic Surfaces of Field Scattered
from Subreflector of the Cassegrain
Antenna

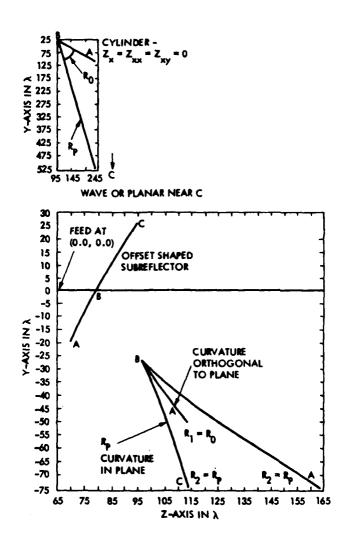
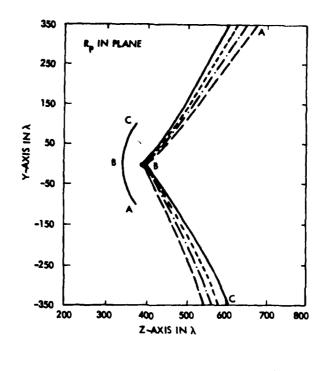
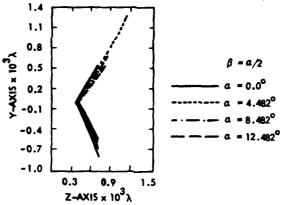


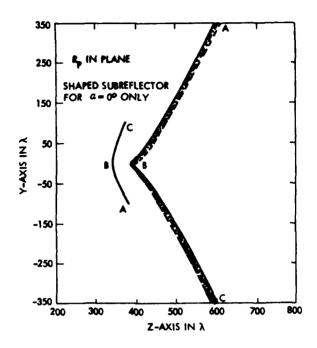
Figure 25. Caustic Surfaces of Field Scattered
from Subreflector of Dual Offset
Shaped Reflectors





en i socioción dispessiva l'occiónica massena moscola en consciona massena

Figure 26. R<sub>p</sub> Caustics (Parallel to Plane)
with Respect to Shaped Subreflector (70 m)



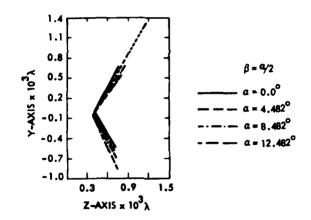


Figure 27. R<sub>P</sub> Caustics (Parallel to Plane)
with Respect to Shaped Main
Reflector (70 m)

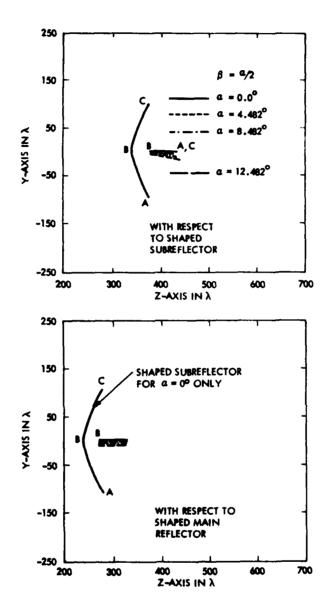
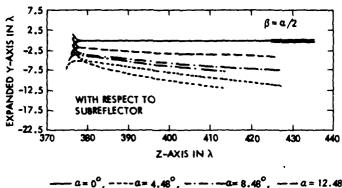
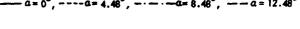


Figure 28. R<sub>O</sub> Caustics (Orthogonal to
Plane) with Respect to Shaped
Subreflector and Shaped Main
Reflector (70 m)

The second second second





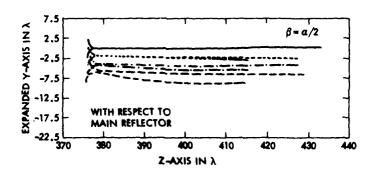
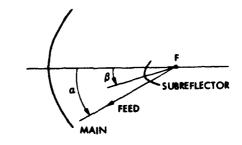


Figure 29. R<sub>O</sub> Caustics (Orthogonal to
Plane) with Respect to Shaped
Subreflector and Shaped Main
Reflector (70 m)



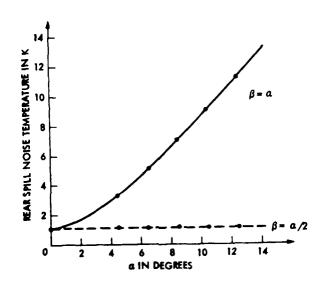


Figure 30. 70-m Cassegrain Near Spillover
Noise Temperature

Control Control Recents Control

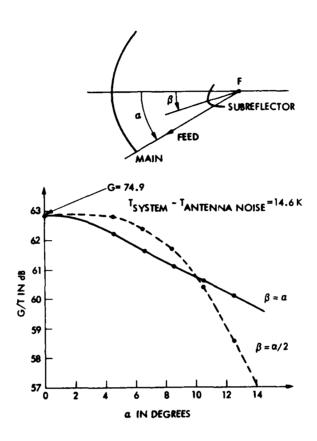


Figure 31a. 70-m Cassegrain G/T

SECOND DESCRIPTION OF THE PROPERTY OF THE PROP

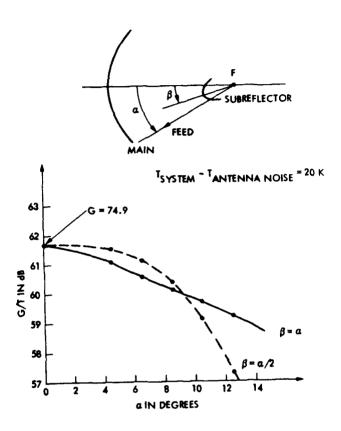


Figure 31b. 70-m Cassegrain G/T

## IMPROVING THE PERFORMANCE OF A SMALL REFLECTOR ANTENNA

M. Lewis, J. Toth, R. Kliger, and W. Miccioli Raytheon Company, Missile Systems Division Bedford, Massachusetts 01730

## ABSTRACT

Techniques for alleviating the performance problems encountered in small (ν20λ) reflector antenna configurations constrained to reside within a given volume are discussed. Small F/D systems generate a highly curved parabolic surface which tends to minimize aperture diameter, resulting in gain and beamwidth degradation. Enhancing the gain and beamwidth properties of a small gimballed reflector is described.

The performance enhancements are achieved primarily by increasing the projected area of the antenna aperture within the confines of a given sphere. The methods presented incorporate the principles of dielectric loading and surface stepping to achieve a reduction in the physical depth of the reflector. The increase in gain achievable is highly dependent on the particular antenna configuration (gimbal sphere diameter, F/D, etc). Commensurate with the increase in gain (and perhaps of equal value) is the decrease in half-power beamwidth afforded by the larger diameter aperture. Included with the theoretical discussion are experimental results obtained for a typical Ka-band reflector system.

## 1.0 INTRODUCTION

Seeker antenna aperture size is typically governed by missile body/radome diameter. In most cases, the largest diameter aperture possible is desired in order to maximize antenna gain and minimize antenna beamwidth. Gimballed seeker antenna diameters are even more restricted, since often not only the antenna aperture but also associated combining networks and receiver circuits must be mechanically steered. Packaging of all of these assemblies so that they reside within the allowable gimbal sphere (as indicated in Figure 1) greatly reduces the available antenna diameter and the achievable performance characteristics.

Reflector type antennas, popular at millimeter wave frequencies, offer a simple mechanical assembly with high power capability, but they require substantial aperture depth to achieve the parabolic surface. As seen in Figure 1, a significant increase in projected aperture area could be obtained simply by flattening the paraboloid. Such reduction in depth would result in a larger diameter antenna, with higher available area gain and a sharper antenna beam. This improvement in performance is particularly significant for small reflector antennas ( $\leq 20\,\lambda$  in diameter) with small F/D. This paper presents two potential methods for reducing the required paraboloidal thickness by either dielectric loading or surface zoning. Thus, in each case, the theoretically infinite operational frequency band is sacrificed for a narrow, defined frequency range of optimum operation and minimal iperture depth.

## 2.0 DESIGN SUMMARY

SECONDESCRIPTION OF THE PROPERTY OF THE PROPER

The specific design goal of this application was to maintain the desirable properties of the conventional parabolic reflector while "flattening" the reflector profile to obtain a larger diameter radiating aperture. Particular emphasis in the ensuing investigation was on improving antenna gain and beamwidth characteristics without a significant increase in mechanical complexity.

The first method employed reflector surface zoning, or "stepping", as illustrated in Figure 2. With this technique, the designer selects portions of reflector surfaces from among a family of parabolas that share the same focal point. Equation (1) is the equation that governs these parabolas. It is easily derived from the requirement that all geometrical ray paths have the same electrical phase (modulo  $2\pi$ ). Examination of the central ray path with this requirement in mind leads to the conclusion that the parabolas must be separated by  $\lambda/2$  along their axis of symmetry.

$$y^2 = 4 (f + \frac{\eta \lambda}{2}) (x + \frac{\eta \lambda}{2}) \text{ where } n = 0, 1, 2...\eta$$
 (1)

Although the zoning technique does increase the available aperture size, it will introduce concentric ring "shadow" regions at each reflector surface step, as suggested in Figure 3. These regions are not directly illuminated by the feeding element of the reflector and represent a loss of aperture area that must enter into the overall tradeoff of gain versus diameter. Therefore, a particular configuration will allow a certain maximum number of surface steps based on a given gimbal sphere radius, a prescribed gimbal center offset, and satisfaction of

the relative phase requirement. Not all steps need to be or should be provided because of step shadowing effects. Steps can be skipped and then compensated for by taking larger step sizes (i.e. skipping one or more parabolic surfaces) in an attempt to maximize the available unshadowed projected area.

Figure 2 shows a typical example in which five steps are possible; but as indicated in Table 1, the largest projected area occurs by taking only two steps, because the shadowing incurred by additional steps outweighs the area increase achieved from a greater overall diameter. For this case, the maximum increase in gain is .3 dB over the gain of the standard parabola commensurate with the given gimbal sphere radius and offset. Gain may not be the only parameter of interest. Since the antenna beamwidth is primarily dictated by the overall aperture diameter, a different set of steps will be necessary to minimize the beamwidth. A second inspection of Table 1 indicates that with only a slight decrease in unshadowed aperture area (i.e. gain), the aperture diameter can be maximized by using three surface steps. Indeed, this may be a better compromise configuration when all system parameters are considered.

The second method of performance enhancement may be visualized as loading the reflector with a low ( $\epsilon_{\rm r}{<}3.0$ ) dielectric constant material. This makes the reflector physically more shallow, as illustrated in Figure 4, allowing the dielectric reflector to be moved closer to the center of gimbal rotation and providing two beneficial effects. The first is the direct increase in diameter available from

TABLE 1 STEPPED PARABOLA GAIN CHARACTERISTICS

Configuration	<u>5</u>	Step 4	Number 3	* 2	1	Relative Projected Area	Relative Gain (dB)
1	0	0	0	0	0	1.00	0
2	0	0	0	0	1	.78	-1.1
3	0	0	0	ı	0	.94	3
4	0	0	0	ı	1	.84	7
5	0	0	1	0	0	1.00	0
6	0	0	1	0	1	.88	<b></b> 6
7	0	0	1	1	0	.96	2
8	0	0	1	1	1	.89	5
9	0	1	0	0	0	1.04	. 2
10	0	1	0	0	1	.88	6
11	0	1	0	1	0	.98	1
12	0	1	0	1	1	.91	4
13	0	1	1	0	0	1.03	.1
14	0	1	1	0	1	.91	4
15	0	1	1	1	0	.99	0
16	0	1	1	1	1	.93	3
17	1	0	0	0	0	1.04	.2
18	1	0	0	0	1	.85	7
19	1	0	0	1	0	.96	2
20	1	0	0	1	1	.89	5
21	1	0	1	0	0	1.03	.1
22	1	0	1	0	1	.91	4
23	1	0	1	1	0	.99	0
24	1	0	1	1	1	.93	3
25	1	1	0	0	0	1.06	.3
26	1	1	0	0	1	.90	5
27	1	1	0	1	0	.99	0
28	1	1	0	1	1	.93	3
29	1	1	1	0	0	1.05	, 2
30	1	1	1	0	1	.93	3
31	1	1	1	1	0	1.01	.1
32	1	1	1	1	1	.95	2

<sup>\*1 -</sup> indicates step taken
0 - indicates step not taken

moving the reflector aft and extending the edge of the parabola to intersect with the gimbal sphere. The second (although not as significant) is a further flattening of the parabola produced by the now increased focal length. This second effect also increases the diameter of the parabola, as indicated in Figure 5.

Equations (2) through (5), which define the pertinent parameters for this reflector's contour, are readily derived from Snell's Law and geometrical optics considerations. All quantities in these equations are defined in Figure 6.

$$\ell_{1} = \frac{r_{\text{ref}}^{\cos\theta} i^{-r} o}{\cos\theta_{i} (\sqrt{\epsilon + \sqrt{\epsilon - \sin^{2}\theta}}_{i})}$$
 (2)

$$\ell_2 = \frac{\ell_1 \sqrt{\varepsilon - \sin^2 \theta_i}}{\sqrt{\varepsilon}}$$
(3)

$$h = d+L \tag{4}$$

$$L = r_0 tan\theta_i$$

$$d = \frac{\tan^{\theta} i (r_{ref}^{\cos \theta} i^{-r}_{o})}{\sqrt{\varepsilon (\sqrt{\varepsilon} + \sqrt{\varepsilon - \sin^{2} \theta}_{i})}}$$
(5)

The dielectric filled contour will be more shallow than the free space parabola. Thus, the end result is a larger projected aperture area with no additional shadowing. Higher gain is not guaranteed because of the impedance mismatch at the dielectric to air interface. The impact of this effect must be weighed against the increase in diameter achievable and other antenna performance parameters. Methods of controlling the impedance mismatch must also be contemplated, such as

maintaining a low dielectric constant loading and incorporation of matching surface-coating layers.

The benefits of either diameter enhancement method described above are gated to some extent by the gimbal offset length "a" introduced in Figure 1. A large offset increases the parabola curvature, which in turn reduces the subtended diameter. As the value of "a" becomes small compared to the initial diameter of the reflector  $(\frac{\mathbf{a}}{D_3} \leq 0.1)$ , the benefits of these two techniques diminish accordingly.

To determine the magnitude of "shadow" region and surface impedance mismatch effects, flattened reflectors of each type can be compared to a standard reflector of similar diameter and focal length. In this manner the reduction in gain measured with the two modified reflectors would indicate the efficiency factor introduced by the two subject methods. The results obtained can then be used to determine the potential benefits of each enhancement technique.

## 3.0 EXPERIMENTAL RESULTS

The three reflectors that were fabricated and tested are illustrated in the photograph of Figure 7. The stepped parabola and dielectric filled parabola were fabricated from aluminum by a numerically controlled machine, while the simple parabola was made from a machined syntactic foam plated with copper. A square  $.605\lambda$  x  $.605\lambda$  open-ended waveguide radiator was positioned at the focal point of each of the reflectors as a feed. The square waveguide was connected to an orthogonal mode transducer allowing for dual polarized operation. The square waveguide feed was operated in the dominant  $TE_{10}$  mode.

The test fixture used in the anechoic chamber during measurement of the reflector antennas is illustrated in Figure 8; it shows the simple parabola mounted with the square open-ended waveguide feed. The test fixture has 4 degrees of freedom, which allows the alignment of the feed and reflector to be controlled with a moderate degree of accuracy. The three dimensional alignment is accomplished with 3 independent precision micrometer drives and one axis of rotation for the feed.

Typical measured H-plane radiation patterns (out to  $\pm 40^\circ$  from the axis of the mainbeam) are illustrated in Figures 9, 10, and 11 for the simple, stepped, and dielectric filled parabolas, respectively. A typical E-plane radiation pattern is shown in Figure 12 for the stepped parabola over  $-90^\circ \le \theta \le 90^\circ$ . The 3dB beamwidths of all three configurations (all 19.3 wavelengths in diameter) were approximately 4 degrees and indicate that beamwidth is determined primarily by the outside diameter of the reflector. The measured first sidelobe levels were below -20dB, which is in good agreement with predicted values for these considerations.

The gains, efficiencies, and beamwidths are presented in Table 2. The stepped parabola and dielectric filled parabola are 0.6dB and 1.0dB, respectively, lower in efficiency than the simple parabola. The overall efficiencies of the antennas measured were low because of feed mismatches and losses in the square aluminum waveguide. The same feed was used for all three configurations, so the efficiency factors listed above should be realistic.

TABLE 2. MEASURED ANTENNA CHARACTERISTICS

	Gain	Antenna Efficiency	3dB Beamwidth
Simple Parabola	32.3 dB	-3.35 dB	3.9°
Stepped Parabola	31.7 dB	-3.95 dB	3.8°
Dielectric Filled Parabola	31.3 dB	-4.35 dB	4.0°

## 4.0 CONCLUSIONS

Techniques have been presented that offer the potential of reducing the beamwidth and increasing the gain of a standard small parabolic antenna. Measured data at Ka-band have been presented which define the gain efficiency factors encountered in surface zoned and dielectrically loaded parabolic reflectors. The relative gain measurements for these parabolas indicate a higher than expected gain loss for both modified reflectors. In the case of the stepped parabola, approximately .4dB can be accounted for in loss from shadow regions. For the loaded reflector, excessive mismatch losses are suspect which may necessitate additional surface dielectric matching layers.

The measured data also showed only minor changes in other antenna pattern parameters resulting from the two methods. In particular, the initial assumption that zoning and loading of a parabola have little effect on beamwidth was clearly verified. Further effort will be required to optimize performance for each technique if the maximum benefit is to be obtained.

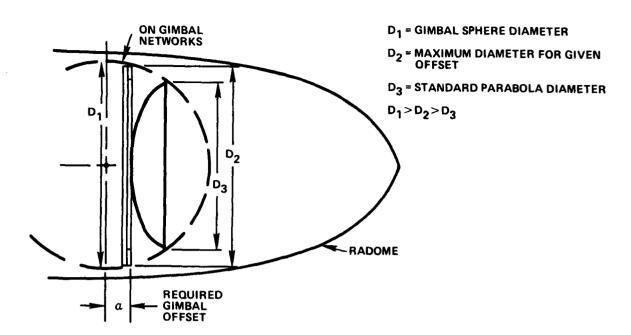


Figure 1. Typical Seeker Antenna Volume Constraints

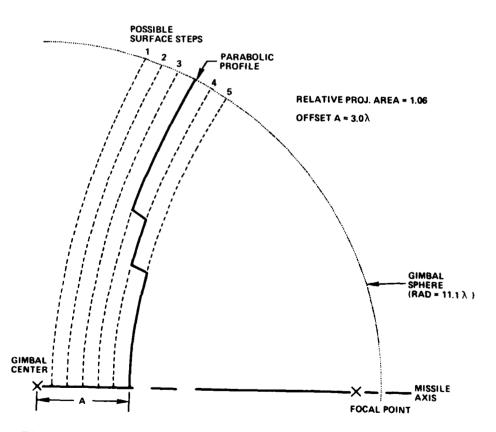


Figure 2. Stepped Parabolic Antenna Surface Profile

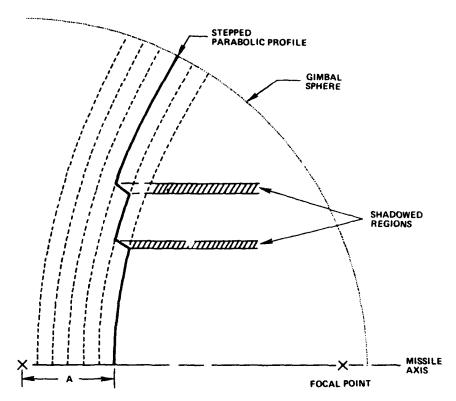


Figure 3. Stepped Reflector Shadow Regions

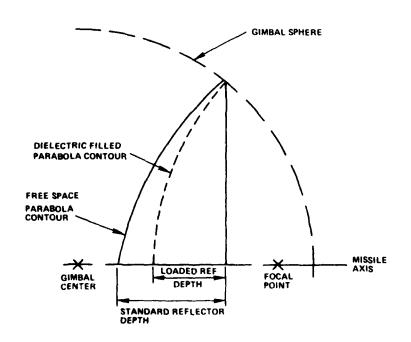


Figure 4. Dielectric Loading Depth Reduction

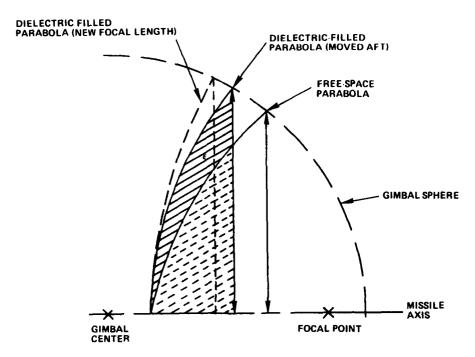


Figure 5. Aperture Size Enhancement due to Dielectric Loading

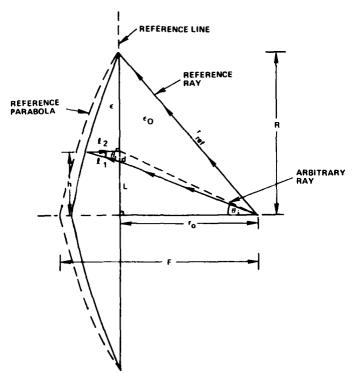


Figure 6. Dielectric Filled Parabola Geometry

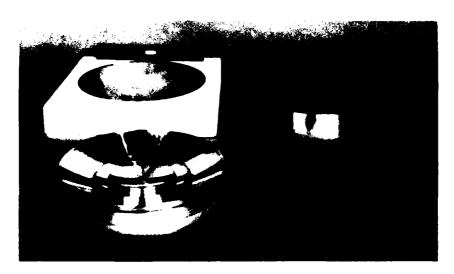
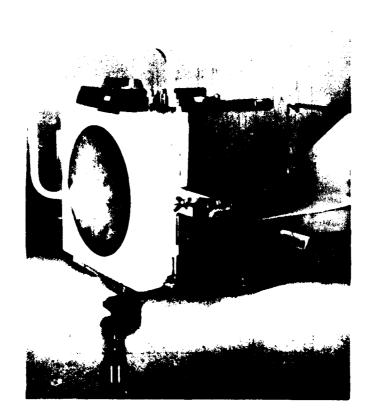


Figure 7. Parabolic Test Reflectors



and provided accounts broughts assesses assesses assesses assessed a contract

Figure 8. Reflector/Feed Alignment Fixture

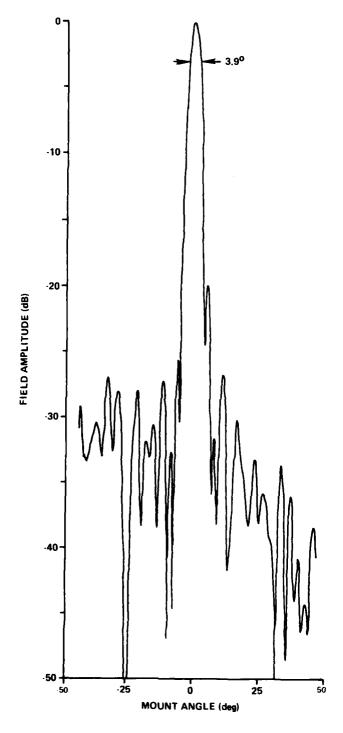
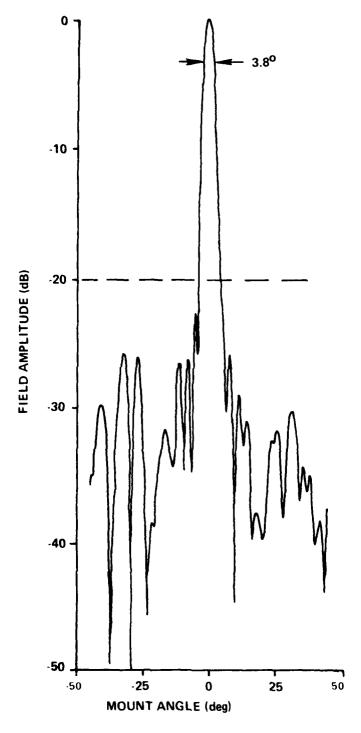


Figure 9. Simple Parabola H-Plane Pattern



ser linesseed bearded beautifus issuites exercise extractor progress resource

Figure 10. Stepped Parabola--H-Plane Pattern

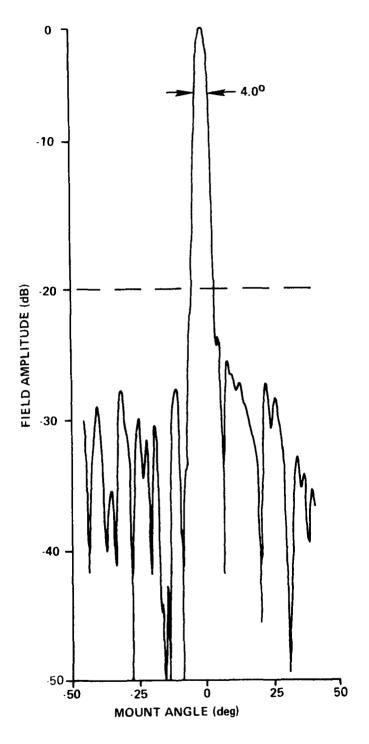


Figure 11. Dielectric Loaded Parabola--H-Plane Pattern

4.

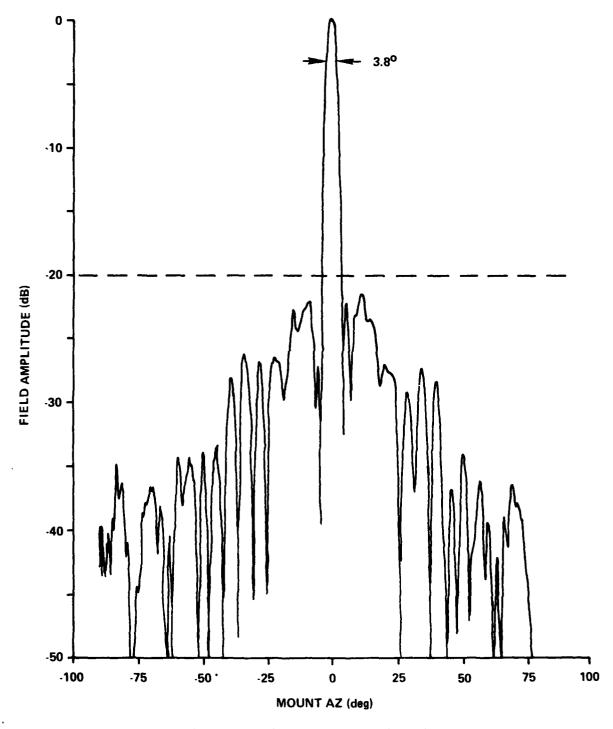


Figure 12. Stepped Parabola--E-Plane Pattern

second leaders leaders bases leave

## MISSION of Rome Air Development Center

RADC plans and executes research, development, test and selected acquisition programs in support of Command, Control Communications and Intelligence  $(C^3I)$  activities. Technical and engineering support within areas of technical competence is provided to ESD Program Offices (POs) and other ESD elements. The principal technical mission areas are communications, electromagnetic guidance and control, surveillance of ground and aerospace objects, intelligence data collection and handling, information system technology, solid state sciences, electromagnetics and electronic reliability, maintainability and compatibility.

Printed by United States Air Force Hanscom AFB, Mass. 01731

SANDARDE OF LANDERS

\*\*\*\*\*\*\*\*

DT/C 5-86